UCLouvain

AGRO LOUVAIN BIOINGÉNIEURS

Faculty of bioscience engineering

Validation of drone-borne Ground Penetrating Radar method for soil moisture mapping

Author: Thibaut Parizel
Supervisor: Sébastien Lambot (SST/ELI/ELIE)
Readers: François Jonard (SST/ELI/ELIE)
Quentin Limbourg (CRA)

Academic year 2020 - 2021

Thesis presented in partial fulfilment of the requirements for the degree of Master [120] in environmental bioengineering

Abstract

Nowadays, agriculture is the leading consumer of freshwater resources, accounting for 70% of the global extracted volume. With the global population set to increase by 65% by 2050, pressure on freshwater resources will increase more importantly without a more sustainable agricultural system.

In that regard, Ground Penetrating Radar (GPR) methods are very promising with respect to the precision irrigation, which needs information collection of soil water content at high spatial resolution. GPR methods can bridge the gap between the small scale of the TDR and the larger scales of the remote sensing instruments and constitute therefore an useful tool for the road to sustainability.

This thesis aims the validation of the soil moisture mapping through drone-borne GPR using the radar model of Lambot et al. (2004). In this paper, several numerical experiments were carried out to assess the viability of the assumptions of the model. Then, some acquisition campaigns were conducted and the results were assessed both quantitatively and qualitatively. Finally, a validation campaign was carried out using several tools in order to allow the comparison between these, as well as with ground-truth moisture value.

Acknowledgements

The development and the completion of this master thesis have only been possible with the contribution of valuable people that helped and supported me during this long process, this section is therefore dedicated to acknowledge them.

First, I would like to sincerely thank my supervisor, Prof. Sébastien Lambot, for his continuous support, advice, assistance and availability despite his overflowing agenda. He made me feel involved during the all-year long data acquisitions and guided me in my work.

I would also like to thank Kaijun Wu, a great and young PhD student of the GERU lab, for all the precious help she gave me during our many exchanges.

Then, a great thank is addressed to Loic Ory and Laura-Maria Palt, for the mutual help and support face to the encountered issues.

I also thank the readers of this thesis, François Jonard and Quentin Limbourg for taking the time to read this thesis.

Thank also to Rémi Desmet from UCLouvain, which gives us a free access to the studied site in the Ferme de Lauzelle.

Finally, I would like to thank my family and friends for their support since the beginning of my studies, which were a wonderful blossoming period of fulfilment and development that will always be a part of me.

Contents

List of Figures

Nomenclature

CMP Common Midpoint

CNSW Carte Numérique des Sols de Wallonies

DEM Digital Elevation Model

dGPS Differential Global Positioning System

FAO Food and Agriculture Organisation

GPR Ground Penetrating Radar

LUT Look Up Table

PEC Perfect Electric Conductor

RMSE Round Mean Square Error

SAR Synthetic Aperture Radar

SFWB Stepped-Frequency Continuous-Wave

SOL Short-Open-Load

SWC Soil Water Content

TDR Time Domain Reflectometry

UAV Unmanned Aerial Vehicle

UWB Ultra Bide Band

VNA Vector Network Analyzer

VSWC Volumectric Soil Water Content

WARR Wide Angle Reflection and Refraction

WCM Water Content Measurements

Chapter 1

Introduction

1.1 Context

Water is the most widely distributed resource on Earth and is an essential resource for all the living organisms living on it. In addition to being the universal support of life, freshwater is needed for our society: agriculture, industry, sanitation and energy. At the same time, natural hazards involving water, such as floods, droughts and landslides are major natural threats to society in many countries. The vadose zone, which may be defined as the transition zone between the atmosphere and groundwater reservoirs, is important for water resource management, because it regulates the water availability for vegetation, including crops, while at the same time it provides a protective buffer zone between land surface and groundwater against solutes and pollutants [Huisman et al., 2003].

Freshwater is often referred to as "blue gold" because it is so precious and becomes increasingly scarce in some regions of our world. Indeed, despite the fact that water is omnipresent on earth, among all this resource, only 2.5% is actually freshwater. Most of this freshwater (70%) is in its solid form in the cryosphere as ice and snow and 30% is groundwater, but these two biggest freshwater stocks are not easily accessible. Surface water, such as rivers and lakes, only account for 0.3% of freshwater, but is readily accessible [Jonard, 2020]. Furthermore, not all countries are equal to face their needs in freshwater because climate, lack of infrastructure, poor water management and population growth put high pressure on water resources quantity and quality.

During the past decades, there has been a massive anthropogenic change in the hydrological cycle, affecting both the quality and the quantity of water. Now, the spatial and temporal water distribution are determined not only by the natural water cycle but also by the human economic activities. Water resources are so much impacted by contamination and depletion that in some parts of the world, they are not able to reach the demand anymore. Water has become the first factor impeding population growth and economic development [Shiklomanov, 1998; Chenoweth, 2008].

Moreover, with a global population set to increase by 65% by 2050, the additional food production required to feed the additional 3,7 billion persons will put further important pressure on freshwater resources, if considering the actual water use in agriculture. Indeed, because all vegetation requires and transpires massive amounts of water when growing, world agriculture is the largest water consumer, accounting for 70% of the total human use of freshwater [FAO, 2017; Wallace, 2000]. Moreover, to ensure basic human health, a person needs between 50 and 100 litres of water per day. In addition, 3 to 4m^3 per capita of rain-originated are consumed to produce human food. This water is denoted as "green-water". Whenever agricultural demand is not fulfilled by green-water, irrigation can fill the gap using water from rivers or groundwater. This leads to a global daily consumption (household, industrial, irrigation) of 1 to 2m^3 per person despite the increasing scarcity of freshwater [Pimentel et al., 2004; Oki et al., 2017].

Beside being essential for the agricultural production, soil moisture is a potential limiting factor for land carbon uptake. When water stress is present in the ecosystem, a higher rate of vegetation mortality and a reduction of gross primary production appear. Indeed, about 25% of the anthropogenic CO_2 is absorbed by the terrestrial biosphere and, therefore, when this biosphere is limited in water, the land carbon sink is reduced [Green et al., 2019].

With its particularly high water consumption, agricultural water management must be enhanced in a more sustainable way. Indeed, to avoid productivity losses due to water stress caused by under-irrigation, farmers spray more water than actually needed. This over-irrigation leads to water and energy waste but also compromises productivity. Nevertheless, precision irrigation can use freshwater much more efficiently and effectively, avoiding both under-irrigation and over-irrigation. This precision irrigation allows to reduce cost, improve productivity and contribute to the environmental sustainability by optimising water supply [Kamienski et al., 2019]. To allow the implementation of such precision irrigation, information collection of soil water content in appropriate spatial and temporal resolution is needed at the field scale [Griffin et al., 2018]. To do such information collection, ground-penetrating radar (GPR) tools seem to be very promising.

1.2 Ground Penetrating Radar potential

High frequency electromagnetic techniques are the most promising sensors to fulfill the need of moisture characterization at different scales. Remote sensing is the most adapted technique for water measurements at larger scales (passive instruments with resolution of tens of square kilometers and active radar instruments with resolution from 10 to several 1000 square meters) [Mohanty et al., 2017; Huisman et al., 2003].

At significantly smaller scales, the in situ method of Time Domain Reflectometry (TDR) provides a high spatial and temporal resolution of the soil water content. Nevertheless, in

addition to being time-consuming and destructive, the small measurement volume in the order of the cubic decimeter makes the method sensitive to water content variations and does not provide the expected information at the field scale [Schwartz et al., 2008; Huisman et al., 2003].

There is hence a significant scale gap between TDR and remote sensing, for this reason, the GPR is considered as the most adapted tool at the field scale because of the high sensitivity of GPR wave velocity to changes in soil water content (SWC) [Klotzsche et al., 2018; Minet et al., 2012].

Indeed, with its intermediate scale in the order of the meter, GPR allows to bridge the gap between TDR and the remote sensing instruments [Minet et al., 2012]. GPR instruments, when set up on a Unmanned Aerial Vehicles (UAV), would reduce the time measurements and would not impact soil and vegetation during the growing season [Wu et al., 2019].

1.3 Objectives of the thesis

Thus, GPR being very promising for a more sustainable water management, specially in agriculture, the main objective of this thesis is the validation of drone-borne mapping for soil water content at the field scale. The GPR application of the used model at the field scale is no longer in question, since it was already validated in [Minet et al., 2012]. Nevertheless, this validation was made by using a horn-antenna mounted on a all-terrain vehicle, while this thesis will focus on a drone-borne data acquisition, thanks to a lightweight dipole antenna. This drone-borne acquisition, despite the limitation of the UAV batteries, presents many non negligible advantages compared to the all-terrain vehicle acquisition, as the automation of the flight, the ease of transport and the non-impacting measurements with regard to the vegetation. Nevertheless, the payload capacity of the drone becomes a constraint and requires equipment changes, as the antenna, lighter than the horn antenna but less directive. In order to construct the validation, several specific objectives are defined.

First, a sensitivity analysis will be conducted using numerical experiments. These experiments will be focused on the used frequency range during acquisition campaigns. The aims of this sensitivity analysis are the assessment and the quantification of the error brought by the main hypotheses of the model, such as the consideration of a non-conductive soil. Indeed, at high frequencies, the electrical conductivity is generally neglected since its effect on wave reflections is negligible, which does not hold for relatively low frequency ranges. The assessment of the impacts of the conductivity on the retrieved permittivity will therefore allow its consideration during the discussions.

Then, several acquisition campaigns will be carried out to qualitatively assess the obtained data. Theses campaigns will be repeated over time to visualize the measurement improvements, as well as to study the spatial distribution and dynamics of the soil water content of the study

field.

Finally, at the end of the different calibration and acquisition campaigns, a whole day will be dedicated to a final acquisition campaign, during which several measurement methods, dielectrics or not, will be used in order to make comparisons. Indeed, methods considered as references, such as Time Domain Reflectrometry (TDR) and gravimetry will provide soil water content values considered as ground-truth water content. These real values will therefore allow error calculation for dielectric measurements. Then, the measurement repeatability will be assessed by comparison between several field measurements taken in a short time window.

Chapter 2

State of the art

The non-invasive GPR method relies on the existing relation between soil constituents such as the soil water content, and its electric properties, namely, the dielectric permittivity, the electric conductivity and the magnetic permeability [Thomas, 2010]. In order to allow a better understanding of the different methods used in the GPR application, a presentation of the state of the art in the domain of soil electric proprieties is needed. Further, a review of the literature about the water characterization methods and an exploration of the GPR theory will be presented.

2.1 Electromagnetic Principles

Three electromagnetic parameters describe the response of the soil, considered as a dielectric medium, to an applied electromagnetic field: the magnetic permeability μ, the electrical conductivity σ and the dielectric permittivity ε [Jol, 2008].

2.1.1 Magnetic permeability

The **Magnetic permeability $\boldsymbol{\mu}$** characterizes the induced magnetism due to the applied magnetic field [Jol, 2008]. In the GPR application, the magnetic permeability is usually supposed equal to the free-space permeability (noted μ_0). Indeed, the magnetic effect of material has very little effect on the GPR propagation since most minerals, as well as water, have a relative magnetic permeability very close to 1. Nevertheless, a magnetic material such as ferromagnetic minerals can impact wave velocity and wave signal attenuation [Cassidy, 2009].

2.1.2 Electrical conductivity

The **Electrical conductivity $\boldsymbol{\sigma}$** (Sm^{-1}) describes currents from free charges movements in response to an applied electromagnetic field and impacts wave attenuation [Awak et al., 2017; Lambot et al., 2004]. Given the fact that electrical conductivity impacts waves propagation, it determines the characterization depth : a higher conductivity will induce a lower depth of

characterization.

At relatively low GPR frequencies, the conduction current is in phase with the electric field. Considering this fact, the conductivity can be represented by a real value. At higher frequencies, an inertial effect induces an out-of-phase conduction current regarding the electric field variations. In this case, the conductivity must be described by a complex value where the imaginary component represents the out-of-phase current [Cassidy, 2009].

Nevertheless, for moisture characterization considering only the soil surface reflection coefficient with GPR, this parameter can be neglected. [Lambot et al., 2006b] showed through numerical experiments and hence, free of radar measurement errors, that in the model configuration illustrated in Figure 2.1, where electrical conductivity is neglected ($\sigma_1 = 0$), the standard error on the estimated volumetric water content was about 8,53e-7 (with a full-wave inversion method and frequency range from 100 MHz to 900 MHz) and, therefore, neglecting of σ is justified.

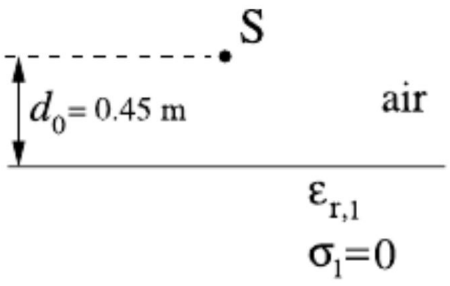

Figure 2.1 – Model configuration considering a source-receiver above a lossless dielectric halfspace. From [Lambot et al., 2006b].

2.1.3 Dielectric permittivity

The **dielectric permittivity** ε (Fm^{-1}) describes the resulting currents of the bound charge displacement and characterizes the material polarizability under the influence of an electric field. Generally, it is quote in terms of relative permittivity (dimensionless) expressed as:

$$\varepsilon_r = \frac{\varepsilon}{\varepsilon_0} \tag{2.1}$$

where ε_0 is the permittivity of free space ($\varepsilon_0 = 8.8542 \times 10^{-12}$ F/m) and ε is the permittivity of the material.

When frequency increases, the bound charges can not follow the fast alternative electric field which creates a relaxation phenomenon resulting in a out of phase polarization [Lambot

et al., 2004]. In that respect, the dielectric permittivity is defined as a complex quantity:

$$\varepsilon_r = \varepsilon'(f) - j\left(\varepsilon''(f) + \frac{\sigma_{\mathrm{dc}}}{2\pi f \varepsilon_0}\right) \tag{2.2}$$

In this equation, f is the frequency (Hz) of the electromagnetic field, σ_{dc} is the DC (direct current) conductivity, the real part $\varepsilon'(f)$ is associated with the energy storage under an alternating electromagnetic field while $\varepsilon''(f)$ is the imaginary part and is associated with the energy dissipation [Robinson et al., 2003].

This dielectric permittivity also determines the velocity $v(\mathrm{ms}^{-1})$ of electromagnetic wave propagation [Huisman et al., 2003]:

$$v(f) = \frac{\mathrm{c}}{\sqrt{\varepsilon'(\mathrm{f})\mu_r \frac{1+1\sqrt{1+\tan^2\delta}}{2}}} \tag{2.3}$$

where c is the velocity of an electromagnetic wave in free space, μ_r is the relative magnetic permeability and $\tan\delta$ is the loss tangent defined as the ratio of the imaginary and the real part of the permittivity and hence expressed as:

$$\tan\ \delta = \frac{\varepsilon''(f) + \frac{\sigma_{\mathrm{dc}}}{2\pi f \varepsilon_0}}{\varepsilon'(f)} \tag{2.4}$$

It is known that the dielectric properties of the soil vary with the frequency. These variations arise from the relaxation phenomenon reflecting the presence of water bound to mineral surfaces (since the H_2O is a dipole, there is a double-layer polarization) but from the ion-solid interactions too [Lambot et al., 2004]. Therefore, it is quite important to characterize the losses from these effects. The empirical Debye relaxation equation accounts for these effects and is described as :

$$\varepsilon_e(f) = \varepsilon_{e,\infty} + \frac{\varepsilon_{e,0} - \varepsilon_{e,\infty}}{1 + j\frac{f}{f_r}} \tag{2.5}$$

In this equation, f is the frequency, f_r is the relaxation frequency of the soil, which is defined as the frequency at which the permittivity equals $\frac{\varepsilon_{e,0}+\varepsilon_{e,\infty}}{2}$, $\varepsilon_{e,0}$ is the static permittivity and $\varepsilon_{e,\infty}$ is the permittivity at frequencies so high that the molecular orientation does not have time to contribute to the polarization. This empirical model accounts for a single relaxation mechanism, while more than one relaxation mechanisms can be observed for soils [Lambot et al., 2004; Huisman et al., 2003].

Huisman et al. [2003] illustrated the separation of the Debye model into the real and imaginary parts as shown in Figure 2.2. This figure accounts for an idealized model with $\varepsilon_{e,0} = 20$, $\varepsilon_{e,\infty} = 15$, $\sigma_{dc} = 0$ and $f_r = 300$ MHz. This shows that for very low and very high frequencies, the permittivity has constant values and zero losses while at intermediate frequencies, an energy dissipation occurs with a peak loss value at $f = f_r$. Water Debye's parameters are $\varepsilon_{e,0} = 80.1$, $\varepsilon_{e,\infty} = 4.2$ and $f_r = 17.1$ GHz at 25C°. Also, in sandy soil, water is mainly in free liquid state, while in clay soils water is absorbed by capillarity and limited in

motion. For absorbed water, dielectric relaxation takes place at lower frequencies than for free water [Huisman et al., 2003].

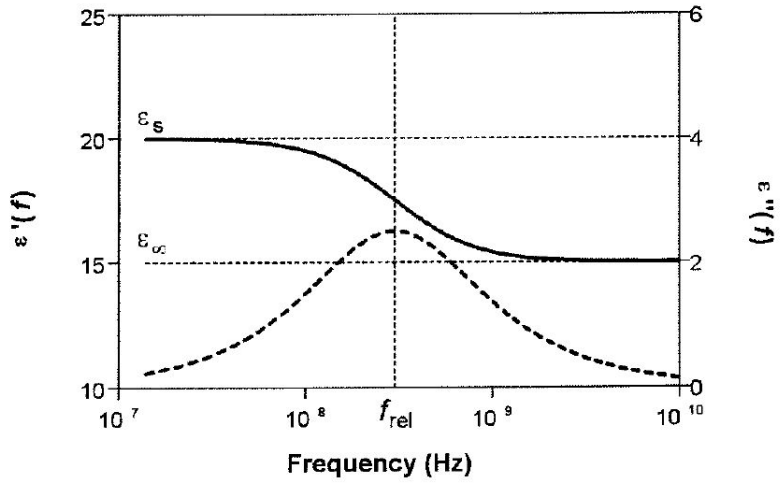

Figure 2.2 – Example of Debye's model for the imaginary part (dashed line) and real part (solid line) of the permittivity for an idealized medium. From [Huisman et al., 2003]

In GPR applications, the frequency bandwidth is generally from 10 MHz to 2 GHz. Considering those frequencies, ε"(f) is generally negligible compared to ε'(f). Moreover, most of the soils does not show relaxation phenomenon at GPR frequencies [Huisman et al., 2003]. For these reasons, Equation (2.3) is reduced to:

$$v = \frac{c}{\sqrt{\varepsilon'}} \tag{2.6}$$

Dielectric behavior of water

Since this thesis is focused in the determination of soil water content, it is useful to precise its dielectric properties.

Water is a complex dielectric polar molecule. Its relative dielectric permittivity depends of its temperature, its ionic concentration, its physic state and of the used frequency range.

Figure 2.3 gives the variations of the water relative permittivity for the real and imaginary components in function of frequency. Regarding this figure and considering the frequency range of the GPR application (1MHz - 2GHz), the relative permittivity is given by its real part and has a constant value of approximately 80. Therefore, in this frequency range, the water relative dielectric permittivity can be considered as poorly frequency dependant [Zakri, 1997].

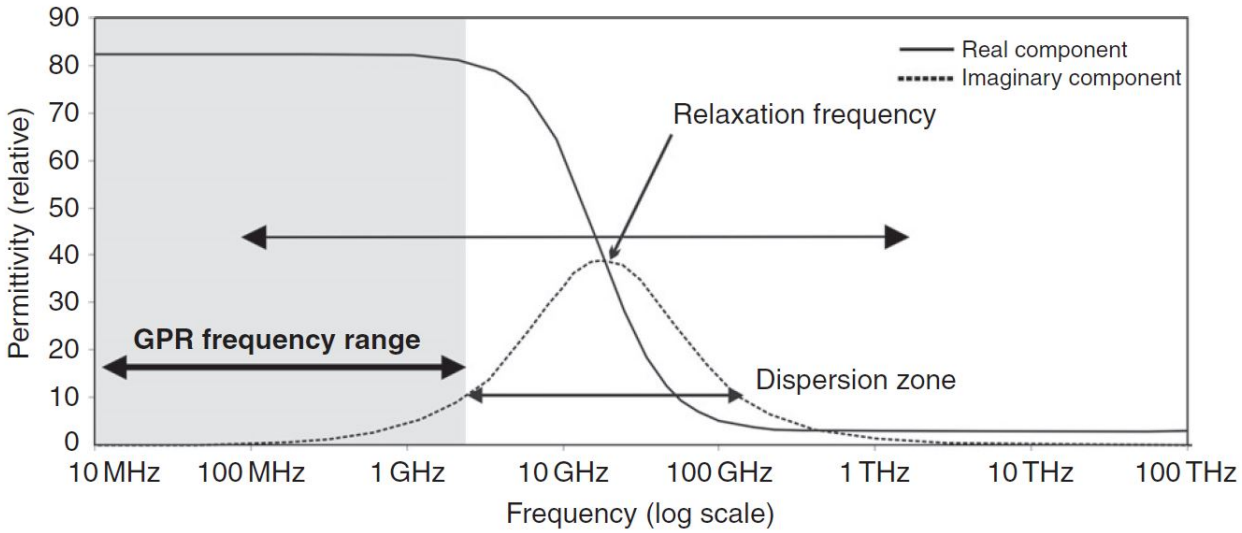

Figure 2.3 – Dielectric behavior of free water at 25°C. From [Cassidy, 2009]

2.2 Soil water content determination

Most of the methods of soil water content determination are indirect, which means that water content is determined through the measurement of an other parameter, linked to the soil water content (SWC). Some other methods are direct, such as the reference gravimetric method. In this section, some water determination methods will be summarized.

2.2.1 The reference gravimetric method

This technique, considered as reference method for ground-truth sampling in this thesis, involves the extraction of small diameter cores. Once sampled, these cores are weighed and dried for 48 hours at 105°C. The dry samples are re-weighed to determine the water mass loss from the original samples. The water mass can therefore be calculated by (gg^{-1}):

$$\theta_w = \frac{M_t - M_s}{M_s} \tag{2.7}$$

Usually, this water content is expressed in volumetric units (cm^3cm^{-3}):

$$\theta_v = \frac{M_t - M_s}{\rho_w V_t} \tag{2.8}$$

where M_t is the total mass of the original samples, M_s is the mass of the dry sample, ρ_w is the water density and V_t is the volume of the original sample [Bielders and Javaux, 2019].

Although simple and very accurate, this direct method is very time-consuming, labor-intensive, invasive, ex situ and destructive [Lunt et al., 2005].

2.2.2 Dielectric methods

2.2.2.1 Water content and permittivity relationships

The real part of the relative permittivity of the free water is approximately 80, while the relative permittivity of air is 1 and for the common soil constituents, the relative permittivity ranges from 3 to 10. Therefore, this high contrast between these permittivities allows the volumetric soil water content (VSWC) determination with electromagnetic methods [Huisman et al., 2003].

There are a lot of relationships available in the literature. In this thesis, two of the most used are presented.

The most used one is the empirical petrophysical relation of Topp to estimate the soil moisture from its relative dielectric permittivity $\varepsilon_r = \frac{\varepsilon}{\varepsilon_0}$ [Topp et al., 1980]. This relation is defined as

$$\theta = -5,3 \times 10^{-2} + 2,92 \times 10^{-2}\varepsilon_r - 5,5 \times 10^{-4}{\varepsilon_r}^2 + 4,3 \times 10^{-6}{\varepsilon_r}^3 \tag{2.9}$$

An other commonly used relationship between the dielectric permittivity and the volumetric water content is described by Ledieu et al. [1986]:

$$\theta = a\sqrt{\varepsilon_r} + b \tag{2.10}$$

where a and b are calibration parameters. It is important to note that the calibration equations between θ and ε_r are usually derived using TDR [Huisman et al., 2003].

2.2.2.2 Time Domain Reflectometry

This in situ non-destructive and indirect method was developed by Davis and Chudobiak in 1975. This method allows to determine the relative dielectric permittivity using two simple electrodes inserted into the material [Noborio, 2001].

Principles

The TDR method determines the relative dielectric permittivity by measuring the propagation time of emitted electromagnetic waves. These electromagnetic waves generated by a pulse generator propagate through a coaxial cable to a TDR probe with parallel rods of known length. At the end of the probe, the launched electromagnetic pulses are reflected back to their source and their amplitude are measured thanks to an oscilloscope and time-related by a high-precision chronometer. For each material discontinuities, an impedance variation is induced and creates a partial or total reflection of the signal, which is recorded by the oscilloscope in the time-domain [Bielders and Javaux, 2019; Noborio, 2001].

Since the pulse has to make a return trip, the path length is twice the length of the rods and the propagation velocity of the pulse is expressed by:

$$V = \frac{2L}{\Delta t} \tag{2.11}$$

where Δt is the transit time and L the length of the rods. By combining this equation with Equation (2.6), the expression of the dielectric permittivity is found as

$$\varepsilon_r = \left(\frac{c\Delta t}{2L}\right)^2 \tag{2.12}$$

with c being the velocity of light in free space [Dalton and Van Genuchten, 1986].

Figure 2.4 illustrates a typical signal in the TDR application. In this example, $\Delta t = t_c - t_b$ is the time taken by the wave to make a back and forth into the rods of the probe and is used to determine the wave velocity.

However, TDR is time-consuming and is prone to error due to air gaps between the probes and the soil if TDR is carelessly introduced into the soil [Lunt et al., 2005]. Also, the small sampled volume induces a representativeness issue.

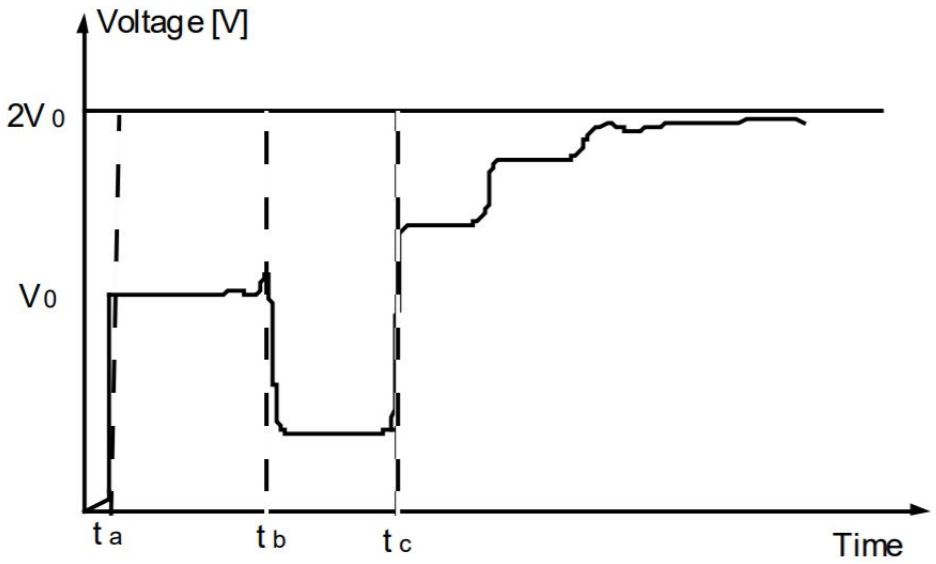

Figure 2.4 – Typical signal recorded in TDR applications. From [Bielders and Javaux, 2019]

2.2.2.3 Capacitance

This method uses an oscillating electrical circuit and a resonance frequency reader into the soil. To understand this method, lets remind that for a capacitor composed of two parallel plates with a surface A, the capacitance C is equal to:

$$C = g\frac{\varepsilon_0 \varepsilon_r A}{d} \tag{2.13}$$

where g is a corrective geometric function accounting for the side effect in the electrical field and d is the distance between the plates. Therefore, a relation exists between the capacitance and the relative dielectric permittivity of the medium between the plates.

The measurement of this capacitance can be achieved by the integration of a LC circuit. This circuit will induce an oscillating alternative current. The oscillating frequency is given by the relation:

$$f_r = \frac{1}{2\pi\sqrt{LC}} \tag{2.14}$$

where L is the inductance of the coil, in Henries. This frequency can be measured and, therefore, the capacitance can be deduced [Bielders and Javaux, 2019].

In practice, a RLC circuit is considered. Indeed, the dielectric losses of the soil are taken into account by considering the soil as a resistor.

2.2.2.4 Ground-penetrating radar

Ground-penetrating radar (GPR) methods are indirect dielectric methods. These methods can be on ground, as well as off ground and allow the determination of the electrical conductivity σ or the relative dielectric permittivity ε_r of the medium.

Since the scope of this thesis is to demonstrate the validity of a drone-borne GPR for soil moisture mapping, a bibliographic study of GPR is presented below.

2.3 Ground-penetrating radar methods

GPR methods are based on non-invasive geophysical measurements at the field scale and allow to break the gap between the large scale remote-sensing and small scale invasive methods [Minet et al., 2012; Klotzsche et al., 2018].

Most commonly used bistatic systems are composed of an antenna acting as transmitter and an other one acting as receiver. The transmitter one radiates short electromagnetic waves at high frequencies, while the receiver antenna measures the resulting signal as a function of time [Huisman et al., 2003]. This resulting signal contains the subsurface signature and through its analysis, subsurface parameters can be determined [Lavoué, 2014]. If a single antenna is used as both transmitter and receiver, the system is called monostatic.

Some parameters are important to consider, such as resolution and penetration depth of the GPR signal. The resolution is determined by the period of the pulse which is controlled by the bandwidth. Consequently, resolution increases with increasing center frequency. The depth penetration of the signal measured is highly sensitive to the soil conductivity and the

center frequency. In application, in sandy soil with poor cation-exchange capacity and low water retention capacity, the penetration depth will be much higher than in clays or silty sands [Huisman et al., 2003].

Several methods allow to retrieve the soil surface dielectric permittivity and, therefore, its soil water content.

2.3.1 Common midpoint Sounding (CMP)

This multi-offset reflection method allows to estimate the radar signal velocity versus depth in the ground by varying the distance between the antennas stepwise and by measuring the change of the travel time of the reflections. In this method, a bistatic antenna system is used, and both antennas are moved while keeping a common midpoint. Wide Angle Reflection and Refraction (WARR), is a similar approach where only one antenna is moved, can also be used [Annan, 2012]. Figure 2.5 illustrates the CMP method. With CMP, the reflected waves can be used to calculate the soil moisture using:

$$v_{\text{soil}} = \frac{2\sqrt{d^2 + (0.5a)^2}}{t_{\text{rw,a}}} \tag{2.15}$$

with d the depth of the scattering object, a the antenna separation, $t_{\text{rw,a}}$ the arrival time of the reflected waves with zero-time correction and v_{soil} the average velocity to the reflecting layer. The obtained radar wave velocity is then converted to dielectric permittivity using Equation (2.6) [Huisman et al., 2003; Lunt et al., 2005; Annan, 2012].

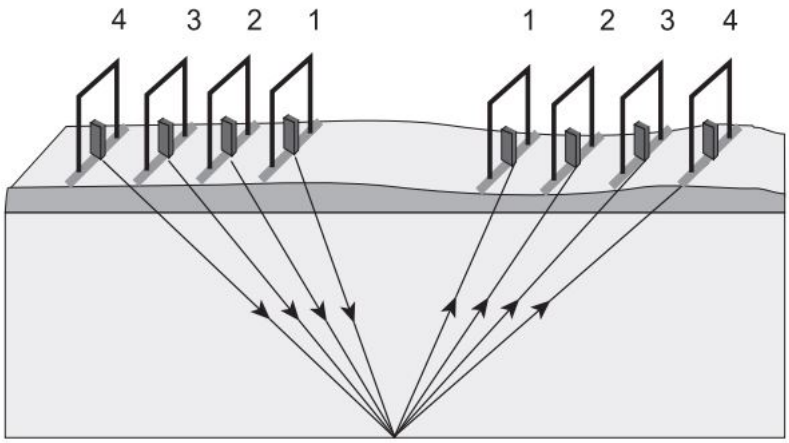

Figure 2.5 – Illustration of the common midpoint method configuration. From [Annan, 2012].

2.3.2 Common surface reflection method

This soil water content determination method uses antennas operated at some distances of the ground by installing them on a vehicle or a small flying air platform [Huisman et al.,

2003]. This method is based on the determination of the reflection coefficient of the soil-air interface. Some assumptions have to be considered to allow this method [Lambot et al., 2006b]:

1. Antennas are located in free space (air) and above on homogeneous half-space delimited by a plane interface
2. Antennas distortion effects can be considered as negligible
3. Reflection coefficient can be approximated by the reflection coefficient of the plane wave
4. Soil electric conductivity is assumed negligible
5. Soil magnetic permeability is assumed to be the free space permeability
6. Soil dielectric permittivity is frequency-independent

Hence, the measured parameter is the reflection coefficient of the soil surface interface, noted R. Once measured, this coefficient is a Dirac's delta function in the time domain whose amplitude is equal to the ratio between the backscattered (E_s) and incident (E_i) electric fields. For a normal incidence plane wave, the reflection coefficient is related to the soil permittivity as:

$$R = \frac{1 - \sqrt{\varepsilon_r}}{1 + \sqrt{\varepsilon_r}} \tag{2.16}$$

where ε_r is the relative dielectric permittivity. Therefore, this can be redefined as:

$$\varepsilon_r = \left(\frac{1 - R}{1 + R}\right)^2 \tag{2.17}$$

The reflection coefficient R is generally derived from the measured amplitude of the surface reflection, noted A, relative to the amplitude from a perfect eletrical conductor (PEC) at the same distance, noted A_{PEC} such as a metal plate (larger than the footprint of the radar) [Lambot et al., 2006b; Huisman et al., 2003]. Indeed, the ratio between the reflection coefficient at the soil surface and at the PEC interface (R_{PEC}) can be expressed as :

$$\frac{R}{R_{\text{PEC}}} = \frac{\frac{E_s}{E_i}}{\frac{E_{s,\text{PEC}}}{E_{i,\text{PEC}}}} \tag{2.18}$$

Because a PEC is a perfect reflector $R_{\text{PEC}} = -1$ and with the assumption that E_i is constant and that the measured amplitude A is directly proportional to E_s, the backscattered electric field (no antenna distortion effects), Equation (2.18) reduces to:

$$R = -\frac{E_s}{E_{s,\text{PEC}}} = -\frac{A}{A_{\text{PEC}}} \tag{2.19}$$

As a result, the determined relative dielectric permittivity can finally be expressed as:

$$\varepsilon_r = \left(\frac{1 + \frac{A}{A_{\mathrm{PEC}}}}{1 - \frac{A}{A_{\mathrm{PEC}}}} \right) \tag{2.20}$$

Figure 2.6 shows the relation between the measured reflection coefficient and the calculated soil moisture, assuming Topp's equation presented in Equation (2.9) [Huisman et al., 2003].

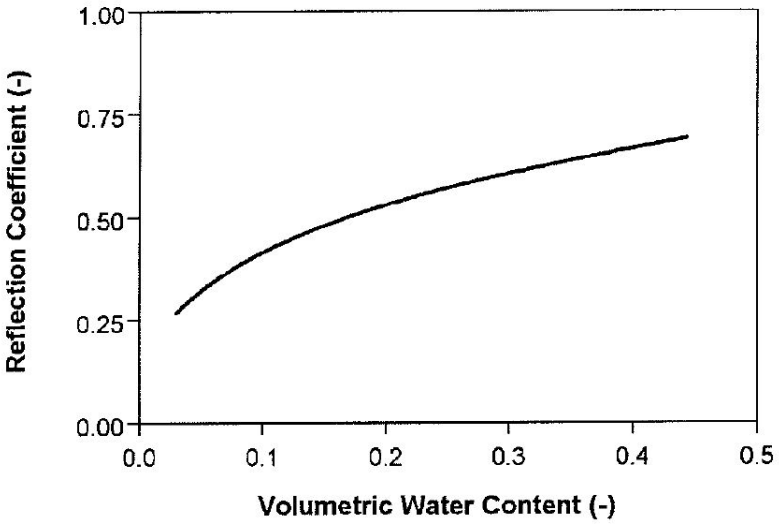

Figure 2.6 – Soil moisture and reflection coefficient relationship. The soil moisture was calculated from ε_r using Topp's equation (Equation (2.9)). From [Huisman et al., 2003].

It is important to note that soil roughness and the varying water volumetric content with depth cause significant scattering. Indeed, soil roughness is resulting in a decreasing reflection coefficient and leads to underestimations in soil moisture. The varying water content with depth can lead to both under- or over-estimations if not accounted for (see [Lambot et al., 2006b]).

Chanzy et al. [1996] determined the upper limit of surface roughness by using the Rayleigh criterion, i.e., a surface can be considered smooth if the Rayleigh criterion is satisfied:

$$h < \frac{\lambda}{(8 \cos \alpha_i)} \tag{2.21}$$

with h being the average height of soil irregularities, λ being the shorter wavelength of the incident pulse and α_i is the incident angle. This means that with lower frequencies, the sensitivity to roughness is smaller than with higher frequencies, and by this way, estimation errors due to soil roughness can be avoided [Huisman et al., 2003]. For instance, at 1 GHz the surface roughness must be below 0.0375m for the approximation of a smooth surface while at 500 MHz, the average soil irregularities must be below 0.075m.

Chapter 3

Model presentation

3.1 Full-wave inversion

Although off ground GPR measurements in the time domain using the surface reflection method have been used for estimating the volumetric water content, progress have been made in the past decade and allow to accounts for antenna effects [Klotzsche et al., 2018]. Notably, in [Lambot et al., 2004] an antenna-medium model was developed, in which a far field radar antenna is modeled using frequency dependent transmission and reflection coefficients combined with Green's functions, this last being the three dimensional Maxwell's equation solution for electromagnetic waves propagating in multilayered media.

3.1.1 Frequency domain radar equation

In the paper mentioned before, namely [Lambot et al., 2004], they set up a monostatic ultra wide band (UWB) stepped-frequency continuous wave (SFCW) radar using a vector network analyzer (VNA). The quantity measured by the VNA is the complex frequency dependent ratio between the returned signal and the emitted signal, noted $S_{11}(\omega)$ where ω represents the angular frequency. $S_{11}(\omega)$ is measured at the radar reference plane.

In order to describe the radar measurements, a radar equation accounting for antenna effects, antennas and medium interactions, as well as three-dimensional wave propagation in multilayered media was introduced [Lambot et al., 2004; Lambot and André, 2014]. This equation, expressed in the frequency-domain, can be applied for near-field as well as far-field conditions [Wu et al., 2019]. This equation is expressed as [Lambot and André, 2014]:

$$S(\omega) = \frac{b(\omega)}{a(\omega)} = R_i(\omega) + \mathbf{T_s}(\mathbf{I_N} - \mathbf{G^0 R_s})^{-\mathbf{1}}\mathbf{G T_i} \tag{3.1}$$

where

$$\mathbf{T_i} = \begin{bmatrix} T_{i,1}(\omega) & T_{i,2}(\omega) & \dots & T_{i,N}(\omega) \end{bmatrix}^T$$

$$\mathbf{T_s} = \begin{bmatrix} T_{s,1}(\omega) & T_{s,2}(\omega) & \dots & T_{s,N}(\omega) \end{bmatrix}$$

$$\mathbf{R_s} = \text{diag}\left(\begin{bmatrix} R_{s,1}(\omega) & R_{s,2}(\omega) & \dots & R_{s,N}(\omega) \end{bmatrix} \right)$$

$$\mathbf{G} = \begin{bmatrix} G_{11}(\omega) & G_{12}(\omega) & \dots & G_{1N}(\omega) \\ G_{21}(\omega) & G_{22}(\omega) & \dots & G_{2N}(\omega) \\ \vdots & \vdots & & \vdots \\ G_{N1}(\omega) & G_{N2}(\omega) & \dots & G_{NN}(\omega) \end{bmatrix}$$

$$\mathbf{G}^0 = \begin{bmatrix} G^0_{11}(\omega) & G^0_{12}(\omega) & \dots & G^0_{1N}(\omega) \\ G^0_{21}(\omega) & G^0_{22}(\omega) & \dots & G^0_{2N}(\omega) \\ \vdots & \vdots & & \vdots \\ G^0_{N1}(\omega) & G^0_{N2}(\omega) & \dots & G^0_{NN}(\omega) \end{bmatrix}$$

$S(\omega)$ is the measured signal by the VNA, $R_i(\omega)$ is the global reflection coefficient of the antenna for field incident from the radar reference plane onto the source point and corresponds to the antenna response in free space conditions, $T_{s,1}(\omega)$ is the global transmission coefficient for field incident from the field onto the radar reference plane of the antenna, $T_{i,1}(\omega)$ is the global transmission coefficient for field incident from the radar reference plane onto the source point, $R_{s,1}(\omega)$ is the global reflection coefficient for field incident from the layered medium onto the field point, $\mathbf{I_N}$ is the N-order identity matrix (N being the number of source and field points). The Green's function is determined using a recursive scheme and a computation of the global reflection coefficients of the three dimensional multilayered medium in the spectral domain [Lambot and André, 2014]. To return in the spatial domain, a semi-infinite integral is numerically evaluated [Lambot et al., 2007].

In the far-field conditions, which are satisfied if an antenna height threshold of $h_0 = 1.2D$ is respected, with D being the maximum antenna aperture, a homogeneous wave field distribution is assumed for the backscattered fields (see Tran et al. [2013]). Hence, the antenna can be considered by an infinitesimal point, acting as source and receiver. This simplifies Equation (3.1) to (3.2) [Lambot et al., 2004; Lambot and André, 2014].

$$\begin{aligned} S(\omega) &= \frac{b(\omega)}{a(\omega)} \\ &= R_{\text{i}}(\omega) + \frac{T_{\text{s},1}(\omega) G_{11}(\omega) T_{\text{i},1}(\omega)}{1 - R_{\text{s},1}(\omega) G_{11}(\omega)} \end{aligned} \tag{3.2}$$

where $R_i(\omega)$ is directly measurable in free space by the VNA because there $G_{xx}(\omega) = 0$ and hence in such conditions, $S_{11}(\omega) = R_i(\omega)$. Then, $T(\omega) = T_{s,1}(\omega)T_{i,1}(\omega)$ is defined as the transmitting-receiving response function. $T(\omega)$ and $R_{s,1}(\omega)$ can be determined with a system

of linear equations, considering two model configurations at different heights above a metal sheet [Lambot et al., 2004].

Therefore, the wave propagation between the radar reference plane and the source point or the field point can be modeled as complex frequency-dependent global coefficients such as these transmission and reflection coefficients. This is illustrated in Figure 3.1 from Lambot and André [2014]. This linear model is relying on the linearity of Maxwell's equations. The different global coefficients allow to determine the internal transmissions, which implicitly lead to antenna-medium interactions.

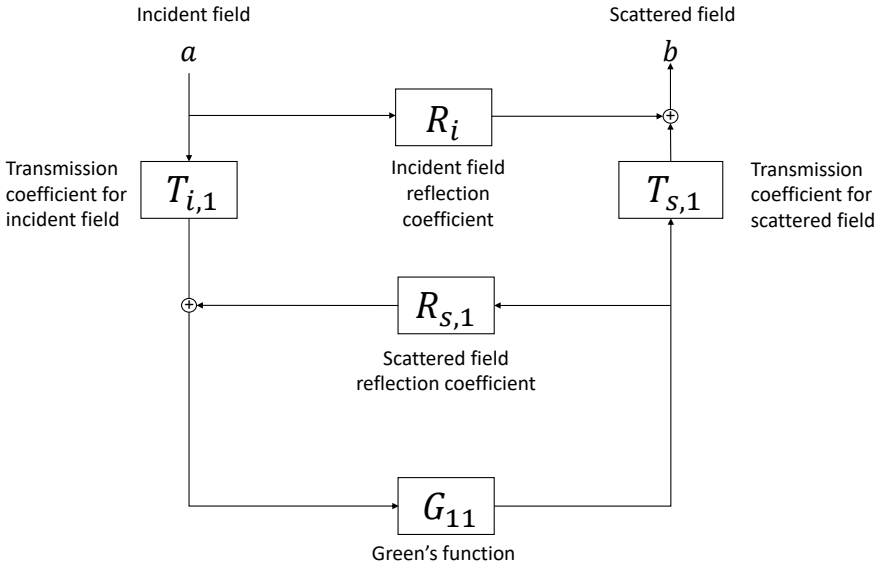

Figure 3.1 – Wave propagation description in the far-field antenna model, using global transmission and reflection coefficient. From [Lambot et al., 2004; Lambot and André, 2014]

3.1.2 Calibration

Calibration is necessary to apply the model and further, to proceed to the determination of the soil permittivity. This calibration consists in the determination of the global reflection and transmission coefficients [Lambot et al., 2004; Lambot and André, 2014]. These global coefficients can be determined with a linear system of equations using Equation (3.2) for different configurations (noted k) in far field conditions. Well defined model configurations are used, with the antenna situated at different heights above a Perfect Electric Conductor (PEC) large enough to be considered as infinite. Therefore, the Green's functions can be computed and $S_{11}(\omega)$ can be measured [Lambot et al., 2006a].

Theoretically, three different configurations are enough for the determination of $R_i(\omega)$, $R_s(\omega)$ and $T(\omega)$. However, for some frequencies, the solution is not numerically stable due to the correlation between equations in the system when a wide frequency range is used.

In order to enhance the calibration, a higher amount of configurations is set up, thereby leading to an over-determined system [Lambot et al., 2006a]. To solve this over-determined system, Lambot et al. [2006a] proposed to linearize Equation (3.2) as:

$$S_{11,k} = R_i + S_{11,k} G_{xx,k} R_{s,1} + G_{xx,k}(T - R_i R_{s,1}) \tag{3.3}$$

and the system can be written in the matrix form :

$$\mathbf{b} = \mathbf{A}\mathbf{x} \tag{3.4}$$

where

$$\mathbf{b} = \begin{bmatrix} S_{11,1} \\ \vdots \\ S_{11,k} \\ \vdots \\ S_{11,n} \end{bmatrix}$$

$$\mathbf{A} = \begin{bmatrix} 1 & S_{11,1} G_{xx,1} & G_{xx,1} \\ \vdots & \vdots & \vdots \\ 1 & S_{11,k} G_{xx,k} & G_{xx,k} \\ \vdots & \vdots & \vdots \\ 1 & S_{11,n} G_{xx,n} & G_{xx,n} \end{bmatrix}$$

$$\mathbf{x} = \begin{bmatrix} R_i \\ R_{s,1} \\ T - R_i R_{s,1} \end{bmatrix}$$

Finally, this vector of unknowns is computed in the least square sense as

$$\mathbf{x} = (\mathbf{A}^{\mathrm{H}}\mathbf{A})^{-1}\mathbf{A}^{\mathrm{H}}\mathbf{b} \tag{3.5}$$

where H is denoting for Hermitian transpose.

When a calibration above a PEC is not possible, a configuration at different heights above a body of water can work too, as it constitutes as well a homogeneous medium with known electrical properties.

When the data are collected by an antenna set up on a drone (UAV), Wu et al. [2019] advises to calibrate the antenna mounted on the drone to account for antenna-drone interactions.

3.1.3 Data inversion

When the radar equation is known thanks to the calibration process, the measured Green's functions can be calculated with the following equation

$$G_{xx} = \frac{S(\omega) - R_i(\omega)}{T(\omega) + S(\omega) R_{s,1}(\omega) - R_i(\omega) R_{s,1}(\omega)} \tag{3.6}$$

For retrieving the surface soil moisture, the full-wave inversion is performed on the Green's function in the time domain, focusing on the surface reflection [Lambot et al., 2006b]. Thus, both the measured and modeled Green's function in the frequency domain have to be transformed in the time domain using the inverse Fourier transform :

$$g_{xx}^{\uparrow}(t) = F^{-1}\{G_{xx}(\omega)\} = \frac{1}{2\pi}\int_{-\infty}^{\infty} e^{i\omega t} G_{xx}(\omega)\,\mathrm{d}\omega \tag{3.7}$$

where ω is the angular frequency, t is time and $i = \sqrt{-1}$. Then, a time window can be defined to focus on the surface reflection only, as shown in Figure 3.2.

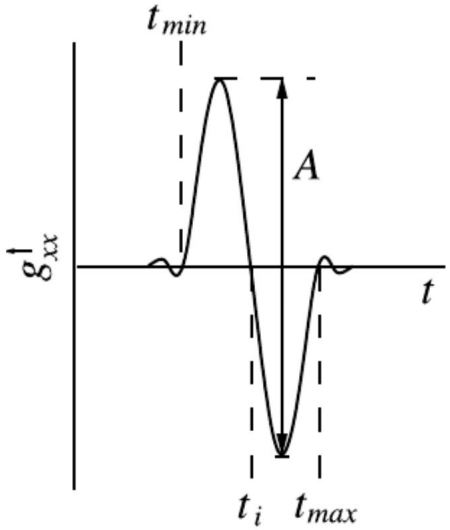

Figure 3.2 – Radar signal in the time domain where antenna effects have been filtered out. t_{min} and t_{max} define the time window focusing on the surface reflection. t_i allows to approximate the time corresponding to the surface interface. From [Lambot et al., 2006b].

Finally, the objective function to be minimized is formulated in the least-square sense to define the inverse problem and is expressed as:

$$\phi(\mathbf{b}) = (\mathbf{g}_{xx}^{\uparrow *}(t) - \mathbf{g}_{xx}^{\uparrow}(\mathbf{b},t))^{\mathrm{T}}(\mathbf{g}_{xx}^{\uparrow *}(t) - \mathbf{g}_{xx}^{\uparrow}(\mathbf{b},t)) \tag{3.8}$$

where $\mathbf{g}_{xx}^{\uparrow *}(t)$ and $\mathbf{g}_{xx}^{\uparrow}(\mathbf{b},t)$ are, respectively, the measured and modeled Green's functions in the time domain, t is the time variable and $\mathbf{b} = [\mathbf{h}_0, \boldsymbol{\varepsilon_r}]$ is the parameter vector to be found [Lambot et al., 2006b]. This objective function has a complex topography with several local minima. The objective function is minimized by using the Nelder-Mead simplex algorithm [Lambot et al., 2006a].

An initial guess for the antenna height, denoted h_0, can be derived from t_i, the root between the positive and the negative peaks of the surface reflection illustrated in Figure 3.2. Concerning the dielectric permittivity, an arbitrary value can be chosen between $2,5 \leq \varepsilon \leq 25$ as initial guess [Lambot et al., 2006b].

Since conducting several thousands of inversions using local optimization is relatively time

consuming, an other approach is to pre-calculate Green's functions in a look-up table (LUT). Hence, the objective function is calculated in the full parameters space and an optimization is achieved by comparing all the measured Green's functions with the precomputed Green's functions stored in the LUT. This LUT allows a fast and robust inversion and only has to be calculated once for a given radar configuration and inverse problem [Wu et al., 2019].

3.2 Soil moisture interpolation

Once the dielectric permittivity of each position is obtained by inversion, the corresponding soil water content is determined using Topp's relation (Equation (2.9)). Further, a soil moisture map is produced by the interpolation of these measured points using ordinary kriging. Ordinary kriging gives the optimal predictions with the assumption that the process is second-order stationary and with a normal distribution and that the observed values are realizations of a stationary stochastic process of fairly simple structure. The observed values are first used to estimate the unknown parameters and to compute the empirical semivariogram. Further, the observed values, the semivariogram and parameters are used to produce the Best Linear Unbiased Predictor (BLUP) [Ryu et al., 2002].

In other words, ordinary kriging is a local prediction method using a weighted linear combination of the neighbour values of θ, based on the spatial dependence given by the semivariogram. The simplified equation of the ordinary kriging model is given by:

$$\theta_p = \sum_{i=1}^{n} \lambda_i \theta_i \tag{3.9}$$

where θ_p is the predicted soil moisture, λ_i is the kriging coefficient (weight) for θ_i and θ_i is the soil moisture derived from inversion modelling.

Chapter 4

Materials and methods

4.1 Study site

4.1.1 Soil characteristics

The study site is located in Ottignies-Louvain-la-Neuve, in the province of Brabant Wallon, Belgium. The site location is presented in an orthophotoplan in Figure 4.1. This site is part of the Ferme de Lauzelle, which belongs to the Université catholique de Louvain. The area of the Ferme de Lauzelle considered in this thesis (delimited in red in Figure 4.1) is approximately 0,76 ha. In this figure, the contour lines were mapped and a digital elevation model (DEM) was focused on the studied area.

The contour lines are derived from a digital elevation model from [Geoportail de la Wallonie, 2014] while the mapped DEM is derived by high resolution photogrammetry from drone-borne photography and processed using Agisoft Methashape software. The drone used for photography acquisition was a DJI Phantom 4 pro in an automated flight.

The elevation of the study site is ranging from 133 to 136.5 meters above the average sea level with the Second General Levelling (EPSG:5710) being the altimetric reference [Geoportail de la Wallonie, 2014]. Thanks to the DEM, an heterogeneous slope direction is visible and hence, an anisotropic drainage behavior can be expected. This topography heterogeneity makes the study site very interesting since higher moisture values are expected at the bottom of the visible slope, as in the upper middle of the field, where a lower area is emerging.

Figure 4.2 is a derivation of Figure 4.1 and shows the slopes heterogeneity in the site. Indeed, since water behavior is not independent of such factors, it is important to clearly define them.

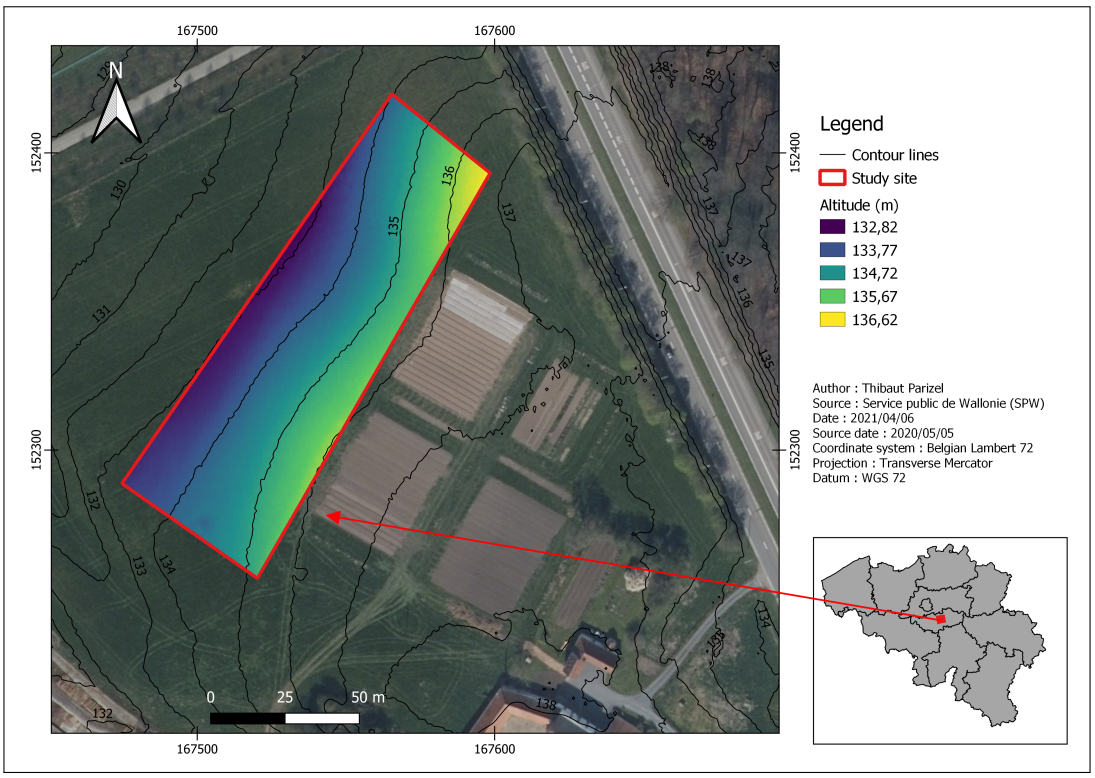

Figure 4.1 – Cartographic representation of the Ferme de Lauzelle site.

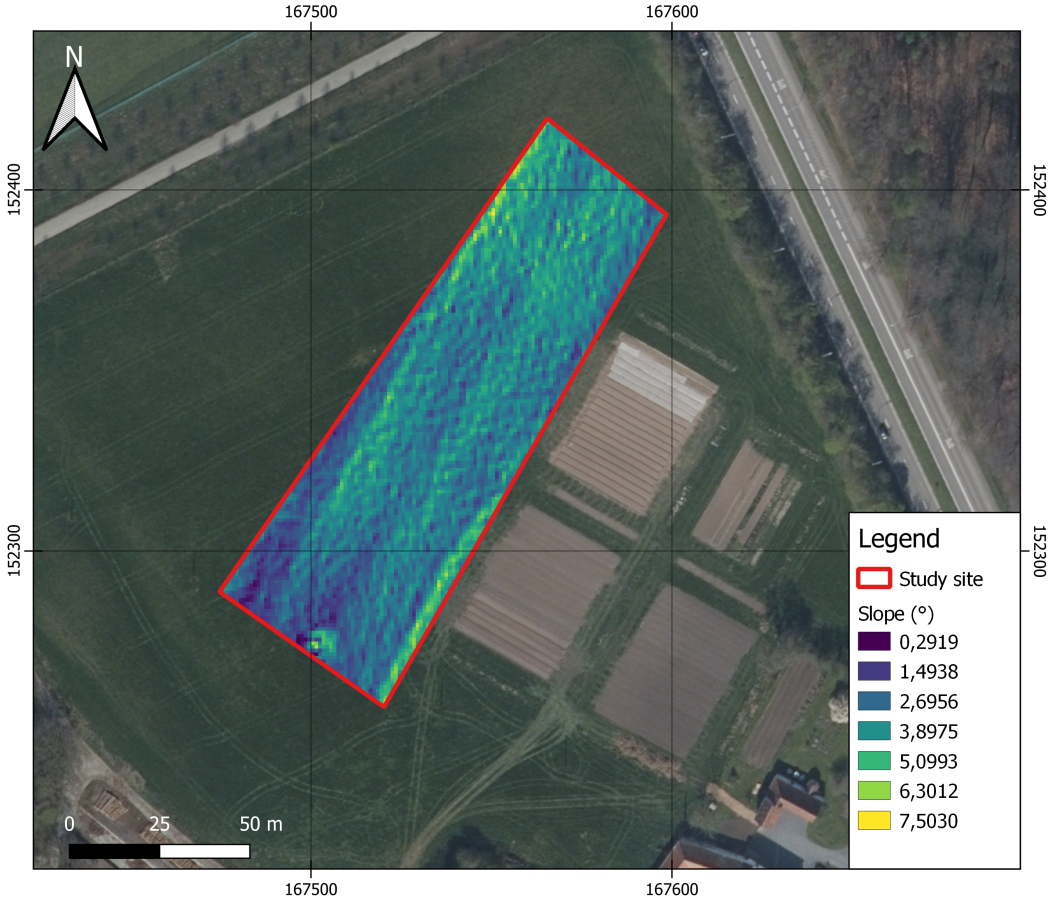

Figure 4.2 – Slopes present in the Ferme de Lauzelle site, derived from drone-borne photogrammetry.

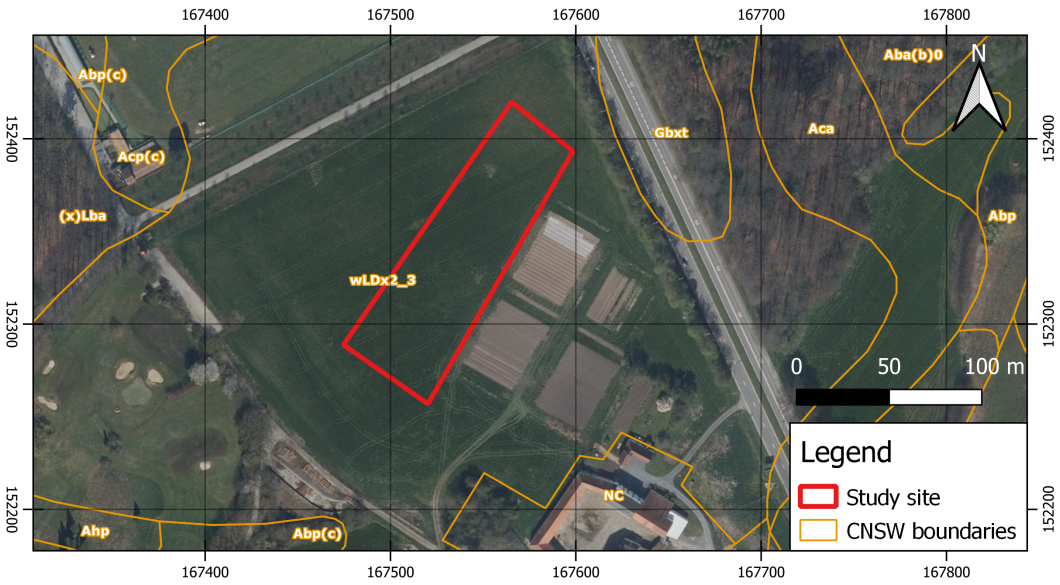

Figure 4.3 – Soil types in the study site according to the numerical map of Walloon soils (CNSW). From [Geoportail de la Wallonie, 2014]

Figure 4.3 describes, according to the numerical map of Walloon soils (CNSW), that the soil of the study site belongs to the wLDx2_3 category, which means that the soil substrate is sandy-clay (w), the textural material is sandy-silty (L) with a moderate natural drainage (D), with a soil profile development undefined (x) and with a substrate beginning between 20 cm and 80 cm deep.

4.1.2 Climate

In this location, climate can be defined as oceanic temperate [Climat.be, 2013]. The meteorological data of the nearest meteostation (located at Lasne-Chapelle-Saint-Lamber) are available in Figures 4.4 and 4.5.

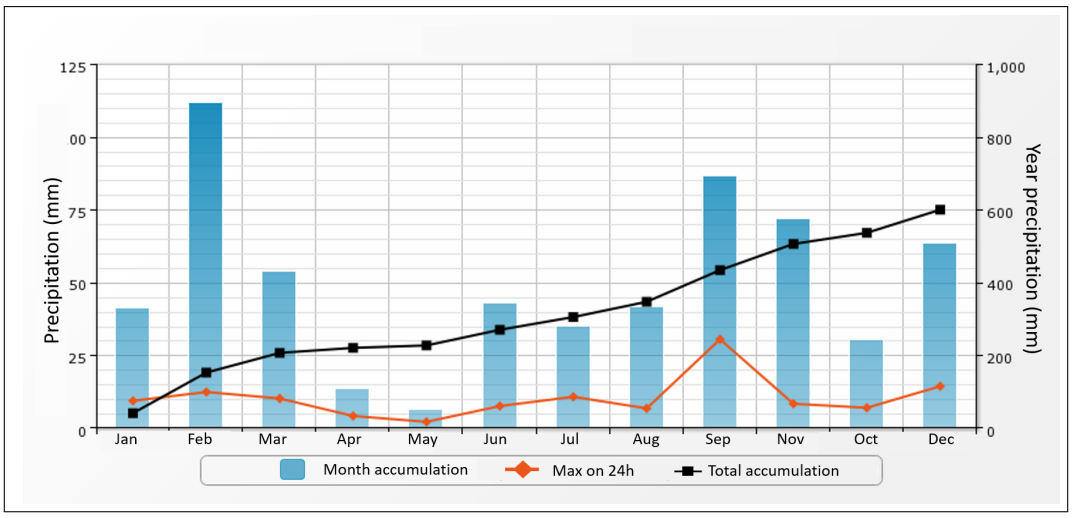

Figure 4.4 – Recorded precipitation data of 2020 at Lasne-Chapelle-Saint-Lambert. From [Infoclimat, 2021].

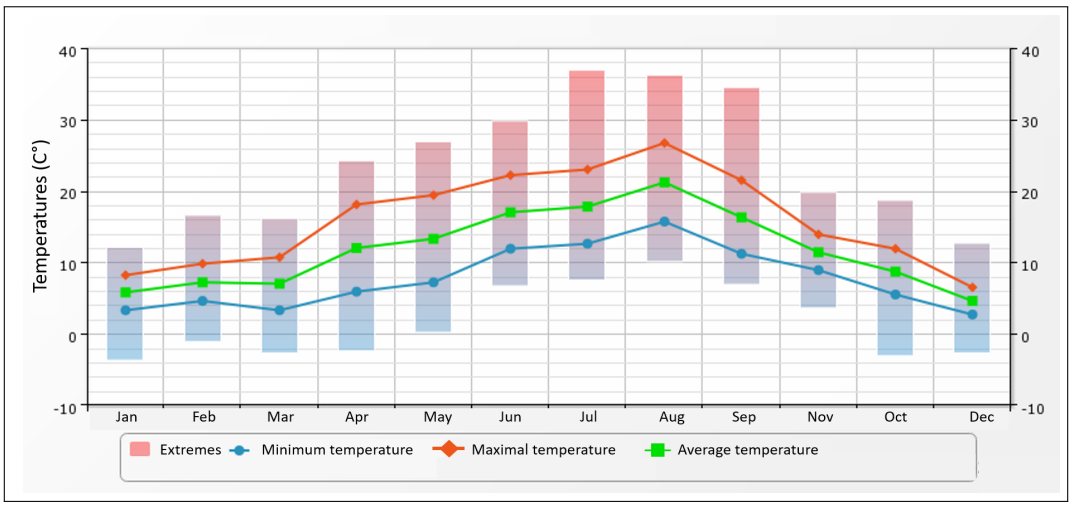

Figure 4.5 – Recorded temperature data of 2020 at Lasne-Chapelle-Saint-Lambert. From [Infoclimat, 2021].

4.2 Soil moisture sensing by ground penetrating radar

4.2.1 Ground penetrating radar set up

4.2.1.1 Radar and control system

The radar and its control system is composed of several equipments:

- A lightweight vector network analyzer (VNA): Planar R60 from Copper Mountain Technologies® (Indianapolis, USA)
- A monostatic system antenna
- An Intel® compute stick
- A power bank
- A smartphone

The dimensions of the R60 VNA are 130x65x28mm, it weights 350 g and is therefore quite convenient for being set up on a small aerial vehicle. This R60 VNA is a USB-powered 50 Ω VNA and can measure reflection coefficients from 1 MHz to 6 GHz. This range is entirely covering the traditional GPR frequencies. This VNA also allows a direct connection with the transmitting and receiving monostatic antenna without test cable, which eliminates measurements uncertainties inherent to the cable. The measurements speed of the VNA reaches 100 µs per frequency. To ensure measurement repeatability in full-wave inversion, VNA has to be calibrated using Short-Open-Load (SOL) calibration standards [Wu et al., 2019].

The Intel® computer stick provides a platform for controlling the radar system, such as the start and stop of measurements, operating frequency range and frequency step. Further,

the measured data are saved in a fixed directory file on this microcomputer. Its dimensions are 125x38x12mm with a weight of 60g. The microcomputer run on Windows 10 system. The powering is provided by a power bank through a micro-USB connector fed with 5V [Wu et al., 2019].

The smartphone device allows to remotely control the computer. Indeed, a local Wi-Fi network is generated by the microcomputer and is captured by the user with the smartphone [Wu et al., 2019].

4.2.1.2 Drone-borne GPR

A picture of the drone-borne GPR setup is shown in Figure 4.6. The GPR system is mounted on a RPAS X8 drone developed by RCTakeOff based in Overijse, Belgium. The payload of the drone can reach 7 kg thanks to the 8 motors distributed on 4 arms. The model can support light rain and wind up to 100 km/h [RCTakeOff, 2021]. In field application, a supplementary battery is taken to enhance the measurement time.

The used antenna for the drone-borne GPR is a 50 centimeters long half-wave dipole (VHA 9103) from Schwarzbeck (Schönau, Germany). The operating frequency range is 30 - 300 MHz and weights 930 g.

Figure 4.6 – Drone-borne GPR set up used for field measurements including the antenna linked to a VNA, GPS device, microcomputer and its power bank

For this drone setup, microcomputer, power blank, VNA, antenna and dGPS-related captor are fixed on a lightweight non ferrous material minimising electromagnetic perturbations.

4.2.1.3 All-terrain vehicle holding GPR

Figure 4.7 – All-terrain vehicle holding the GPR system, including the antenna linked to a VNA, GPS device, microcomputer and its power bank.

A second acquisition setup was the use of an all-terrain vehicle as illustrated in Figure 4.7. In this setup, the GPR system, including the antenna linked to a VNA, dGPS-related device, microcomputer and its power bank, is fixed on a non-magnetic wooden structure to avoid electromagnetic perturbations. The antenna used for this setup is a logarithmic periodic antenna (UHALP 9108A) from Schwarzbeck, but the dipole antenna can also be used with a similar configuration. The operating frequency range is from 250 to 2400 MHz [Schwarzbeck, 2021].

This all-terrain setup will further allow the validation of the drone-borne GPR results by comparison.

4.2.1.4 Antennas

Calibration of the antennas

To retrieve the measured Green's functions and perform inversion, antennas have to be calibrated to determine its global reflection and transmission coefficients (see Equation (3.2)). This can be achieved by performing several measurements above a perfect electric conductor such as a copper plane, large enough to be considered as infinite. In this thesis, calibration was carried out in the GPRLouvain lab, with 6 measurements at different distances above a large copper sheet (3m $\times$ 3m).

In total, three calibrations were achieved: a first for the dipole antenna above the copper sheet in the lab, a second with the same antenna but mounted on a drone above a water body and a third above the copper sheet with the log periodic antenna. The reason of the calibration with the water pond is that, given the relatively low frequencies and poor directivity of the dipole, copper sheet in the lab is not large enough and several objects of the lab can interfere

when using lower frequency. The calibration of the logarithmic antenna was performed in lab with the copper plane. The results are satisfying since the frequency range is slightly higher and the antenna is very directive. In this case, the 3m x 3m copper plane is large enough

Because the dipole antenna was calibrated in the more or less same frequency range above the water body as with the copper sheet, their relative transfer functions (frequency-dependent transmission and reflection coefficients) can be compared, as shown in Figure 4.8. Nevertheless, some disparities are visible in those plots, which are expected to have significant impact on full-wave inversion [Wu et al., 2019].

These significant differences between the copper plane calibration and drone-borne calibration show the need to calibrate the antenna when mounted on the drone to include the drone-antenna interactions. Indeed, this drone is made from carbon and others metallic components that are conductive. In addition, the copper sheet in the lab is too small (ideally, the reflector should be 5 times larger than the wavelength) for that frequency range and extraneous objects in the lab affect the calibration (walls, sand box, ground, calibrations facilities,..). These interferences are showed by the higher value of R_i for the lab-calibration than for the water-calibration.

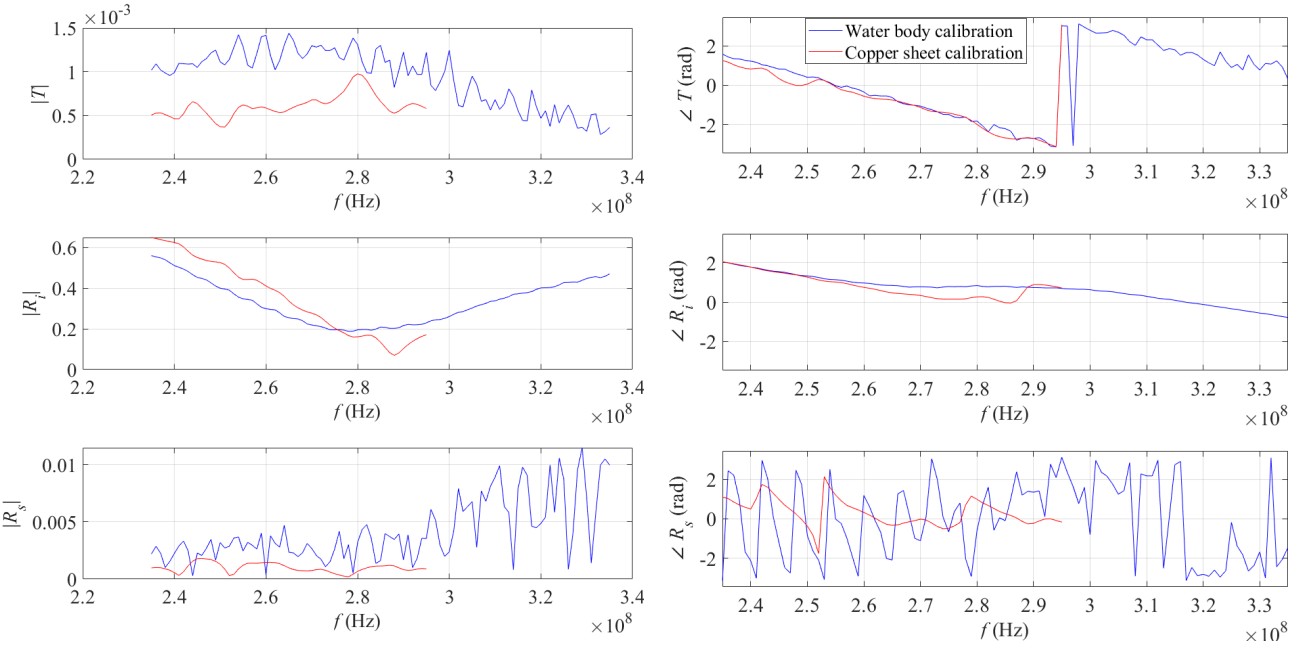

(a) Magnitude

(b) Phase

Figure 4.8 – Magnitude and phase of the dipole antenna characteristic functions for the copper sheet calibration and water body calibration.

Figure 4.9 shows the transfer characteristic functions of the Log periodic antenna. According to the specifications of the manufacturer, the Log antenna is much more directive than the dipole antenna. Moreover, the return loss, namely R_i is between 2 and 3 times lower than for the dipole antenna, which is very good given that it radiates much more energy, and the return loss for medium-backscattered field R_s is at least one order of magnitude lower than for the dipole antenna. It is important to note that the frequency range is not the same compared to the dipole antenna calibration.

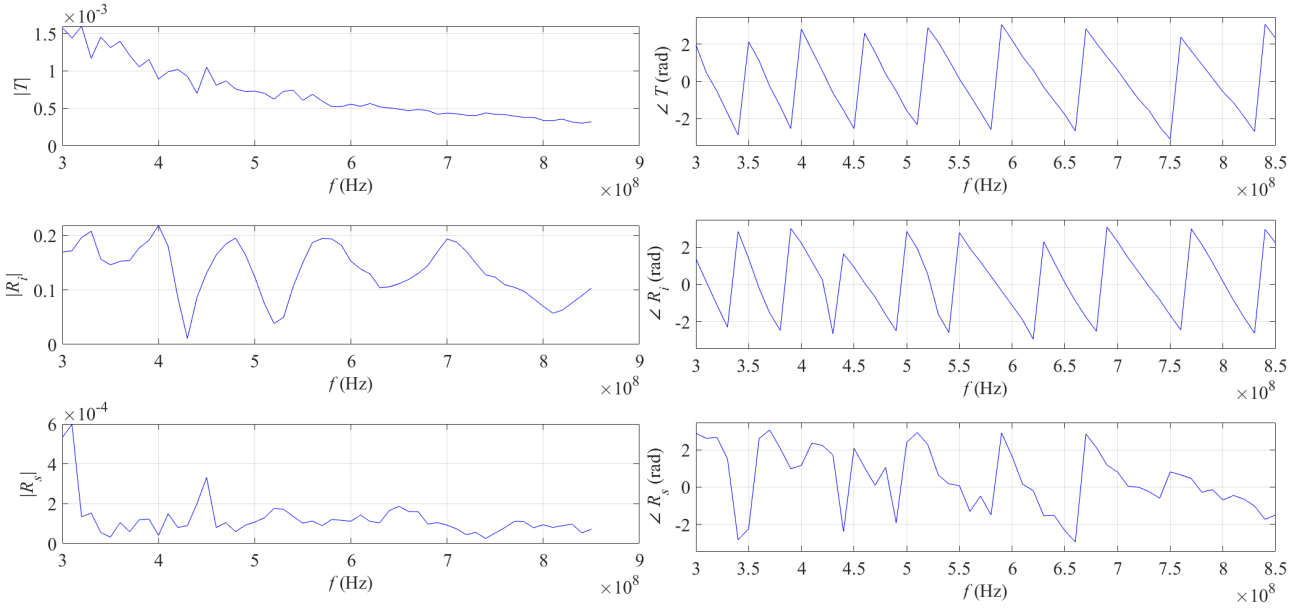

(a) Magnitude

(b) Phase

Figure 4.9 – Magnitude and phase of the Log periodic antenna characteristic functions for the copper sheet calibration

Radiation pattern

The directivity of the antenna is a measurement of its ability to direct its power towards a given direction and is a component of the gain [Orfanidis, 2002]. When this gain is plotted as a function of the direction, a radiation pattern is obtained [Vallozzi et al., 2016].

Such radiation patterns are generally provided by antenna constructors, as the one provided by Schwarzbeck presented in Figure 4.10 which describes the radiation patterns of the logarithmic-periodic antenna (UHALP 9108 A). The E-plane represents the plane of the electric field vector, while the H-plane represents the plane of the magnetic field vector. A first sight on these radiation patterns allows to see a directive behavior of the logarithmic antenna. In this figure, the radiation pattern of the antenna are presented for two frequency: 300 MHz and 600 MHz, both being contained in the used frequency window of the log-antenna.

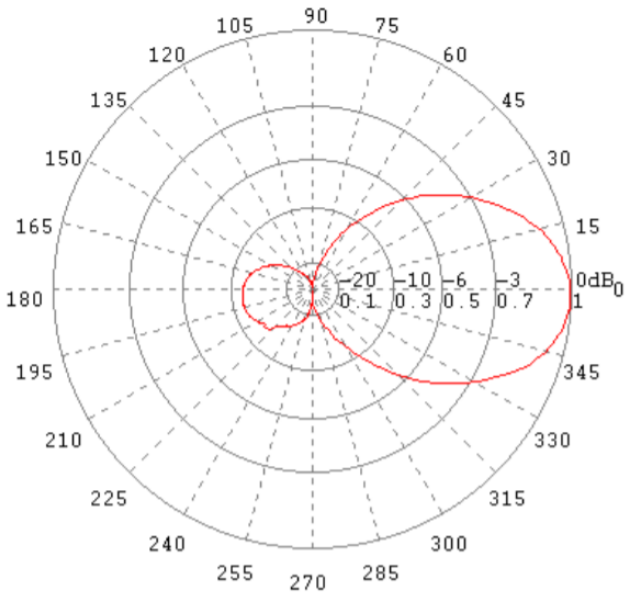

(a) E-Plane 300 MHz

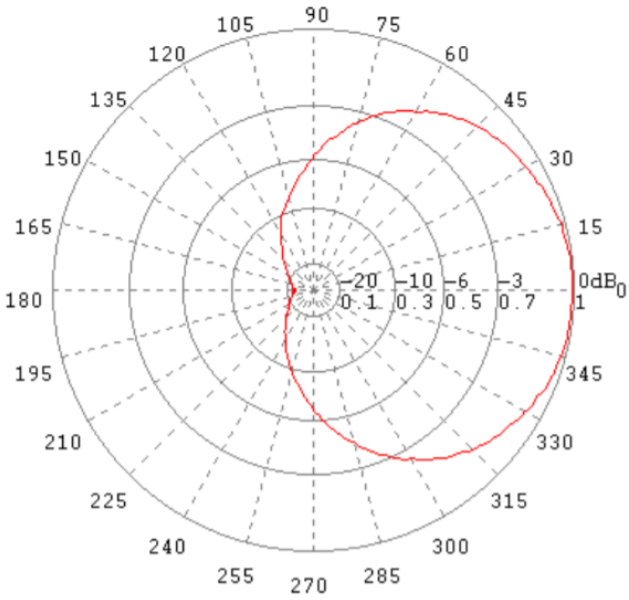

(b) H-Plane 300 MHz

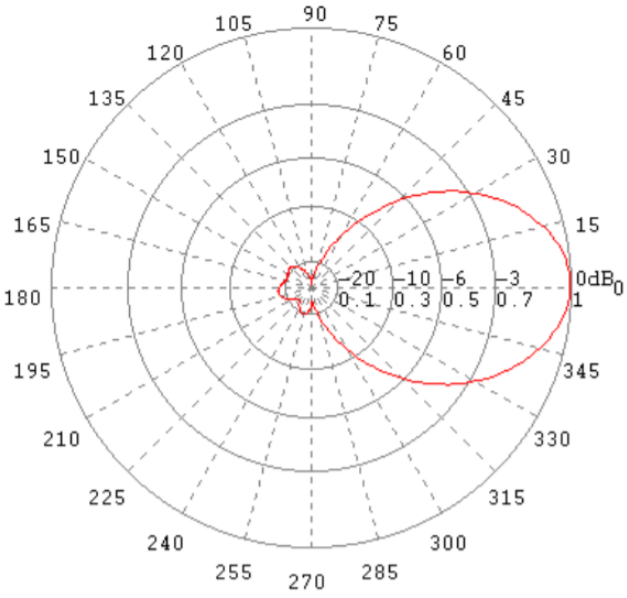

(c) E-Plane 600 MHz

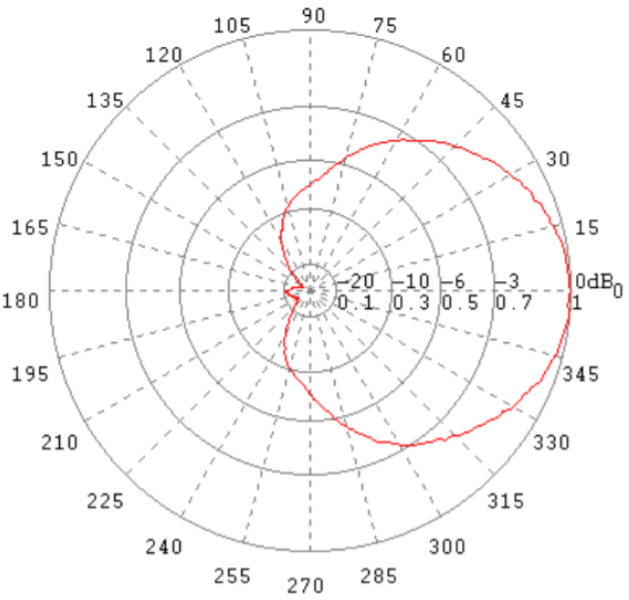

(d) H-Plane 600 MHz

Figure 4.10 – Radiation pattern for the UHALP 9108 A antenna. From [Schwarzbeck, 2021b].

The radiation pattern of the VHA 9103 being not provided by Schwarzbeck, the radiation pattern of the VHA 9105 dipole antenna, presented in Figure 4.11, will be considered as the radiation pattern of the VHA 9103 antenna. The VHA 9105 is similar to VHA 9103 but operates at higher frequencies. Generally, dipole antennas present similar shape of radiation pattern, which is therefore comforting for this assumption.

The radiation pattern in X-Z coordinates is close to an ideal isotropic field and its three dimensional shape is the so-called donut-shaped radiation pattern. Note that the H-plane radiation pattern is not provided by Schwarzbeck, but its directional pattern is circular.

The dipole antenna, with its donut-shaped radiation pattern, is far less directive than the

logarithmic antenna and thereby, caution must be emphasized during the calibration as it is more sensitive to extraneous object. The same is for the field measurements.

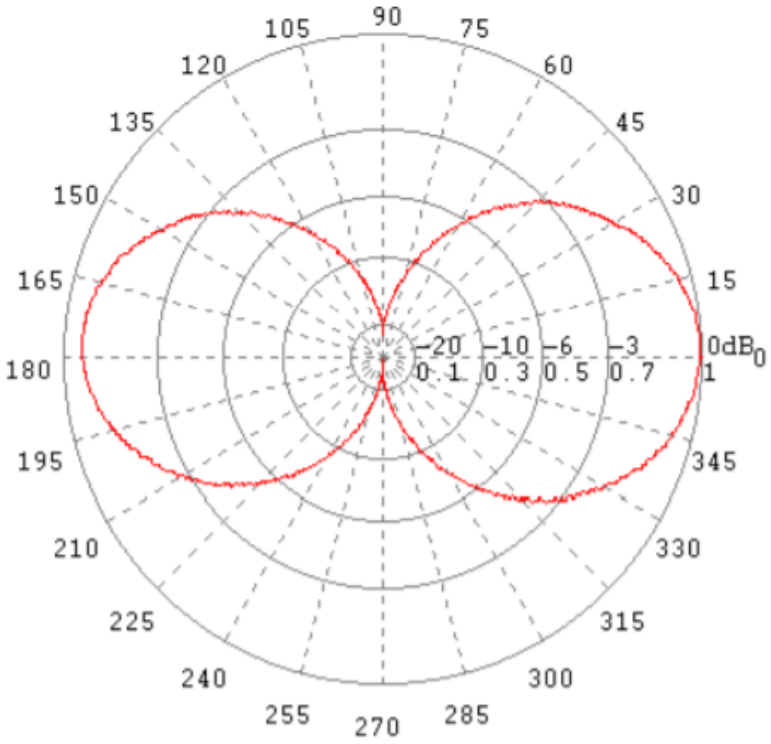

Figure 4.11 – E-plane radiation pattern for the VHA 9105 dipole antenna. From [Schwarzbeck, 2021a].

4.2.1.5 Differential GPS

To allow for an accurate positioning of the radar measurements, a REACH M+ UAV mapping kit developed by EMLID was used, with an expected accuracy of 1cm in horizontal coordinates. This kit includes an EMLID REACH RS+ GNSS receiver, a Reach M+ RTK GNSS module, a LoRa radio and a Tallysman multi-GNSS antenna. Such accuracy is permitted thanks to the RTK technology. The two receivers communicate with LoRa radio, Reach RS+ has an internal Lora radio while Reach M+ uses external radio which can be connected by USB port. The internal radio in Reach RS+ broadcasts RTK corrections while Lora radio of Reach M+ receives them [EMLID, 2021]. All GPS data are stocked in a fixed directory on the microcomputer allowed by an USB-connection.

During field measurements, Reach RS+ is mounted on a tripod in an open area, Reach M+ is fixed on the drone or quad and connected by USB to the microcomputer and the Tallysman multi-GNSS antenna is fixed on the drone or quad.

Nonetheless, since GPS measurements are independent of radar measurements, a post-processing is required to match the two measurements. This post-processing consists in an

linear interpolation taking into account the accurate radar measurement time, the GPS time on the same clock and the GPS location for each GPS time.

Figure 4.12 – Reach M+ UAV Mapping Kit from EMLID

Chapter 5

Numerical experiments

5.1 Specific objective

The objective of the numerical experiments is the investigation of the main and most critical hypotheses considered in the used model described in Chapter 3, namely, the consideration of the soil as a lossless dielectric half-space. This hypothesis is based on a negligible effect of the electrical conductivity on the returned signal under high frequencies and absence of vertical variations of permittivity within the depth of sensitivity of the surface reflection.

The investigation consists in a visualization of the retrieved permittivity error when conductivity is neglected while it is different from zero.

5.2 Methodology

In order to test the validity of the zero-conductivity hypothesis to retrieve permittivity, numerical experiments were conducted. In particular, synthetic data with a series of conductive soil conditions were produced and subsequently inverted assuming zero-conductivity, thereby introducing a model error, and hence, a permittivity error. These analyses will therefore permit to define the range of conditions for which this hypothesis holds.

5.2.1 Synthetic data production

To produce the synthetic data considering a conductive soil, the height and relative permittivity were fixed on plausible values, such as $h = 2.5$ m and $\varepsilon_r = 5, 10, 15, 20$. Then, a vector ranging from 0 Sm^{-1} to 0.1 Sm^{-1} with a increment of 0.005 Sm^{-1} was chosen as the conductivity values of the synthetic data. The choice of this conductivity range was based on the typical ranges of conductivity found in soil formulated by [Samouëlian et al., 2005]. Hence, the synthetic data are therefore composed of 21 different values of conductivity, each with a height of 2.5m and a relative permittivity of 5, 10, 15 or 20.

Once these three parameters are well defined for the synthetic data, the calculation of

Green's functions is done for every combination of parameters.

This numerical analysis was performed on a single frequency range, namely $235 - 295$ MHz, which represents the frequency range used in this study with the 50 cm length dipole antenna.

5.2.2 Inversion and quantification of inversion errors

Assuming a lossless soil with $\sigma = 0$ Sm^{-1} for the inversion introduces therefore an error on the further estimated parameters when knowing that the synthetic data consider non-null conductivity values.

A method to evaluate the impacts of this created conductivity error on the parameters estimation, is the comparison between these estimated parameters and the synthetic parameters, previously fixed for the synthetic data Green's functions production. Hence, a parameter error can be calculated for every conductivity error and the sensibility can therefore be deduced.

Further, an inversion in the time domain can be achieved on the synthetic data, thanks to a LUT considering $\sigma = 0$ Sm^{-1} and an objective function can be calculated from this LUT and the synthetic data. The approximated parameters correspond to the parameters which minimize the objective function.

To properly assess the negligibility of the soil conductivity, it is good to proceed to the calculation of the error on the estimated parameters. In this paper, the error calculation is processed using the Root Mean Square Error (RMSE):

$$S_{\varepsilon_\mathrm{r}} = \left[\frac{\sum_{n=1}^{N} (\varepsilon_\mathrm{r} - \varepsilon_\mathrm{r}^*)^2}{N} \right]^{\frac{1}{2}} \tag{5.1}$$

$$S_h = \left[\frac{\sum_{n=1}^{N} (h - h^*)^2}{N} \right]^{\frac{1}{2}} \tag{5.2}$$

where ε_r is the actual relative permittivity, ε_r^* is the estimated relative permittivity, h is the actual height, h^* is the estimated height and N is the number of estimated parameters, namely in this case, 21.

5.3 Results and discussion

5.3.1 Synthetic data production

In order to have a first sight on the synthetic data, the amplitude of the 21 synthetic Green's functions in the frequency domain were plotted for all the frequency range considered in these numerical experiments, namely, 235−295 MHz. These plots are presented in Figure 5.1.

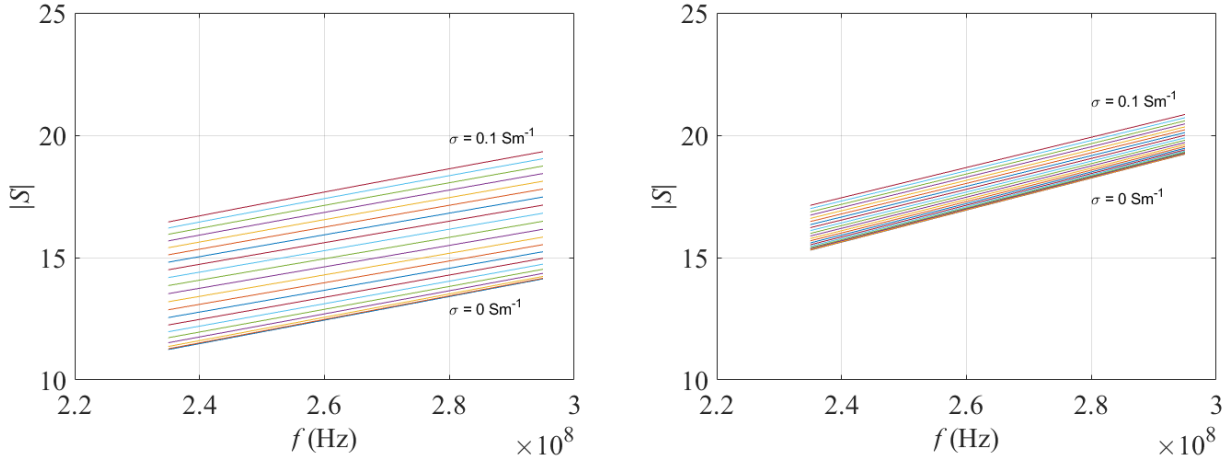

(a) $\varepsilon_r = 5$ (b) $\varepsilon_r = 10$

(c) $\varepsilon_r = 15$ (d) $\varepsilon_r = 20$

Figure 5.1 – Amplitude of the synthetic Green's functions in the frequency domain for the 4 different ε_r. Each plot contains the 21 Green's functions, considering the different electrical conductivity.

On these subfigures, the first blue line represents the synthetic Green's function for $\sigma = 0$ Sm^{-1} and the upper red line is the Green's function of the 21$^{\text{th}}$ value of conductivity, namely, $\sigma = 0.1$ Sm^{-1}. High disparities appear when comparing the plots of the different permittivities, with smaller the considered relative permittivity is, higher is the sensitivity on the amplitude. Indeed, the curves in Figure 5.1a considering $\varepsilon_r = 5$ are spaced apart, while the curves of Figure 5.1d, considering $\varepsilon_r = 20$ are barely distinguishable.

This first sight on the synthetic data already gives indications on the future trend of the hole numerical analysis. Indeed, it is quite logical that high disparities in the synthetic Green's functions bring high discrepancies in the estimated parameters. It is thus expected that all numerical experiments on the synthetic data considering $\varepsilon_r = 5$ will show higher error than data considering a higher ε_r.

5.3.2 Error production and data inversion

Once the synthetic data have been visualized, an inversion can be processed for the estimation of the height and relative permittivity from the LUT considering $\sigma = 0$ Sm^{-1}. From these estimated parameters, the error can be calculated by the simple difference between the actual parameters of the synthetic data and the retrieved parameters from the inversion process. Then, since the considered model conductivity is $\sigma = 0$ Sm^{-1}, the conductivity error in these experiments equals the fixed conductivity vector for the production of the synthetic data. Figures 5.2 and 5.3 show, respectively, the error on the height and relative permittivity for the considered relative permittivity accounting for different conductivity errors.

Some disparities on these curves can be seen already on these two figures and a common trend emerges. Indeed, the error on height, such as on relative permittivity, increases with an increasing conductivity error. Moreover, the sensitivity of the electrical conductivity on these two parameters decreases when permittivity increases. The trend expected in the last subsection is therefore confirmed.

The calculation of the Root Mean Square Error was performed using Equations (5.1) and (5.2) for the different numerical experiments. The results are summarized in Table 5.1.

Table 5.1 – Root Mean Square Error on the estimated relative dielectric permittivity ε_r and estimated height h for the different numerical experiments.

	S_h	S_{ε_r}
$\varepsilon_r = 5$	0,0227	3,3881
$\varepsilon_r = 10$	0,0103	1,9456
$\varepsilon_r = 15$	0,006	1,4288
$\varepsilon_r = 20$	0,004	1,1414

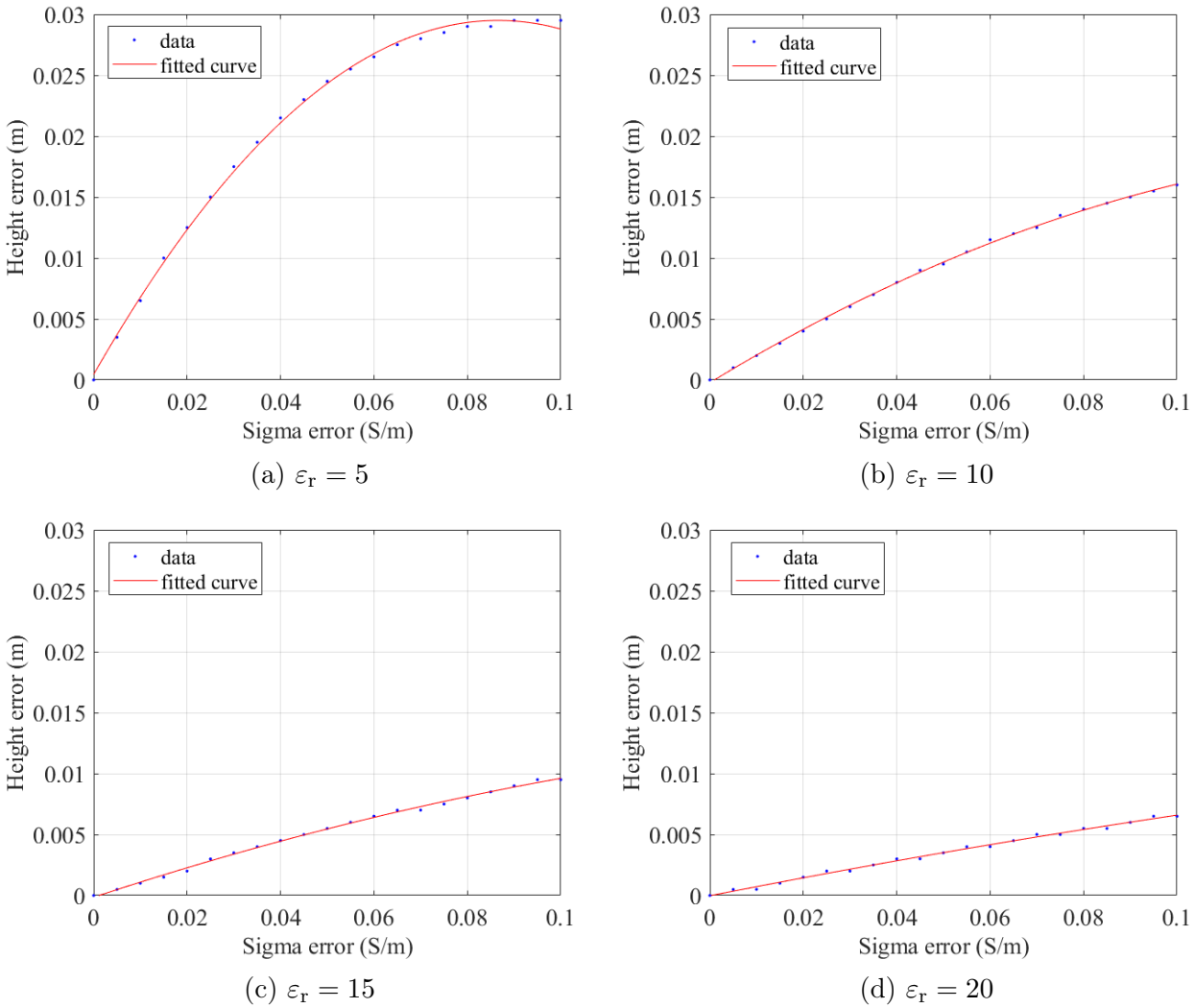

(a) $\varepsilon_r = 5$ (b) $\varepsilon_r = 10$

(c) $\varepsilon_r = 15$ (d) $\varepsilon_r = 20$

Figure 5.2 – Error on the estimated height h. Each of the 21 points is related to one of the 21 generated Green's functions.

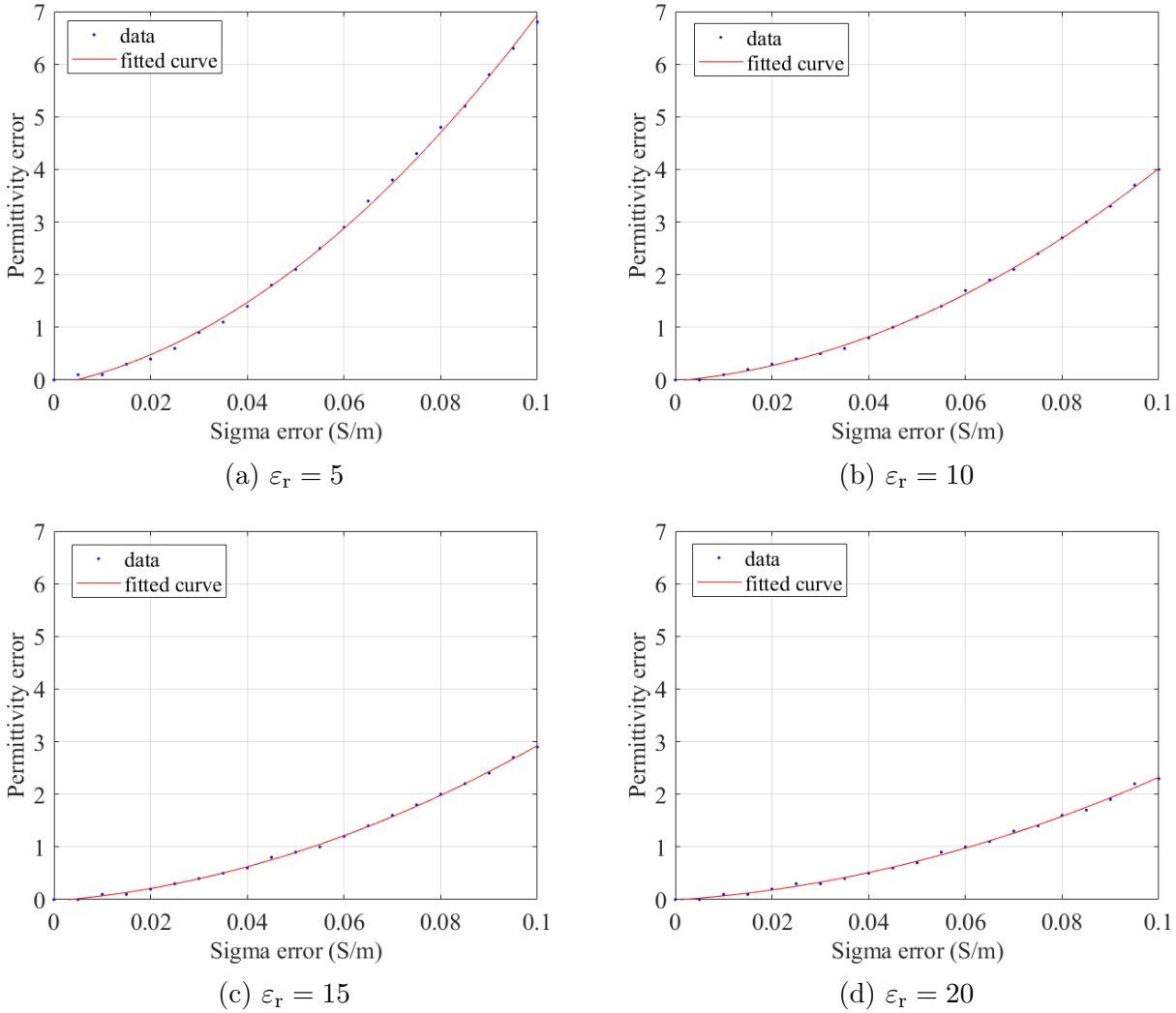

(a) $\varepsilon_r = 5$ (b) $\varepsilon_r = 10$

(c) $\varepsilon_r = 15$ (d) $\varepsilon_r = 20$

Figure 5.3 – Error on the estimated permittivity ε_r. Each of the 21 points is related to one of the 21 generated green's functions.

The error on permittivity can be translated in soil water content (θ) error thanks to Topp's equation (Equation (2.9)). Figure 5.4 shows the soil water content error for the 4 different permittivities based on Equation (5.3):

$$\theta_{\text{error}} = \theta_{\text{estimated}} - \theta_{\text{fixed}} \tag{5.3}$$

where $\theta_{\text{estimated}}$ is the soil water content, in $\text{cm}^3\text{cm}^{-3}$, corresponding to the estimated relative permittivity through inversion and θ_{fixed} is the soil water content, in $\text{cm}^3\text{cm}^{-3}$, corresponding to the relative permittivity fixed during the synthetic data production.

In Figure 5.4, it is crystal clear that higher the relative permittivity is, lower the error on soil water content will be. This behavior is due to the larger contribution of ε_r to the amplitude of the surface reflection with respect to the effect of σ.

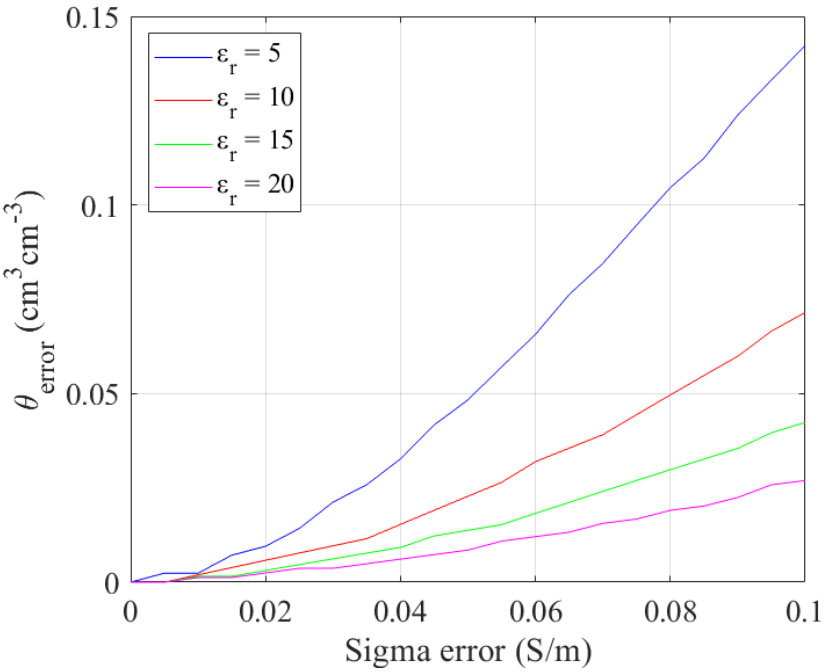

Figure 5.4 – Soil water content error due to lossless soil consideration for the 4 different permittivities.

This behavior is in good concordance with the results of Slob et al. [2010], where a numerical analysis of full-waveform inversion focused on the surface reflection was performed and led to the assessment of the error in electric permittivity values as a function of permittivity and conductivity values. Furthermore, in the study of Lambot et al. [2006b], it was found that forcing the conductivity to be zero did not deteriorate the permittivity retrieval when $\sigma < \sim 0.01$ S/m^{-1}, but for higher value of conductivity, the estimated permittivity were less accurate and even led to unrealistic values for $\sigma > \sim 0.1$ S/m^{-1}.

Finally, to evaluate the discrepancies when considering different sub-ranges of frequency, a sub-sample was made on the fixed frequency vectors. The frequency vector was divided into 3 sub-vector, namely, 235 - 255 MHz, 255 - 275 MHz and 275 - 295 MHz. Then, the permittivity error was calculated with the same method as in Figure 5.3 and the three curves were plotted in Figure 5.5. Another frequency band was analyzed and added on the same plot, namely, 300 - 850 MHz. This band corresponds to the frequencies used with the second antenna for field measurements using the radar mounted on the quad, i.e., the logarithmic periodic antenna.

In this figure, higher is the frequency band, higher is the accuracy. Hence, the last frequency band, namely, 300 - 850 MHz shows much lower relative dielectric permittivity errors than others frequency bands. Using this frequency band, the RMSE for the height and relative permittivity are, respectively, 0.0019 and 0.3370 with $\varepsilon_r = 10$ fixed. Regarding Table 5.1, the result is significantly lower than the RMSE calculated for the 235 - 295 MHz band. This lower error can be explained by the fact than the imaginary part of the propagation wave, containing the effect of the electric conductivity is divided by the angular frequency [Lambot et al., 2006b].

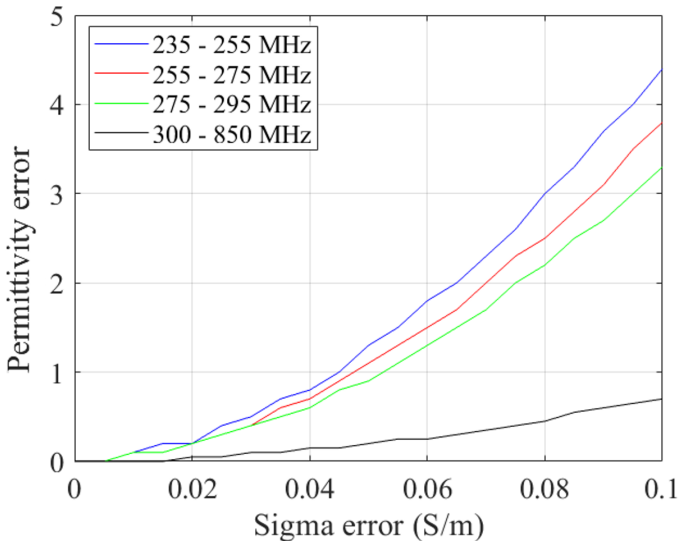

Figure 5.5 – Error on the estimated permittivity ε_r for three frequency sub-vector, considering the different electrical conductivity errors.

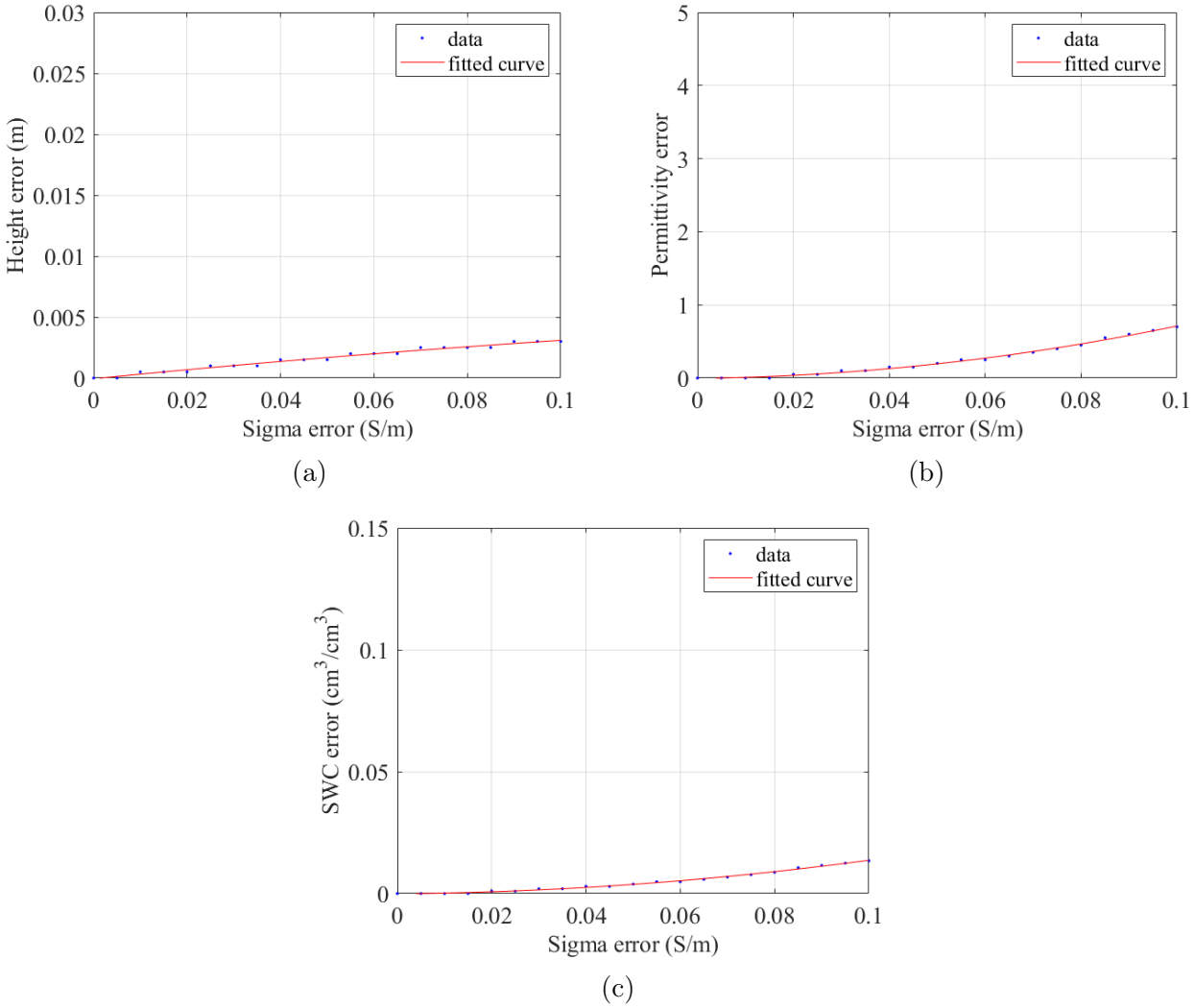

Figure 5.6 – Different numerical experiments results when considering 300 - 850 MHz frequency range. a) represents height error b) represents relative permittivity error and c) represents the resulting error on soil moisture.

Figure 5.6 represents the results of the last numerical experiment, i.e., the numerical experiment considering the 300 - 850 MHz frequency band. Here, note that the scales were chosen to allow the comparison with the previous figures. It appears that all these results are much more accurate than the previous, with an error on height and permittivity less than 0.005 (m) and 1, respectively. These results were expected since the frequency range used for this experiment, namely, 300 - 850 MHz is significantly higher than for the previous experiments.

5.4 Conclusion

Thanks to these different results, it is clear that the use of the 300 - 850 MHz frequency band is recommended. Indeed, the error on soil water content is much lower for this frequency band as the maximum error is 0.0134 cm^3cm^{-3} for a conductivity error of 0.1 S/m^{-1}. Note that most soils are below that value, except soils with a relative high clay content in wet conditions. Moreover, the Root Mean Square Error value on the permittivity for this frequency range is 0.3370, which represents less than 1% humidity and, hence, can be considered as acceptable in agricultural applications.

Nevertheless, this error can be minimised by fixing an expected electrical conductivity value for the sampled soil. This can be done by consulting the literature, such as the paper of [Samouëlian et al., 2005] or by some field measurements of conductivity, e.g., using electromagnetic induction or low frequency range GPR.

The numerical experiments performed in this chapter showed some of the physical limitations of the assumptions on the conductivity used for the surface dielectric permittivity estimation. Indeed, knowing that wet clay soil can show high electrical conductivity values [Grisso et al., 2005], a particularly attention have to be made to the conductivity-related error, especially if the dipole antenna is used, due to its limited frequency bandwidth.

Chapter 6

Soil moisture mapping using GPR

The aim of this chapter is to show the results of the different acquisition campaigns. First, a step-by-step explanation of the data processing will be presented for a single dataset.

For now, two different antennas were tested and two methodologies were used (drone and all terrain vehicle).

By the end of this chapter, an explanation attempt of the different discrepancies between the acquisition will be made.

6.1 Signal processing

6.1.1 Radar data visualisation and processing

In this section, a description of the measured signal, their different processing and their results will be described. This will lead to a better understanding of the logic behind the signal processing.

For that purpose, the 24/02/2021 dataset is selected as example. In Figure 6.1, the radar altitude is plotted for all measurements. In this figure, the altitude peak was made on purpose and allows the free space conditions radar measurements for the further signal correction. The index vector presented in horizontal axis indicates the measured points.

Figure 6.2 shows the hand-made subselection of measurement points. The exclusion of such end-points is justified by the difference of the measurement angle when a directional change is done with UAV. Indeed, this change in the incident angle of measurement is not part of the model and is not measured to match with the calibration. The remaining points will be further used for the inversion.

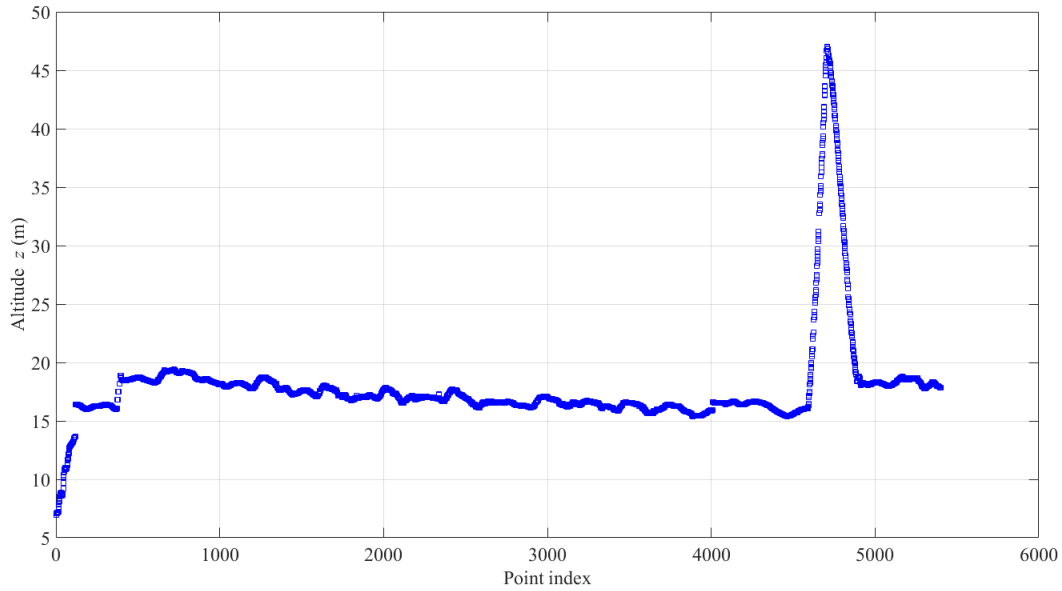

Figure 6.1 – Measurement altitude (above ground level) of the 24/02/2021 dataset as provided by the dGPS.

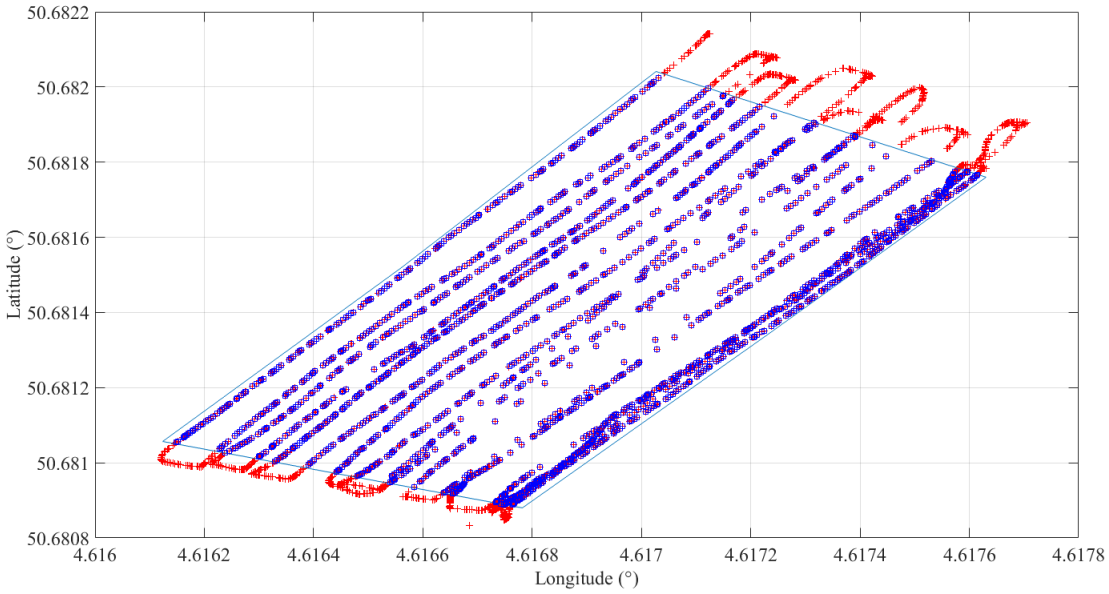

Figure 6.2 – Measurements map of the 24/02/2021 dataset. The blue polygon represents the selection of points that will be further considered for the inversion (WGS84).

Figure 6.3 shows two graphs representing H_i, the characteristic reflection coefficient of the antenna. The blue curve represents H_i determined by a free-space measurement (considered here by a measurement at high altitude, as visible in Figure 6.1), while the red curve is H_i determined through antenna calibration (water body). The upper subfigure represents the amplitude and the lower represents the phase. During the processing of the data, it is possible to correct the H_i used, namely, the H_i from the calibration process, with the H_i measured in the free space condition during the high altitude flight. Ideally, both H_i measured ans H_i calibrated are matching perfectly.

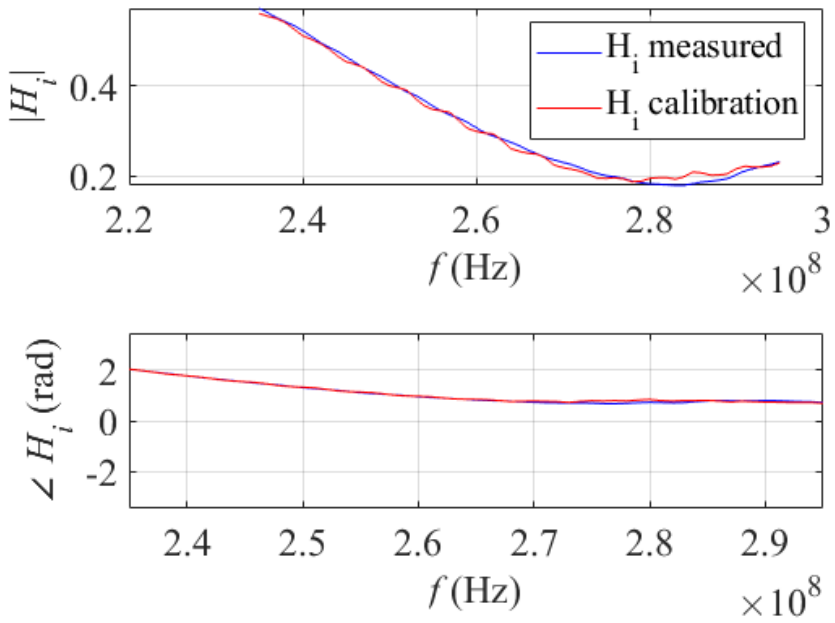

Figure 6.3 – Global reflection coefficient H_i of the antenna derived from the water body calibration (red curve) and high-altitude measurement (blue curve).

Figure 6.4 presents the measured signal in the time domain for the 24/02/2021 dataset. Here, the reflection at the soil surface is clearly visible (yellow-blue oscillations), with reflections ranging from 7 to 30 ns. This propagation time is the time for the wave to make the forth and back and, hence, if considering the light speed, the distance between soil and radar can be deduced for every measurement. In this case, it is visible that the height of the UAV is between 1,5 m and 4,5 m. This retrieved height information will be part of the inversion from the look-up table (LUT).

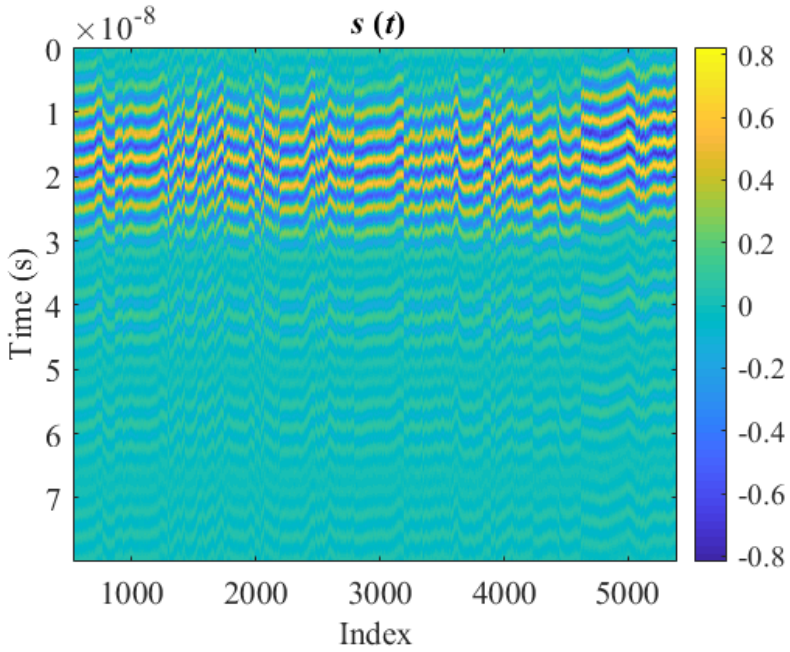

Figure 6.4 – Measured signal in the time domain for the 24/02/2021 dataset acquired by UAV-GPR over the field of the Ferme de Lauzelle.

6.1.2 Inversion results and discussion

From the previously presented data and from a pre-processed LUT, an inversion can be performed. In that regard, an objective function is calculated for every measurement. This objective function contains the error, calculated in the least-square sense, between the signal and the Green's function for every parameter combinations. The soil parameters correspond to the LUT parameters for which the objective function presents its minimal value. In order to filter out the worse model fits and therefore keep only successful inversions, a maximal objective function value is defined. In this thesis, this value is arbitrary fixed to :

$$\phi_{\max} = \overline{\phi} + 1,5\ \sigma_\phi \tag{6.1}$$

where $\overline{\phi}$ is the mean value of the minima of the objective functions corresponding to all radar measurements and σ_ϕ is the corresponding standard deviation. Since higher is the value of the objective function, lower is the quality of the fit, this sub-selection based on the standard deviation leads to a selection of the best fits. Figure 6.5 illustrates this fit enhancement with lower ϕ values and the deterioration effect with higher ϕ values.

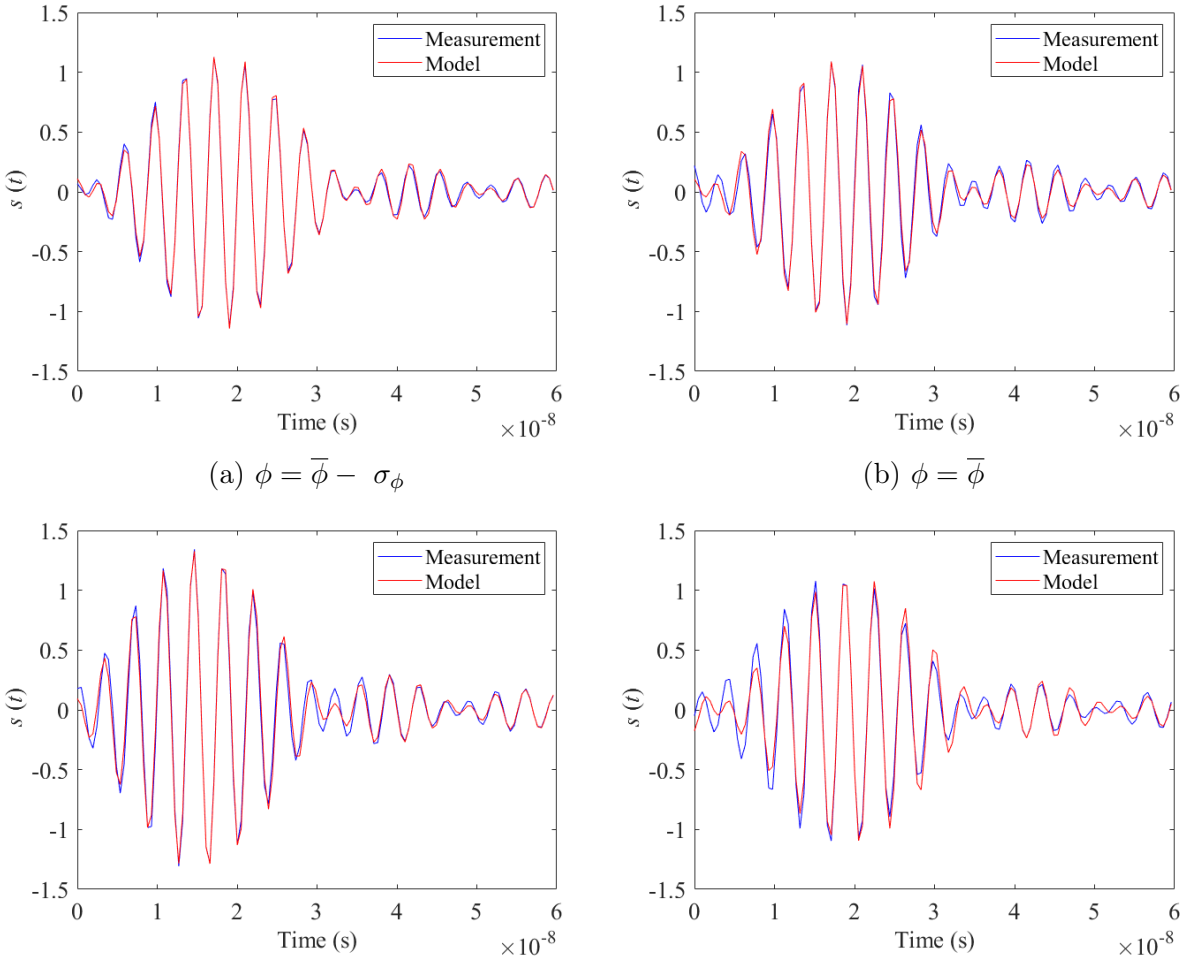

(a) $\phi = \overline{\phi} - \ \sigma_\phi$ (b) $\phi = \overline{\phi}$

(c) $\phi = \overline{\phi} + \ \sigma_\phi$ (d) $\phi = \overline{\phi} + 2\ \sigma_\phi$

Figure 6.5 – Fits of the measured and modelled signals, corresponding to 4 different minimized values of objective function ϕ.

Beside this illustration of the discrepancies in the minima of the objective functions corresponding to all radar measurements dataset objective function, the histogram of all the minimised objective function values is illustrated in Figure 6.6. Here, according to Equation (6.1), $\phi_{\max} = 0,7055$. This means that all the sampled points whose the objective function minimum value is larger than 0,7055 will not be taken into account, these filtered data represent 16.65% of the total data. In that way, outliers are removed as well.

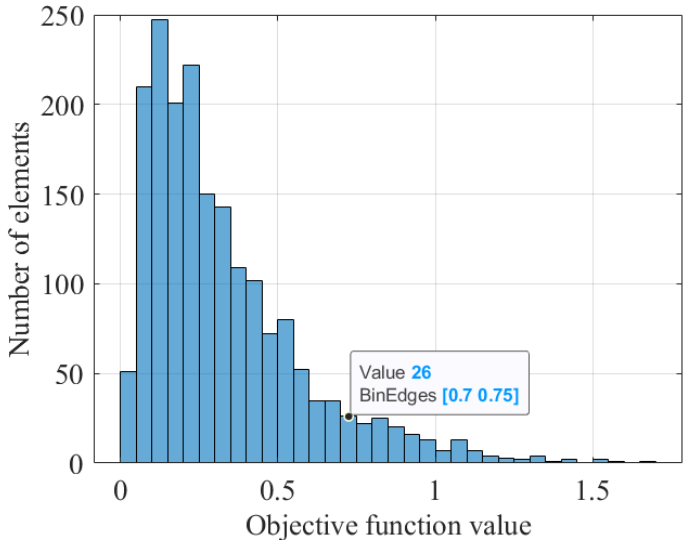

Figure 6.6 – Histogram of all the calculated minimum objective function values for the 24/02/2021 dataset.

Figure 6.7 shows the retrieved height of measurement from the signal through inversion. Figure 6.7a shows the retrieved height from all the measured points, while Figure 6.7b shows the retrieved height for the points whose the minimum objective function value is $< \phi_{\max}$. The statistic-based filtering leads therefore to smoother values, as subject to less estimation errors.

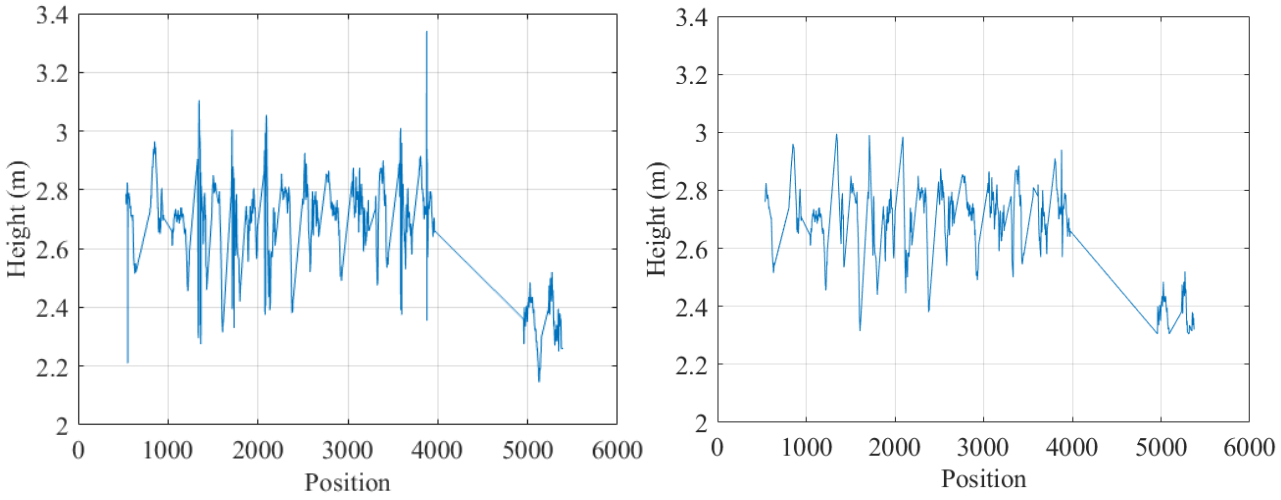

(a) $\phi_{\max} = \infty$ (b) $\phi_{\max} = \overline{\phi} + 1,5\ \sigma_{\phi}$

Figure 6.7 – Comparison between retrieved height value (a) without maximum objective function value: $\phi_{\max} = \infty$ and (b) with maximum objective function value: $\phi_{\max} = \overline{\phi} + 1,5\ \sigma_{\phi}$.

Figure 6.8 shows the retrieved relative permittivity of the sampled soil from the signal through inversion. Figure 6.8a shows the retrieved relative permittivity from all the measured points, while Figure 6.8b shows the retrieved relative permittivity for the points whose minimum objective function value is $< \phi_{\max}$. In this second case, using this filter significantly improves the results as outliers are removed and estimation uncertainty is lower. Nevertheless, the retrieved relative permittivity appears to be too high for such soil and moisture conditions. These over-estimations are attributed to an antenna calibration issue. They may also originate from shallow layering leading to constructive interferences while an homogeneous half-space medium is assumed (see [Lambot et al., 2006b]).

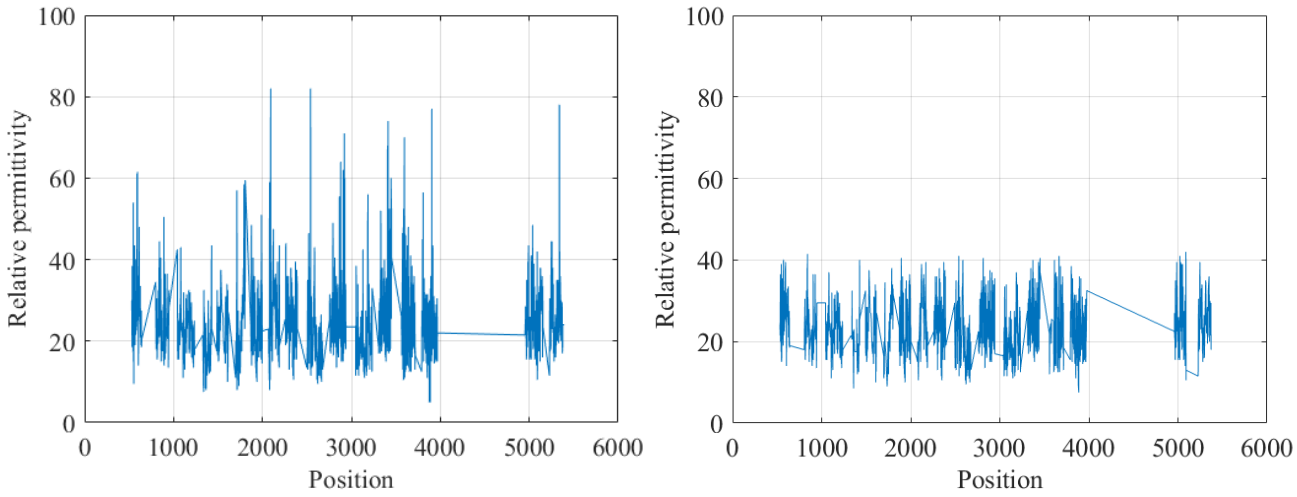

(a) $\phi_{\max} = \infty$ (b) $\phi_{\max} = \overline{\phi} + 1,5\ \sigma_{\phi}$

Figure 6.8 – Comparison between retrieved permittity value (a) without maximum objective function value: $\phi_{\max} = \infty$ and (b) with maximum objective function : $\phi_{\max} = \overline{\phi} + 1,5\ \sigma_{\phi}$.

Once the estimation of the soil relative permittivity is retrieved, the results can be mapped to visualise the estimated soil moisture at the field scale. Indeed, Topp's equation (see Equation (2.9)) empirically links the permittivity and the soil moisture value. From the retrieved humidity values, a kriging was used to produced an interpolated map (Figure 6.9).

Figure 6.10 shows the semivariogram of the dataset for the kriging process. A nugget exponential model was fitted over the variogram estimates. A nugget effect is visible on the figure, indicating measurements noise and a short scale variability that is random and unpredictable (nugget = 13.27, partial sill = 28.12, range = 3.1 m). Note that the spatial correlation length is very small since the variance stabilizes with a distance of 3.1 m, despite a high maximum variance.

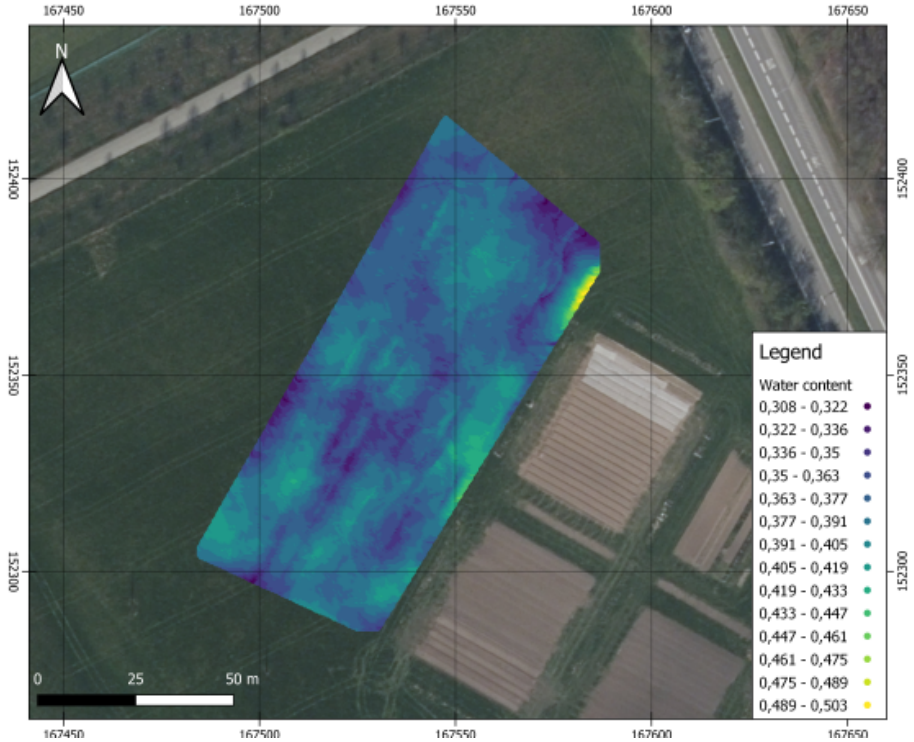

Figure 6.9 – Soil moisture mapping for the 24/02/2021 dataset using UAV-GPR setup.

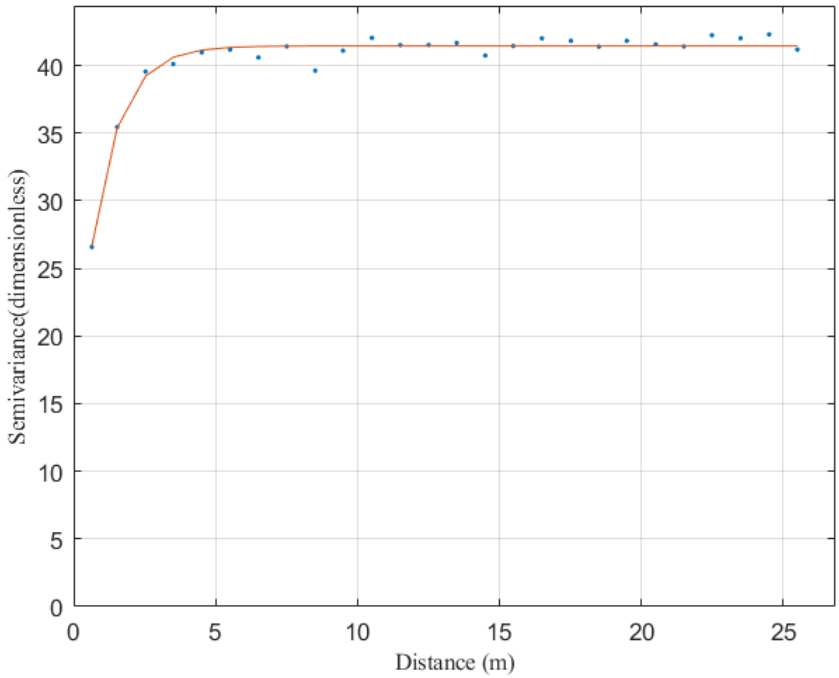

Figure 6.10 – Semivariogram of the 24/02/2021 permittivity data for the kriging in Figure 6.9.

6.2 Soil moisture mapping from the different datasets

To ensure the good quality of measurements of the different setups, several measurement campaigns were carried out. Figures 6.11 and 6.12 show the water content results of the different

campaigns. In the three first subfigures, namely, Figures 6.11a, 6.11b and 6.11c, overestimation of soil moisture values are visible. Indeed, the estimated soil relative permittivity is close to the relative permittivity of pure water, which is impossible for a soil. The setup used for these three maps was the dipole antenna mounted on the all-terrain vehicle. These discrepancies with the reality may be explained by the antenna-quad interactions and radar calibration, as explained above for the drone dataset. Indeed, the conductive materials of the all-terrain vehicle can interfere with the electromagnetic waves and highly impact the results if not taken into account. These conductive materials lead therefore to an increase of wave reflections, which are not taken into account during the data processing since the antenna was not calibrated when mounted on the all-terrain vehicle.

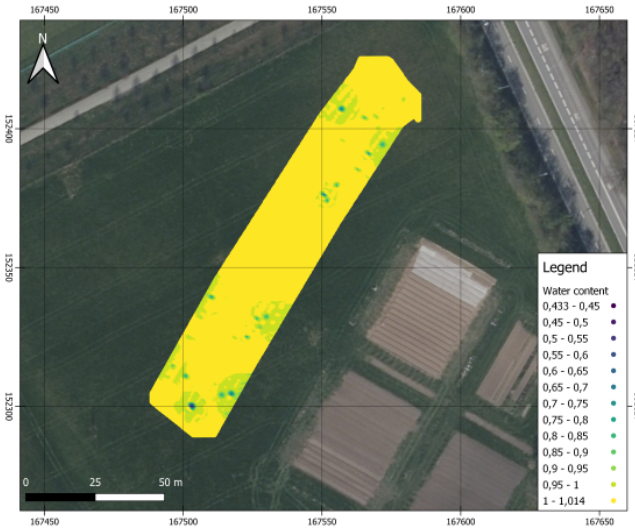

(a) 24/03/2021 - a

(b) 24/03/2021 - b

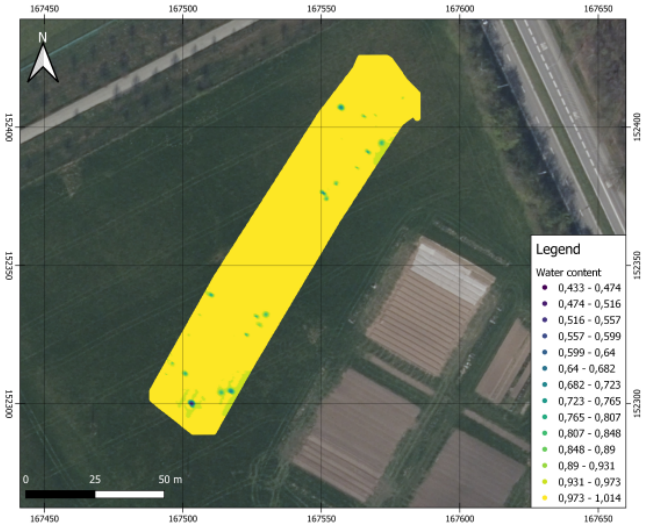

(c) 24/03/2021 - c

Figure 6.11 – Soil moisture content mapping of the 24/03/2021 dataset using 4x4 vehicle-dipole antenna.

Nevertheless, as we focus on the surface reflection, the backsctattered waves from the measured field would logically arrive earlier than the reflected waves from the quad and, thereby, not impact the inverted results. A hypothesis is that the narrow bandwidth of the dipole

antenna does not permit to fully separate the reflections in time. Considering this, the quad can still interfere, even if the propagation time is larger compared to the one of the surface reflection.

The three next subfigures, namely, 6.12a, 6.12b and 6.12c were taken with the logarithmic periodic antenna mounted on the all-terrain vehicle. Qualitatively, these three last maps show very consistent results, with values in the expected range of soil moisture. Unfortunately, this antenna being too heavy to be set up on the UAV, a solution have to be found to allow a good quality measurements with the dipole antenna.

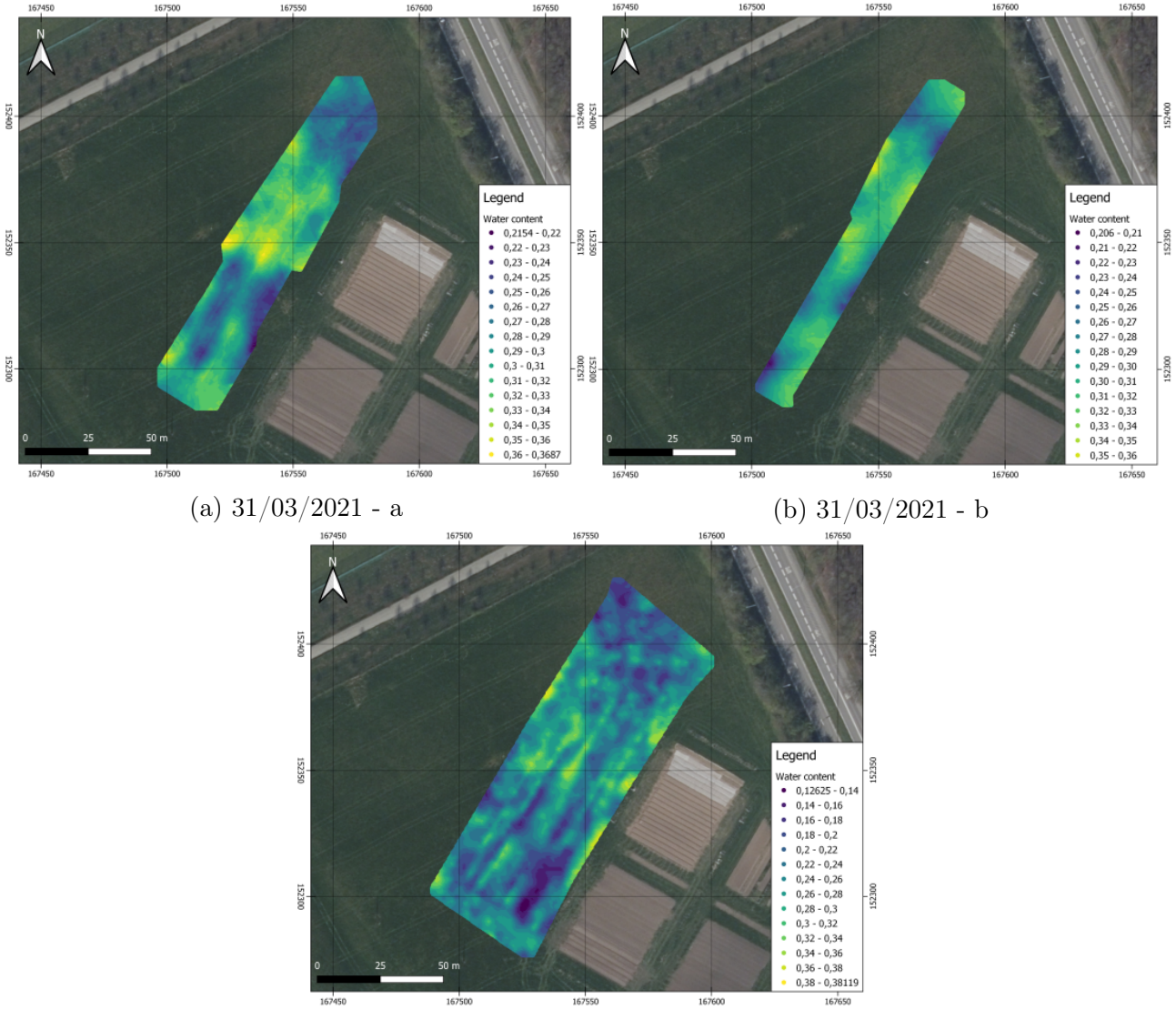

(a) 31/03/2021 - a

(b) 31/03/2021 - b

(c) 06/04/2021

Figure 6.12 – Soil moisture content mapping of the 31/03/2021 and 06/04/2021 datasets using 4x4 vehicle-logarithmic periodic antenna.

The soil moisture results obtained through these different measurements using the quad-log GPR show a common behavior. Indeed, higher soil moisture values are generally retrieved in the upper middle of the field. This heterogeneous moisture distribution is attributed to the

topography of the field, which presents a slope in its upper part (North-East), directing the water at the bottom of that slope.

6.3 Conclusion

In this chapter, the different results of the data acquisition campaigns were showed and qualitatively assessed. Further, an attempt was made to explain the discrepancies between the results of the different setups and concludes that the poor quality results of the dipole antenna is due to its poorly directive radiation pattern which leads to wave reflections from interactions with the all-terrain vehicle conductive materials. Here, it is important to note that the directivity issue of the antenna is not an issue since it is part of the model, but it requires an adapted calibration.

It is possible to prove that these discrepancies are due to the reflections by the quad conductive materials thanks to a change in the antenna orientation in relation to the vehicle. If the antenna would be oriented such as its donut-shapped radiation pattern has its new plane perpendicular to the vehicle axis, the conductive materials of the vehicle would disappear from the radiation area and, hence, no more interfere with the signal.

A way to solve this issue is to properly calibrate the dipole antenna mounted on the quad or UAV. In this manner, the reflection due to the vehicle will be properly taken into account. However, such a calibration is not straightforward given the significant size of the calibration reflector that would be needed (at least 6 m x 6m).

Finally, the good quality results of the logarithmic antenna with the all-terrain vehicle are very promising and its utilization for comparative purposes could provide good information for the validation step.

The next step is therefore the validation of drone-borne soil moisture mapping. This last step can be achieved by several measurements within a same time windows, with several tools. Of course, to allow good quality results, a new calibration is needed, as highlighted in this chapter.

Chapter 7

Validation

7.1 Specific objective

The aims of this section is the assessment of the drone-borne GPR results quality for soil moisture mapping at the field scale in order to validate the mapping method. In that regard, a measurement campaign, using different measurement tools, was carried out. These different tools will allow the comparison between their relative moisture values, several tools being considered as reference methods for soil moisture determination. The different used tools are the logarithmic antenna radar mounted on the all-terrain vehicle, TDR sampling, gravimetric sampling and the drone-borne GPR.

In this chapter, a discussion about the differences observed between the four characterization methods will be performed.

7.2 Materials and methods

In the aim of the drone-borne moisture mapping validation, a measurements campaign was carried out on April 30, 2021. This measurement campaign was performed with different tools, namely, GPR (UAV-dipole and all-terrain-logarithmic antenna setups), gravimetric and TDR.

The day before, 15 flags have been placed, each referring to a specific location previously determined by a dGPS (Leica 1200), as showed in Figure 7.1. The flags locations were chosen in order to cover the heterogeneity of the field. For this, the general behavior of water distribution was used, based on the previous maps. Further, the flags served for the indication of the locations to be measured by the different tools.

7.2.1 TDR and gravimetric sampling

For more technical and theoretical information about these two methods, the reader is referred to Sections 2.2.1 and 2.2.2.2 in the state of the art chapter.

Figure 7.1 – Flags locations among the study field.

The used TDR device is a Teros-12 from Meter Environment (California, USA). It supplies a 70-MHz oscillating wave to the sensor needles, which charge according to the dielectric constant of the material, namely, the sampled soil. The SWC is then retrieved by a calibration equation specific to a mineral substrate. The circuitry of this sensor was optimized to deliver a volume of influence of one liter through the 5.5cm long rods [Meter Environment, 2021].

The TDR measurements were taken in two different ways. First, three surface measurements were made in a triangle shape with an identical distance from the flag (about 15cm-20cm). This will allow the assessment of the micro-variability of the soil-moisture around the determined locations. A scheme of these measurements is visible in the left side of Figure 7.2.

In a second time, two undisturbed soil samples were taken at 5cm and 10cm depth. These two samples were subsequently weighted to determine their relative volumetric moisture through the reference gravimetric method. The undisturbed soil samples were taken by means of 100cm^3 Kopecky's rings, referred to as K1 and K2, and were weighed after 7 days of drying in a dedicated room. A fourth TDR measurement was taken, at the common boundary of the two undisturbed soil samples. A scheme of these last measurements is sketched on the right side of Figure 7.2.

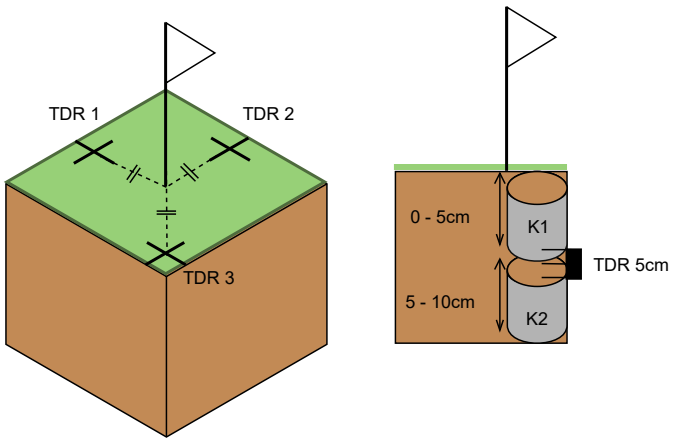

Figure 7.2 – Gravimetric and TDR based soil sampling methodology.

7.2.2 GPR sampling

During this campaign, 3 maps were taken by the logarithmic-periodic antenna setup mounted on the all-terrain vehicle. Then, being confronted to a technical computer-related issue and limited by the two batteries from the drone, only a single map was taken by the drone-borne GPR. Finally, for these two measurement methods, measurements were taken at precise location through a stop for the all-terrain vehicle or a hovering flight for the drone, this last being illustrated in Figure 7.3.

Figure 7.3 – Hovering flight above a determined location during the measurement campaign.

7.3 TDR and gravimetric results

The raw results, as well as the average and variance values of the three TDR surface measurement datasets are presented in Table 7.1. To better visualize the moisture micro-variability in the field, the data of Table 7.1 are plotted in Figure 7.4. In this figure, important discrepancies appear, as visible for points 7, 12 and 14. Nevertheless, very close results are also

visible, as seen for points 2, 3, 9 and 10. This variable behavior may be due to the light rain occurred the previous day and inherent microvariability within agricultural fields.

Table 7.1 – Soil water content, average and variance of the TDR surface measurements (cm^3/cm^3).

	(cm^3/cm^3)				
Points	TDR 1	TDR 2	TDR 3	TDR average	Variance
1	0.204	0.277	0.236	0.239	0.030
2	0.275	0.272	0.28	0.276	0.003
3	0.306	0.319	0.325	0.317	0.008
4	0.315	0.287	0.352	0.318	0.027
5	0.26	0.229	0.288	0.259	0.024
6	0.283	0.321	0.261	0.288	0.025
7	0.29	0.226	0.284	0.267	0.029
8	0.28	0.312	0.278	0.290	0.016
9	0.278	0.271	0.258	0.269	0.008
10	0.225	0.252	0.242	0.240	0.011
11	0.277	0.31	0.343	0.310	0.027
12	0.28	0.192	0.274	0.249	0.040
13	0.24	0.317	0.283	0.280	0.032
14	0.303	0.174	0.249	0.242	0.053
15	0.189	0.194	0.15	0.178	0.020

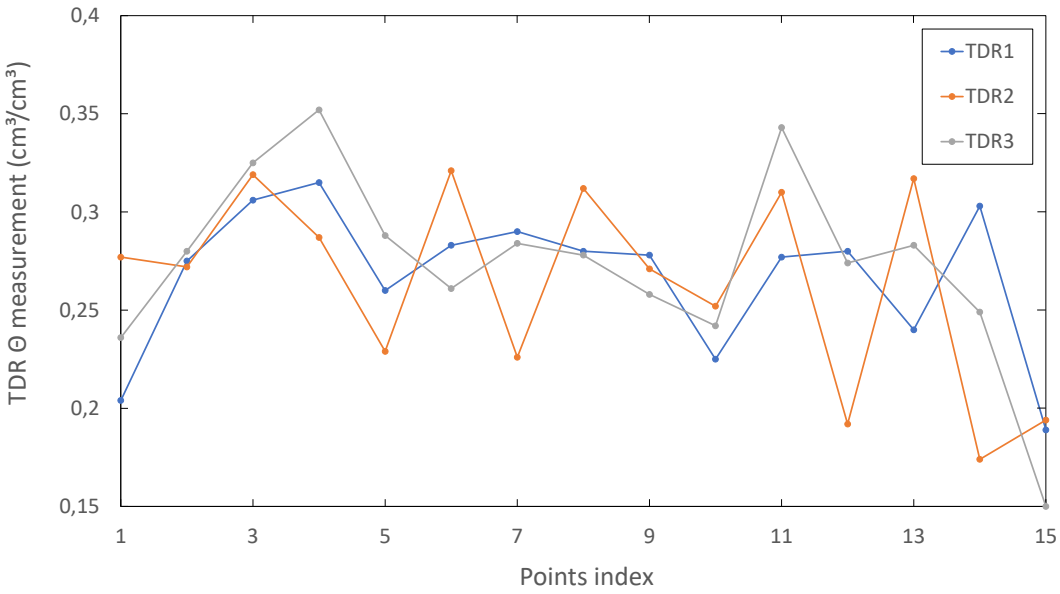

Figure 7.4 – Moisture results through the surface TDR measurements at the 15 strategic locations.

In Table 1 of Appendix A.1, the results of the gravimetric and the 5cm depth TDR measurements methods are shown. The correlation between the two measurement method is presented in Figure 7.5. Note that the results of point 14 is not considered, since a defective

transport bag was used for the 0-5cm gravimetric sample. The gravimetric values presented in the figure are the average values of the 0-5cm and 5-10cm samples since both depths are contained in the volume of influence of the 5cm-depth TDR.

When regarding the differences between these gravimetric and TDR values, an average error of 0.026 (cm^3/cm^3) can be observed, which is quite acceptable for the consideration of these both reference methods for the ground-truth moisture values measurements.

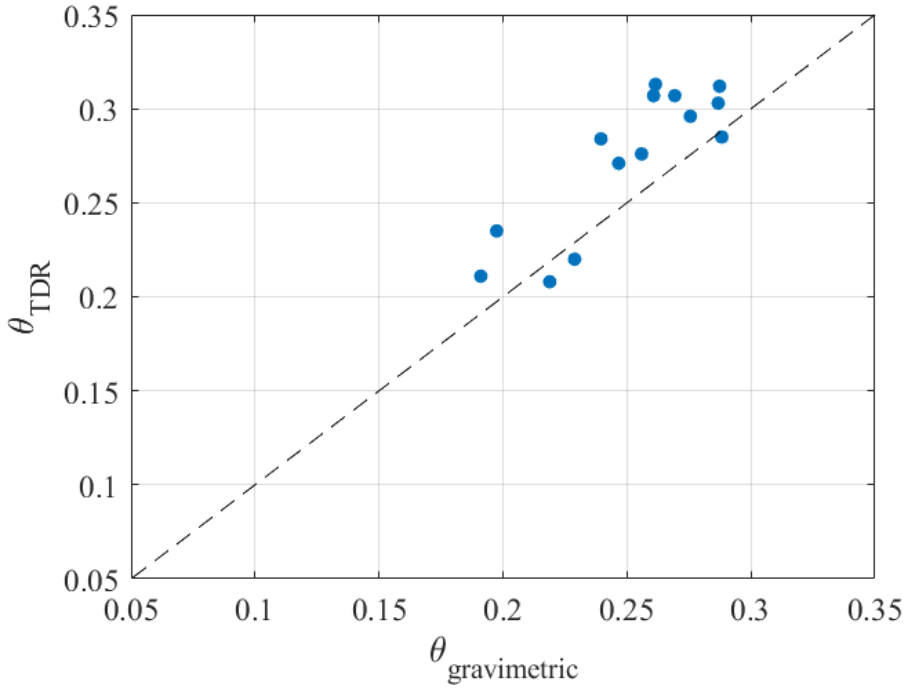

Figure 7.5 – Correlation plot between the TDR and the gravimetric (0-10cm) measured SWC

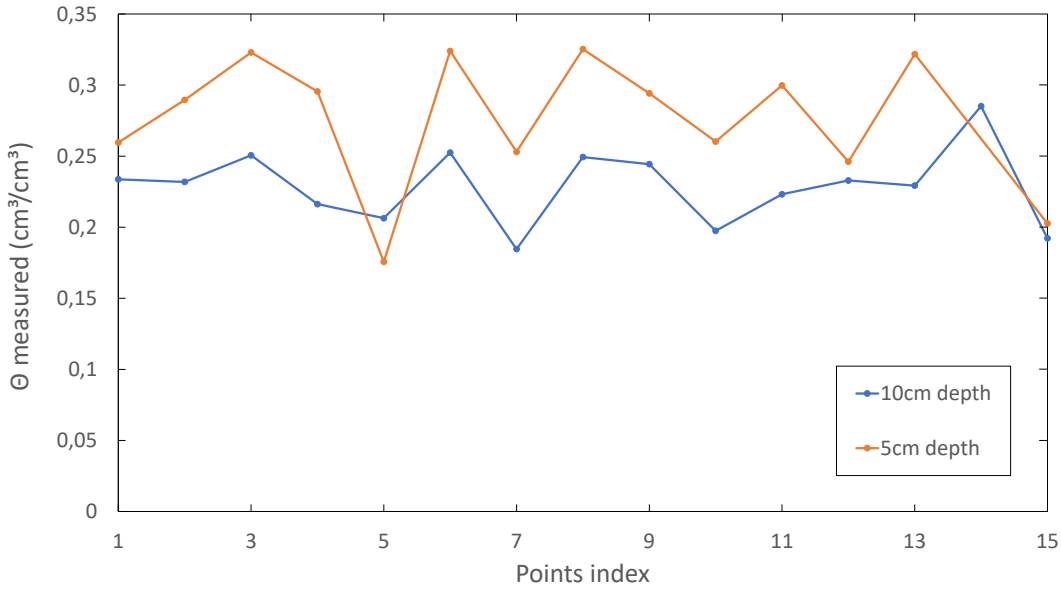

Figure 7.6 – Gravimetric results at 5cm and 10cm depth at the 15 strategic locations.

Figure 7.6 shows the plot of the soil water content results in the 5cm and 10cm depth

sampled soil layers. The general behavior of the water distribution through the near-surface soil profile is visible and indicates that a higher moisture is observed in the first 5cm layer than in the 5-10cm layer. This moisture discrepancies may be attributed to the rain which occurred the day before.

7.4 GPR results

7.4.1 Quad-logarithmic periodic antenna results

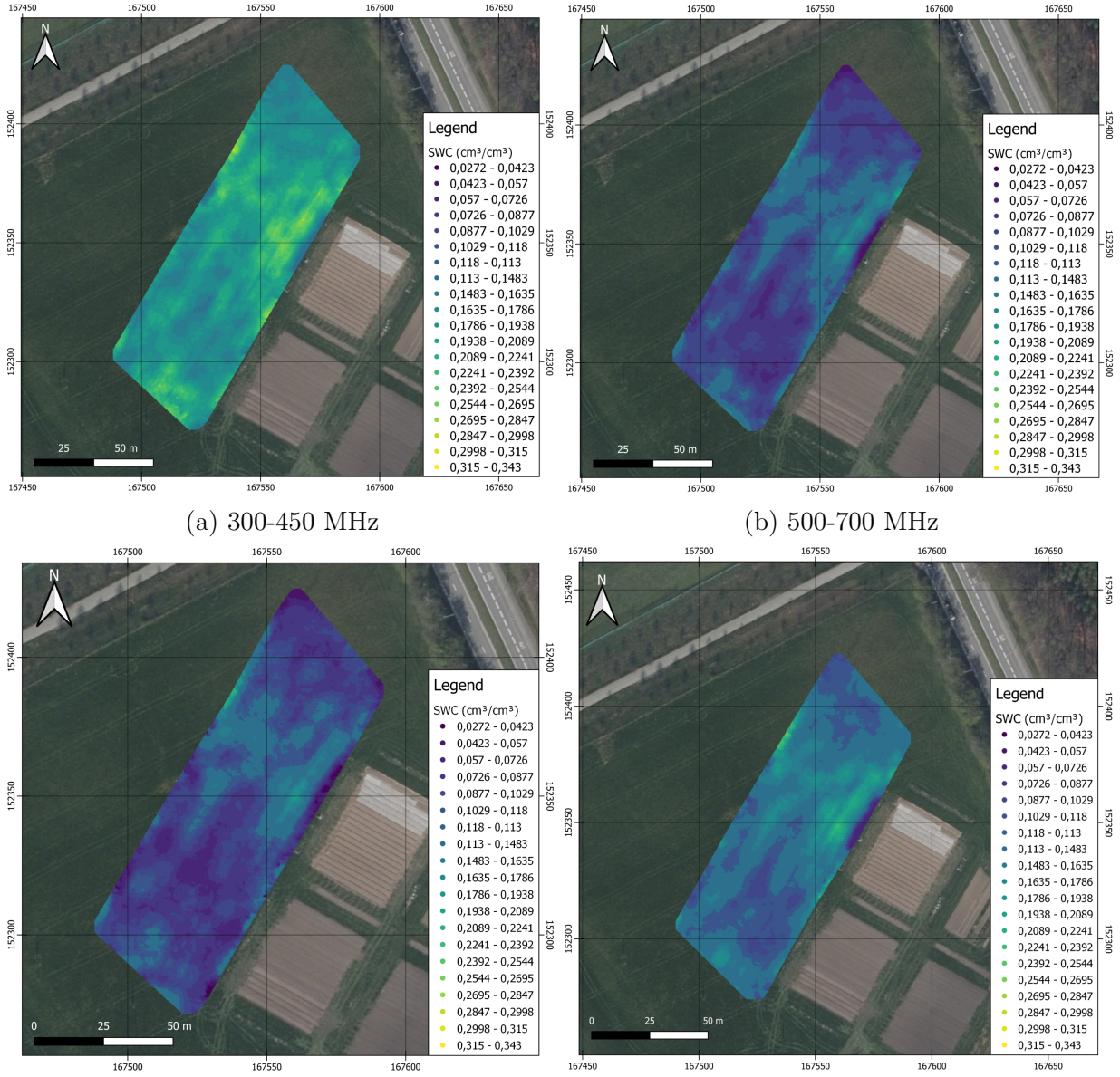

(a) 300-450 MHz

(b) 500-700 MHz

(c) 700-850 MHz

(d) 300-650 MHz

Figure 7.7 – Mapped kriged results of the logarithmic-periodic antenna considering four different frequency ranges.

Figure 7.7 represents the mapped kriged results of the first measurements dataset of the logarithmic-periodic antenna for different frequency ranges. High discrepancies were observed

when using different frequency ranges. In order to visualize the high discrepancies between these results, the same color scale for soil water content was chosen for the four different maps. Indeed, Figure 7.7a, which represents the lower frequencies map, shows the higher soil-water content. Conversely, Figure 7.7c, showing the results for the higher frequencies range, namely, 700-850 MHz presents the lower soil water content.

These differences, in function of the frequency may be due to the different characterization depths and the heterogeneous moisture through the soil profile.

Hence, considering this hypothesis, the higher retrieved soil moisture values with the lower frequencies would mean that the soil moisture increases with depth through the soil profile. This first deduction goes against the results presented in Figure 7.6, where higher soil moisture was measured in the 5cm depth layer than in the 10cm depth layer for almost all the sampled points. Nevertheless, the average depth of characterization is not known and may be out of the gravimetric sampled depth. In that regard, a new numerical experiment will be achieved and will attempt to determine the influence depth as a function of these different frequency ranges.

Another possible explanation of these discrepancies relies on the soil surface roughness consideration. Indeed, considering the Rayleigh criterion: $h_c = \lambda/8 \ \cos(\gamma)$, where h_c is the critical height of the surface protuberances, γ is the incidence angle and λ is the wavelength, a distinction can be made between smooth and rough surfaces. With a smooth surface, most of the energy reflected will be in the specular direction while with a rough surface, diffuse reflections or scattering will occur and lead therefore to less energy being recorded in the specular direction [Jonard et al., 2012]. The wavelength decreasing with the frequency increase, the critical height of the Rayleigh criterion decreases proportionally to the frequency increase and hence, the electromagnetic waves become more prone to the roughness scattering and diffusion. In that case, soil moisture would be underestimated.

Qualitatively, despite the frequency dependence of the results, all these four maps show the same trend in the humidity distribution, as observed in the previous soil moisture maps. Indeed, a moisture valley correlated to the topography is visible in the upper middle of the field.

7.4.1.1 Numerical experiments : depth of influence

To conduct these experiments aiming to determine the depth of influence as a function of the frequency ranges, a new model configuration was made to produce synthetic Green's functions. Figure 7.8 represents the used model configuration, where $\varepsilon_{r,1}$ is the relative permittiviy of the first soil layer and $\varepsilon_{r,2}$ is the relative permittivity of the second layer. A first numerical experiment is performed considering $\varepsilon_{r,1} = 5$ and $\varepsilon_{r,2} = 10$. A second experiment considers $\varepsilon_{r,1} = 15$ and $\varepsilon_{r,2} = 10$. For both numerical experiments, d_0 varies from 0 to 1 meter, with a step of 0.01 m.

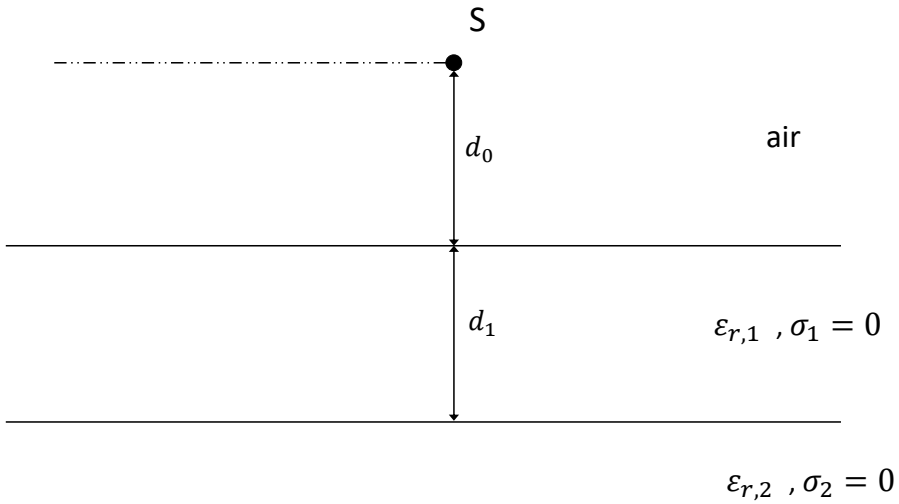

Figure 7.8 – Model configuration for the numerical experiments aiming to estimate of the depth of influence as a function of the frequency range. S is the point source and receiver corresponding to the antenna phase center.

The results of the first numerical experiment, i.e., the one which considers $\varepsilon_{r,1} = 15$ and $\varepsilon_{r,2} = 10$ is shown in Figure 7.9. The layering of the synthetic soil induces reflection at different interfaces which interfere in a constructive or destructive way and influence the reflections amplitudes. The presence of these interferences depends on the ratio between the wavelength λ, the relative permittivity contrast and the layer thickness d_1 as highlighted in [Lambot et al., 2006b], where similar numerical experiments were performed. In the paper of Lambot et al. [2006b], two cases are distinguished : if $d_1 < \lambda/2$ with a negative reflection coefficient at the interface between the layers, then the interferences will be destructive with a maximum for $d_1 = \lambda/4$. The second case is if $d_1 > \lambda/2$ with a positive reflection coefficient, the interferences will be constructive.

In Figure 7.9, it is visible that with a first soil layer thickness (h_1) being equal to 0, the retrieved permittivity through the model inversion is as expected the relative permittivity of the second layer. Inversely, when h_1 becomes larger, the estimated permittivity tends to the relative permittivity of the first layer. According to Lambot et al. [2006b], the oscillating behavior is an artefact of the inverse Fourier transform (used for the Green's functions transformation from the frequency to the time domain, see Equation (3.7)) when using limited frequency range.

A second numerical experiment was carried out using $\varepsilon_{r,1} = 15$ and $\varepsilon_{r,2} = 10$. The results are visible on Figure 7.10 and the inverse behavior compared to the previous numerical experiment is observed.

These numerical experiments provide a good support for the choice of the frequency range to use for the data processing. Here, the 300 - 650 MHz frequency band seems to be the most accurate, since it increases the signal-to-noise ratio by ignoring the higher frequency, whose

are more prone to noise and roughness, and the wider frequency window will provide more information. This frequency band will therefore be used for the signal inversion and hence, a better accuracy.

Regarding Figures 7.9d and 7.10d, an approximation of the depth of sensitivity can be derived. Indeed, according to the numerical experiments, if considering the first 10 soil centimeters (depth of the gravimetric sampling), the retrieved permittivity value is an intermediate value of the permittivities of the two soil layers and can even be under- or over- estimated, depending on the permittivity contrast. Therefore, a influence depth of 15 to 20cm is considered, as at this depth, the retrieved permittivity oscillates less importantly and is subjected to errors lower than 2 units of relative permittivity around $\varepsilon_{r,1}$ value, which results to an errors of soil moisture of 4%, approximately.

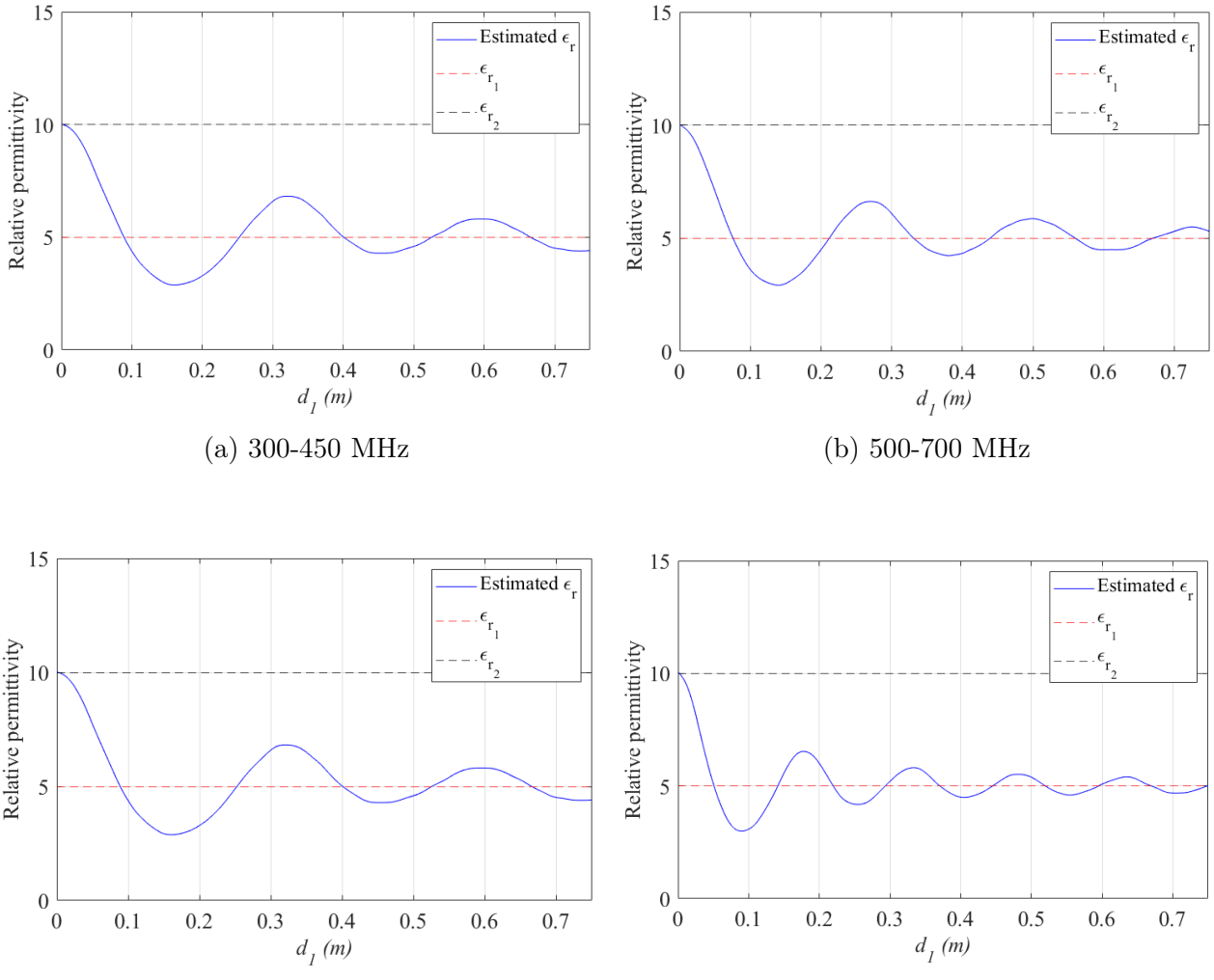

(a) 300-450 MHz

(b) 500-700 MHz

(c) 700-850 MHz

(d) 300-650 MHz

Figure 7.9 – Relative permittivity as a function of the thickness of the first soil layer for different frequency ranges. This numerical experiment considers $\varepsilon_{r,1} = 5$ and $\varepsilon_{r,2} = 10$.

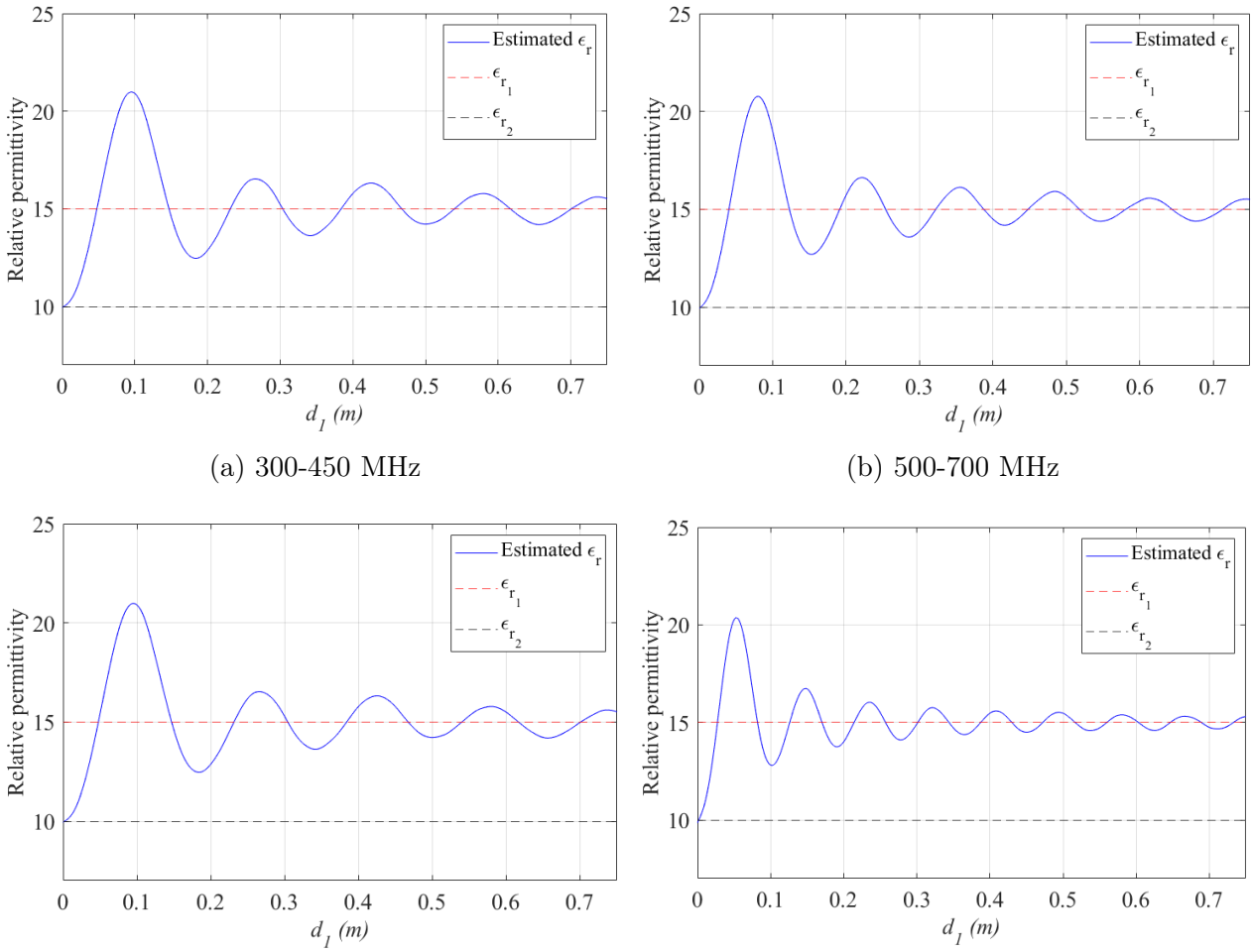

(a) 300-450 MHz

(b) 500-700 MHz

(c) 700-850 MHz

(d) 300-650 MHz

Figure 7.10 – Relative permittivity as a function of the thickness of the first soil layer for different frequency ranges. This numerical experiment considers $\varepsilon_{r,1} = 15$ and $\varepsilon_{r,2} = 10$.

7.4.1.2 Resulting maps after processing

The 300 - 650 MHz frequency band being selected through the numerical experiments, the 3 quad-GPR datasets using the logarithmic antenna were processed with this frequency range. The 3 resulting kriged maps are presented in Figure 7.11 and their correlation coefficients were calculated and are depicted in Table 7.2. These correlation coefficients indicate high spatial and temporal correlation, as it could be expected from the visual comparison of the three repetitions. This high correlation induces therefore a small RMSE between the repetitions, which equals 0.0094 between the first and the second repetitions, 0.0111 between the second and the third repetitions and 0.0122 cm^3cm^{-3} between the first and the third repetitions.

Nevertheless, it is important to note that the interpolation process was carried out using the same grid at the same location. Hence, this interpolation pattern combined with the micro-variability of the study field can explain a large part of the repetition uncertainties given that different locations point were measured to be assigned to a fixed point of the kriging grid.

Table 7.2 – Correlation coefficient between the three repetitions

	a	b	c
a	1	0.925	0.872
b	0.925	1	0.889
c	0.872	0.889	1

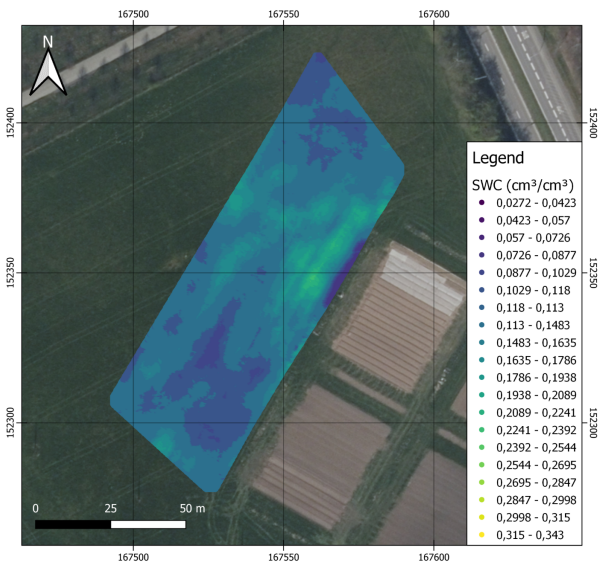

(a) 30/04/2021 quad-GPR - a

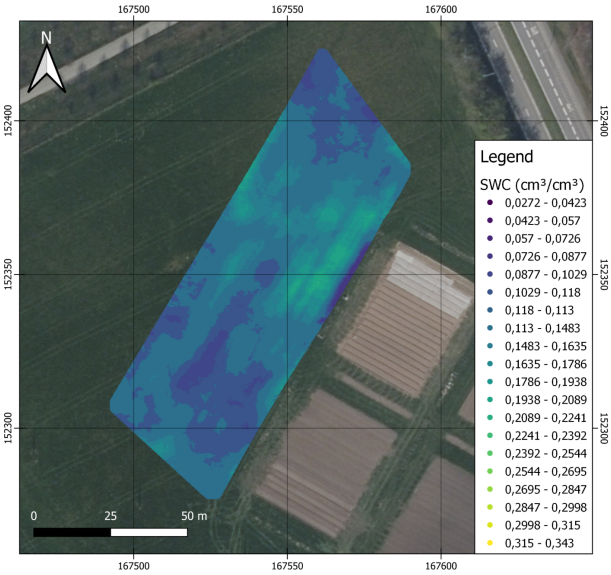

(b) 30/04/2021 quad-GPR - b

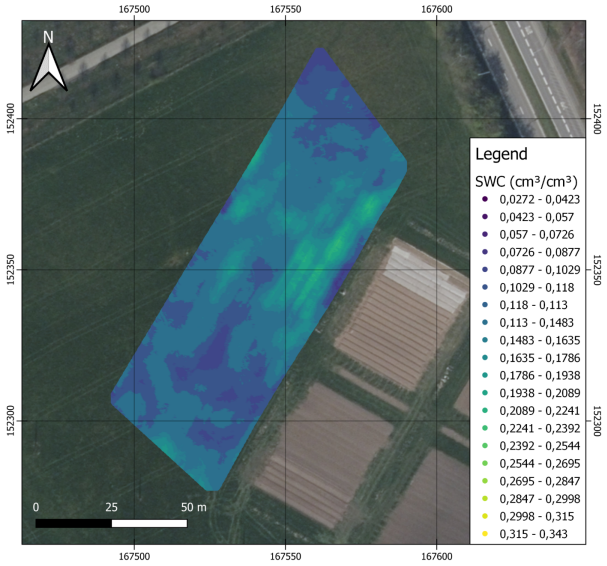

(c) 30/04/2021 quad-GPR - c

Figure 7.11 – Mapped kriged results of the logarithmic-periodic antenna for the 3 datasets.

7.4.2 UAV-dipole antenna results

The kriged results of the drone-borne radar acquisition are presented in Figure 7.12. The kriging was achieved with SAGA (System for Automated Geoscientific Analyses), a free open

source software since the MATLAB results were not satisfying. Note that the same color scale as for the other maps was used, except that two ranges of value were added (the two orange-shaded colors) for the higher moisture values. It is therefore visible that the estimated soil water content is much higher for the drone-borne GPR acquisition than through the quad-GPR acquisition.

The expected humidity valley related to the field topography is quite visible in its upper middle. Nevertheless, an unexplained humidity line is visible along the western limit of the studied area and might be due to measurement issues.

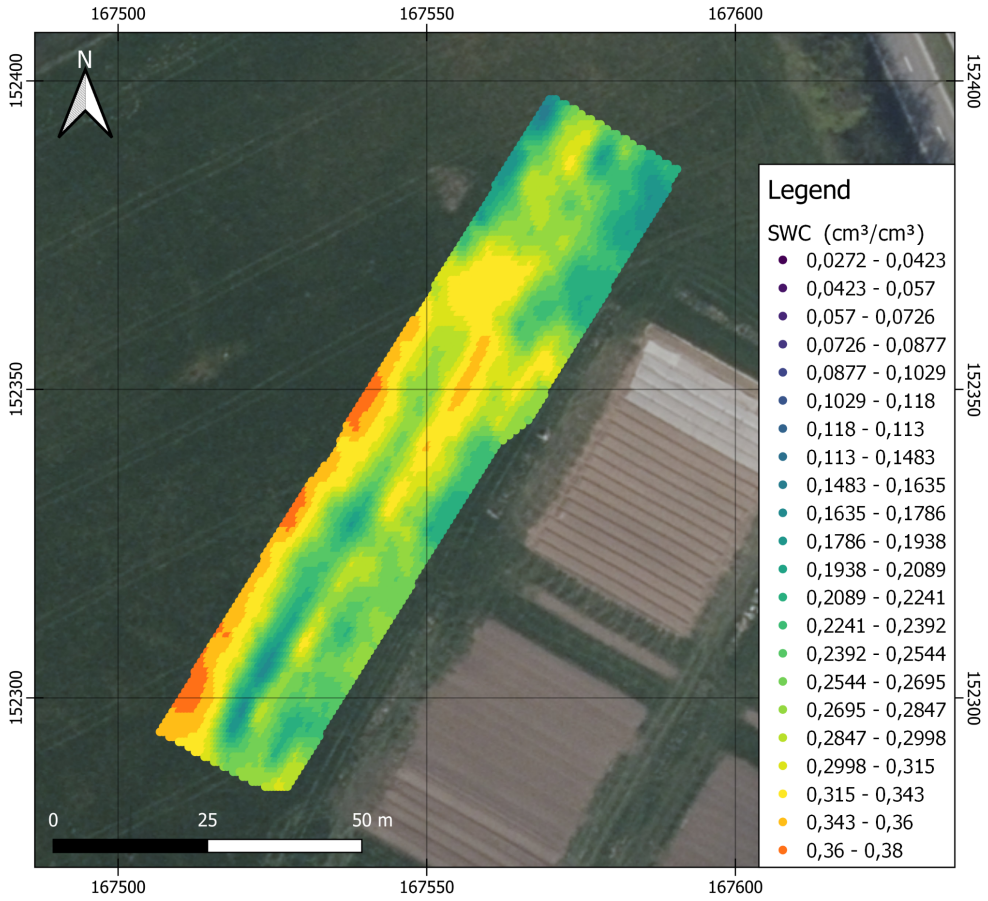

Figure 7.12 – Mapped kriged results of the drone-borne radar dataset.

7.4.3 Gravimetric and GPR results comparison

In order to allow the comparison of the measurements with methods considered as reference methods, fifteen locations were previously indicated with a flag and were dedicated to comparison measurements. Figure 7.13 shows the comparisons between drone-borne measurements and quad GPR measurements. It is quite visible that the quad-GPR soil moisture are generally smaller than the reference method. In the other side, the drone-borne acquisition seems to be more correlated to the gravimetric method but the discrepancies are still not negligible. The RMSE of these data are 0.1287 and 0.0391 for the $\theta_{quad} - \theta_{gravimetric}$ and $\theta_{drone} - \theta_{gravimetric}$, respectively.

Note that the $\theta_{drone} - \theta_{gravimetric}$ dataset contains only ten points since a technical issue and the battery capacity limited the acquisition time.

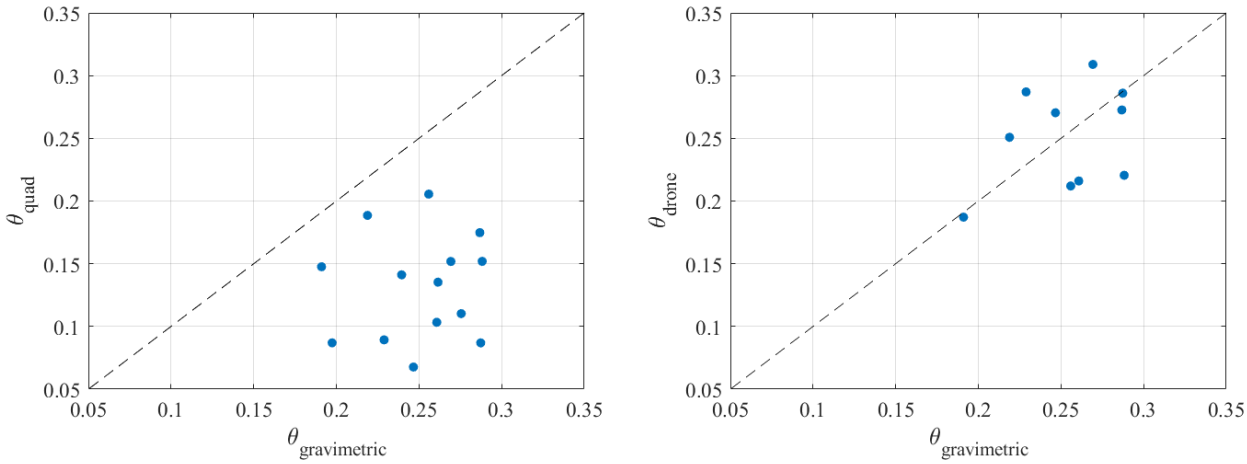

(a) Quad - gravimetric (0-10 cm) results comparison

(b) Drone - gravimetric (0-10 cm) results comparison

Figure 7.13 – Retrieved soil water content through full-waveform signal inversion for Quad-logarithmic antenna and drone-borne acquisition vs reference gravimetric measurements. The dashed line represents a perfect correlation.

Figure 7.14 shows the correlation plot between the retrieved moisture using the quad-GPR and the retrieved moisture using drone-GPR. From this plot, no correlation can be deduced between the two methods of measurements.

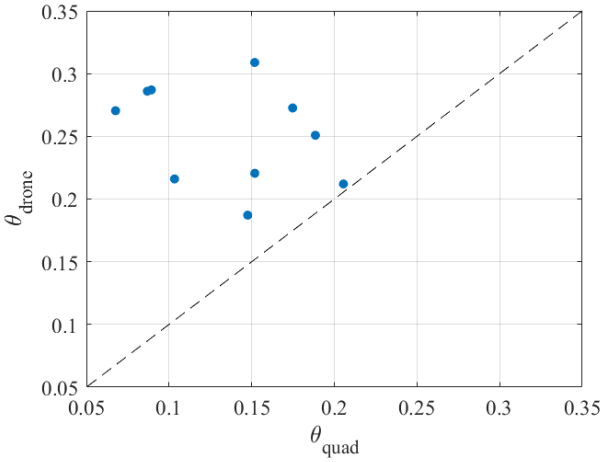

Figure 7.14 – Correlation plot between the drone-borne GPR and the quad-GPR measured SWC.

Figure 7.15 represents the boxplot of the four different measurements dataset acquired by GRP, either drone-borne GPR than quad GPR. This figure provides a summary of the differences found between the different methods, i.e., the higher retrieved permittivity through drone-borne GPR and the lower but well repeated permittivity of the quad-GPR using the logarithmic antenna.

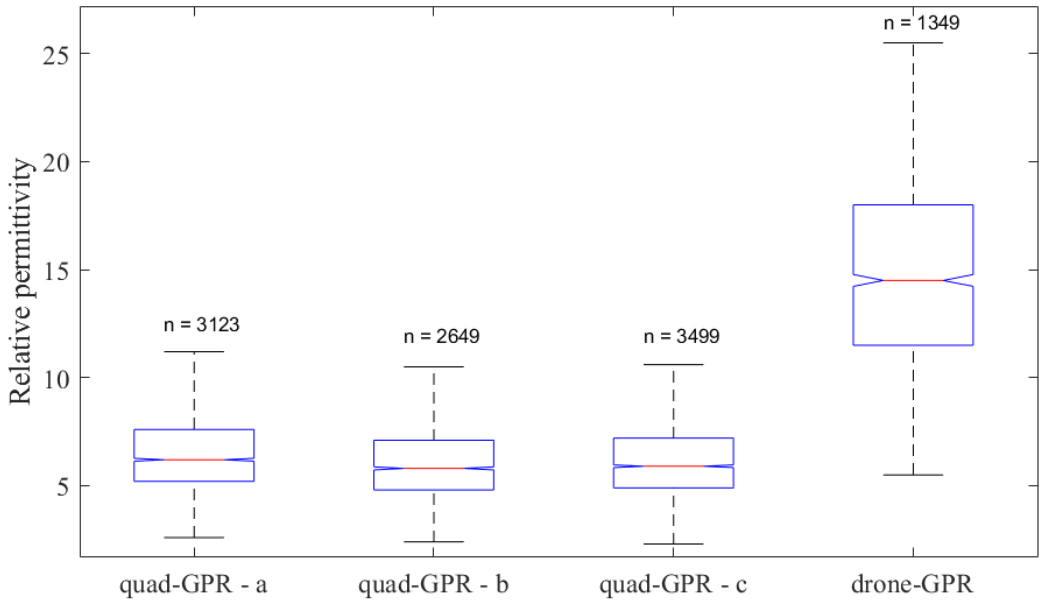

Figure 7.15 – Statistical comparison between the retrieved permittivity of the different measurements methods.

7.5 Summary and conclusion

In this chapter, two GPR setups were assessed through comparison with reference methods and repeatability. First, the quad-GPR data was processed and shows a high moisture variability when using different frequency ranges. An hypothesis based on the roughness of the field with respect to the Rayleigh criterion was advanced. Another hypothesis concerning the characterization depth was advanced but was not in accordance with the reference gravimetric results, which showed higher moisture values in the first five soil centimeters than in the next five soil centimeters. Therefore, numerical experiments were conducted to virtually assess the depth of influence using the 300 - 650 MHz frequency range, which appears to be between 15 and 20 centimeters.

Hence, based on the numerical experiments and the Rayleigh criterion, the frequency range of 300 - 650 MHz was selected for the data processing of the logarithmic antenna. However, despite the good repeatability of the three quad-GPR repetitions, the final results did not agree with the TDR and gravimetric measurements. One explanation is the different sampled volumes and the inherent microvariability of the soil moisture, including vertically.

Concerning the drone-borne GPR measurements, a technical issue occurred during the measurements and limited the validation of these data. Yet, the data comparison with the gravimetric data showed a quite good correlation, which is very promising. However, caution must be exercised as the resulting map showed an unexpected high soil water content in the western limit of the studied area, where no ground-truth SWC was taken.

Finally, despite that the validation of the drone-borne GPR soil water content measurement was the aim of this chapter and in a more global point-of-view, of this thesis, the results are not up to the task of carrying this validation. Indeed, the lack of raw data due to computer-related technical issue limited the comparison with ground-truth data, the repeatability assessment and therefore, the validation of the obtained results. However, very interesting results have been obtained, either numerical or real, and consistent maps were obtained with respect to the topography. Further research is needed to elucidate the reasons of the observed differences between the different measurement methods.

Chapter 8

Conclusion and prospects

8.1 Conclusion

Because agriculture is the leading consumer of freshwater and because the growing global population will further increase the food production needs, the already high pressure on water resource is set to increase. Nevertheless, the precision agriculture is much more sustainable than the traditional and could help to face the freshwater depletion by smarter irrigation. Nevertheless, precision irrigation needs information collection at high spatial and temporal resolution to be effective. In that regard, Ground Penetrating Radar methods has been identified as one of the most promising for soil water content monitoring at the field scale thanks to the high sensitivity of its wave velocity to changes in soil moisture [Klotzsche et al., 2018].

After several numerical experiments aiming in the assessment of the negligibility of the model assumptions, namely, the consideration of a non conductive soil, it was conclude that when using lower frequencies, as the frequency of the dipole antenna (235 - 295 MHz), higher errors on the permittivity retrieval are visible. The same is visible when considering lower permittivities.

In order the make the validation of drone-borne GPR information collection, several data acquisition were achieved. Their results were assessed, both qualitatively and quantitatively. The first drone-borne GPR acquisition were not satisfying and showed too high moisture values when compared to the expected values. Then, a new antenna was used when mounted on a all-terrain vehicle and showed very good results when regarding the soil water content and the water distribution in relation to the topography. The poor measurement quality of the drone-borne GPR acquisition may be due to the poor quality of the calibration, as it can be deduced regarding the discrepancies between H_i measured and H_i calibrated.

Finally, an acquisition campaign was carried out during an entire day. To allow the validation, different tools were used to supply comparison between the measurements and ground-truth soil moisture values were determined using gravimetric measurements. The final results

of the drone-borne GPR did not allow us to completely validate the measurement since a technical issue limited the acquired data. Indeed, despite a good correlation with the ground truth values, caution must be emphasized with the conclusion on the quality of these measurements since some unexpected values of soil moisture content were retrieved in an area where no ground truth value is available. Nevertheless, the different GPR results showed the expected water distribution in relation to the topography, which is very promising and comforting to attribute the discrepancies to the calibration process.

In an agricultural point of view, these GPR results are very promising in the view of the limitations in the volume sampled by TDR or gravimetric methods. As seen in this thesis, the reference gravimetric methods, despite being very time and work consuming, did not provide the information for the entire volume of interest, since the root of the vegetation are generally deeper than the accessible depth for gravimetric sampling. In that regard, the characterised volume using GPR is far more interesting for agricultural application, being larger but also easier to obtain.

8.2 Prospects

As highlighted in the Chapter 6, where several acquisition results were showed, a new calibration is needed for the dipole-UAV setup. Note that all the previous acquired data can be used since the measurements are completely independent of the radar transfer equations determined through the calibration. Hence, once the new calibration achieved, all the previous maps can be corrected and reassessed. In that regard, a new calibration is already scheduled and will be carried out thanks to a magnetic paint applied on a large tarp. The magnetic paint will play the role of the PEC (perfect electric conductor). The advantage of such calibration is that the conductive materials present in the lab will no more interfere with the poorly directive dipole electromagnetic waves.

Also, it could be interesting to compare the retrieved soil moisture content through GPR and through SAR (Synthetic Aperture Radar) methods, such as Sentinel-1. Indeed, the lower spatial resolution of SAR does not allow the detection of very local variations, but it could nevertheless provide good and easily obtainable data for mutual validation. A similar project (project RAPAS) has already been carried out by the Belgian Earth Observation.

Another interesting aspect to develop is the automation of the flight for data acquisition. This would provide more regular intervals between the measurements lines and, hence, more accurate and rigorous sensing. Automation could also provide a real-time moisture map for the user, permitting to directly assess the measurements quality, or even the water deficit of the field with regard to agricultural management.

Finally, to enhance measurements quality, a measurement of the incident antenna angle in

relation to the ground could be very useful if integrated into the model or at least, if considered in relation of the antenna transfer equation. Similarly, a measurement of the soil roughness, e.g., by a laser profiler, could be considerably useful as higher frequencies are more sensitive to scattering. Of course, these additional equipments would increase the load on the UAV and are therefore at the expense of flight time of the UAV and, hence, may be not compatible with the UAV application.

Bibliography

Annan, A. P. (2012). *11. Ground-Penetrating Radar*, pages 357–438. Society of Exploration Geophysicists.

Awak, E. et al. (2017). Determination of soil electrical conductivity using ground penetrating radar (gpr) for precision agriculture. *Int. J. Sci. Eng. Res*, 8(1):1971–1977.

Belgian Earth Observation (2021). RAPAS: New drone-borne methods for digital soil mapping. https://eo.belspo.be/en/news/rapas-new-drone-borne-methods-digital-soil-mapping. Accessed: 2021-06-04.

Bielders, C. and Javaux, M. (2019). Cours de physique du sol appliquée à l'agronomie et l'environnement (LBRES2103). Faculté des Bioingénieurs, Université catholique de Louvain.

Cassidy, N. (2009). Electrical and magnetic properties of rocks, soils and fluids. In *Ground Penetrating Radar: Theory and Applications*, pages 41–72. Elsevier. Journal Abbreviation: Ground Penetrating Radar.

Chanzy, A., Tarussov, A., Bonn, F., and Judge, A. (1996). Soil water content determination using a digital ground-penetrating radar. *Soil science society of America journal*, 60(5):1318–1326.

Chenoweth, J. (2008). Minimum water requirement for social and economic development. *Desalination*, 229(1):245–256.

Climat.be (2013). Le climat en belgique. https://climat.be/en-belgique/climat-et-emissions/climat. Accessed: 2021-04-06.

Dalton, F. N. and Van Genuchten, M. T. (1986). The time-domain reflectometry method for measuring soil water content and salinity. *Geoderma*, 38(1):237–250.

Davis, J. L. and Chudobiak, W. J. (1975). In situ meter for measuring relative permittivity of soils. In *Report of activities*. Geological survey of Canada.

EMLID (2021). Reach m+ uav mapping kit. https://store.emlid.com/product/reach-mapping-kit/. Accessed: 2021-04-07.

FAO (2017). *Water for Sustainable Food and Agriculture A report produced for the G20 Presidency of Germany*. Food and Agriculture Organization of the United Nations.

Geoportail de la Wallonie (2014). Relief de la wallonie - modèle numérique de terrain (mnt) 2013-2014. http://geoportail.wallonie.be/catalogue/6029e738-f828-438b-b10a-85e67f77af92.html. Accessed: 2021-04-06.

Green, J. K., Seneviratne, S. I., Berg, A. M., Findell, K. L., Hagemann, S., Lawrence, D. M., and Gentine, P. (2019). Large influence of soil moisture on long-term terrestrial carbon uptake. *Nature*, 565(7740):476–479. Number: 7740 Publisher: Nature Publishing Group.

Griffin, T. W., Shockley, J. M., and Mark, T. B. (2018). Economics of precision farming. *Precision agriculture basics*, pages 221–230.

Grisso, R. D., Alley, M. M., Holshouser, D. L., and Thomason, W. E. (2005). Precision farming tools: Soil electrical conductivity. *Virginia Cooperative Extension*.

Huisman, J. A., Hubbard, S. S., Redman, J. D., and Annan, A. P. (2003). Measuring soil water content with ground penetrating radar: A review. *Vadose zone journal*, 2(4):476–491.

Infoclimat (2021). Climatologie de l'année 2020 à lasne-chapelle-saint-lambert. https://www.infoclimat.fr/climatologie. Accessed: 2021-04-06.

Jol, H. M. (2008). *Ground penetrating radar theory and applications*. Elsevier.

Jonard, F. (2020). Gestion intégrée des ressources en eau (LBRES2204). Faculté des Bio-ingénieurs, Université catholique de Louvain.

Jonard, F., Weihermüller, L., Vereecken, H., and Lambot, S. (2012). Accounting for soil surface roughness in the inversion of ultrawideband off-ground gpr signal for soil moisture retrieval. *Geophysics*, 77(1):H1–H7.

Kamienski, C., Soininen, J.-P., Taumberger, M., Dantas, R., Toscano, A., Salmon Cinotti, T., Filev Maia, R., and Torre Neto, A. (2019). Smart water management platform: Iot-based precision irrigation for agriculture. *Sensors*, 19(2):276.

Klotzsche, A., Jonard, F., Looms, M. C., van der Kruk, J., and Huisman, J. A. (2018). Measuring soil water content with ground penetrating radar: A decade of progress. *Vadose Zone Journal*, 17(1):1–9.

Lambot, S. and André, F. (2014). Full-wave modeling of near-field radar data for planar layered media reconstruction. *IEEE Transactions on Geoscience and Remote Sensing*, 52(5):2295–2303.

Lambot, S., Antoine, M., Vanclooster, M., and Slob, E. C. (2006a). Effect of soil roughness on the inversion of off-ground monostatic gpr signal for noninvasive quantification of soil properties. *Water Resources Research*, 42(3).

Lambot, S., Slob, E., and Vereecken, H. (2007). Fast evaluation of zero-offset green's function for layered media with application to ground-penetrating radar. *Geophysical Research Letters*, 34(21).

Lambot, S., Slob, E. C., van den Bosch, I., Stockbroeckx, B., and Vanclooster, M. (2004). Modeling of ground-penetrating radar for accurate characterization of subsurface electric properties. *IEEE Trans. Geosci. Remote. Sens.*, 42(11):2555–2568.

Lambot, S., Weihermüller, L., Huisman, J. A., Vereecken, H., Vanclooster, M., and Slob, E. C. (2006b). Analysis of air-launched ground-penetrating radar techniques to measure the soil surface water content. *Water resources research*, 42(11).

Lavoué, F. (2014). *2D full waveform inversion of ground penetrating radar data: towards multiparameter imaging from surface data*. PhD thesis, Université de Grenoble.

Ledieu, J., De Ridder, P., De Clerck, P., and Dautrebande, S. (1986). A method of measuring soil moisture by time-domain reflectometry. *Journal of Hydrology*, 88(3-4):319–328.

Lunt, I., Hubbard, S., and Rubin, Y. (2005). Soil moisture content estimation using ground-penetrating radar reflection data. *Journal of Hydrology*, 307(1):254–269.

Meter Environment (2021). TEROS 12 advanced soil moisture sensing. https://www.metergroup.com/environment/products/teros-12/. Accessed: 2021-05-16.

Minet, J., Bogaert, P., Vanclooster, M., and Lambot, S. (2012). Validation of ground penetrating radar full-waveform inversion for field scale soil moisture mapping. *Journal of Hydrology*, 424:112–123.

Mohanty, B. P., Cosh, M. H., Lakshmi, V., and Montzka, C. (2017). Soil moisture remote sensing: State-of-the-science. *Vadose Zone Journal*, 16(1):1–9.

Noborio, K. (2001). Measurement of soil water content and electrical conductivity by time domain reflectometry: a review. *Computers and Electronics in Agriculture*, 31(3):213–237.

Oki, T., Yano, S., and Hanasaki, N. (2017). Economic aspects of virtual water trade. *Environmental research letters*, 12(4):044002.

Orfanidis, S. J. (2002). Electromagnetic waves and antennas. *Rutgers University New Brunswick, NJ*.

Pimentel, D., Berger, B., Filiberto, D., Newton, M., Wolfe, B., Karabinakis, E., Clark, S., Poon, E., Abbett, E., and Nandagopal, S. (2004). Water Resources: Agricultural and Environmental Issues. *BioScience*, 54(10):909–918.

RCTakeOff (2021). Price offer rcto-pro x8. https://www.rctopro.be/price-offer/x8/. Accessed: 2021-02-04.

Robinson, D. A., Jones, S. B., Wraith, J. M., Or, D., and Friedman, S. P. (2003). A review of advances in dielectric and electrical conductivity measurement in soils using time domain reflectometry. *Vadose Zone Journal*, 2(4):444–475.

Ryu, J.-S., Kim, M.-S., Cha, K.-J., Lee, T. H., and Choi, D.-H. (2002). Kriging interpolation methods in geostatistics and dace model. *KSME International Journal*, 16(5):619–632.

Samouëlian, A., Cousin, I., Tabbagh, A., Bruand, A., and Richard, G. (2005). Electrical resistivity survey in soil science: a review. *Soil and Tillage Research*, 83(2):173–193.

Schwartz, B. F., Schreiber, M. E., and Yan, T. (2008). Quantifying field-scale soil moisture using electrical resistivity imaging. *Journal of Hydrology*, 362(3):234–246.

Schwarzbeck (2021). Standard lpda. http://www.schwarzbeck.de/en/antennas/logarithmic-periodic-broadband-antennas/standard-lpda.html. Accessed: 2021-04-06.

Schwarzbeck (2021a). UHA 9105 - dipole antenna radiation pattern.

Schwarzbeck (2021b). UHALP 9108 a - log periodic antenna radiation pattern.

Shiklomanov, I. A. (1998). *World water resources: a new appraisal and assessment for the 21st century: a summary of the monograph World water resources*. Unesco.

Slob, E., Lambot, S., Miller, R., Bradford, J., and Holliger, K. (2010). Direct determination of electric permittivity and conductivity from air-launched gpr surface-reflection data. In *Advances in Near-Surface Seismography and Ground-Penetrating Radar*, pages 251–261. Society of Exploration Geophysicists.

Thomas, A. M. (2010). *Measurement of electromagnetic signal velocities in saturated fine-grained soils*. PhD thesis, University of Birmingham.

Topp, G. C., Davis, J. L., and Annan, A. P. (1980). Electromagnetic determination of soil water content: Measurements in coaxial transmission lines. *Water resources research*, 16(3):574–582.

Tran, A. P., André, F., Craeye, C., and Lambot, S. (2013). Near-field or far-field full-wave ground penetrating radar modeling as a function of the antenna height above a planar layered medium. *Progress In Electromagnetics Research*, 141:415–430.

Vallozzi, L., Hertleer, C., and Rogier, H. (2016). 26 - latest developments in the field of textile antennas. In Koncar, V., editor, *Smart Textiles and their Applications*, Woodhead Publishing Series in Textiles, pages 599–626. Woodhead Publishing, Oxford.

Wallace, J. (2000). Increasing agricultural water use efficiency to meet future food production. *Agriculture, Ecosystems & Environment*, 82(1):105 – 119.

Wu, K., Rodriguez, G. A., Zajc, M., Jacquemin, E., Clément, M., De Coster, A., and Lambot, S. (2019). A new drone-borne gpr for soil moisture mapping. *Remote Sensing of Environment*, 235:111456.

Zakri, T. (1997). *Contribution à l'étude des propriétés diélectriques de matériaux poreux en vue de l'estimation de leur teneur en eau : modèles de mélange et résultats expérimentaux*. PhD thesis, Université de Grenoble.

Appendix A

A.1 Reference gravimetric and 5cm depth TDR results

Table A.1 – Soil water content results determined by gravimetric method and comparison with 5cm depth TDR measurements.

	Gravimetric results (cm^3/cm^3)			TDR (cm^3/cm^3)	
Points	5 cm depth	10 cm depth	Average	5cm depth	Δ
1	0.260	0.234	0.247	0.271	0.024
2	0.290	0.232	0.261	0.307	0.046
3	0.323	0.251	0.287	0.303	0.016
4	0.296	0.216	0.256	0.276	0.020
5	0.176	0.206	0.191	0.211	0.020
6	0.324	0.253	0.288	0.285	0.003
7	0.253	0.185	0.219	0.208	0.011
8	0.325	0.249	0.287	0.312	0.025
9	0.294	0.244	0.269	0.307	0.038
10	0.260	0.198	0.229	0.220	0.009
11	0.300	0.223	0.262	0.313	0.052
12	0.246	0.233	0.240	0.284	0.045
13	0.322	0.229	0.276	0.296	0.020
14	/	0.285	0.285	0.316	/
15	0.203	0.192	0.197	0.235	0.038
Average	0.276	0.225	0.251	0.273	0.026

Validation of drone-borne Ground Penetrating Radar method for soil moisture mapping.

Thibaut Parizel

Nowadays, agriculture is the leading consumer of freshwater resources, accounting for 70% of the global extracted volume. With the global population set to increase by 65% by 2050, pressure on freshwater resources will increase more importantly without a more sustainable agricultural system.

In that regard, Ground Penetrating Radar (GPR) methods are very promising with respect to the precision irrigation, which needs information collection of soil water content at high spatial resolution. GPR methods can bridge the gap between the small scale of the TDR and the larger scales of the remote sensing instruments and constitute therefore an useful tool for the road to sustainability.

This thesis aims the validation of the soil moisture mapping through drone-borne GPR using the radar model of Lambot et al. (2004). In this paper, several numerical experiments were carried out to assess the viability of the assumptions of the model. Then, some acquisition campaigns were conducted and the results were assessed both quantitatively and qualitatively. Finally, a validation campaign was carried out using several tools in order to allow the comparison between these, as well as with ground-truth moisture value.

UNIVERSITÉ CATHOLIQUE DE LOUVAIN
Faculté des bioingénieurs
Croix du Sud, 2 bte L7.05.01, 1348 Louvain-La-Neuve, Belgique | www.uclouvain.be/agro